

1-1-1980

Very long baseline interferometry observations of the masers toward Orion A.

Stanley Severin Hansen
University of Massachusetts Amherst

Follow this and additional works at: https://scholarworks.umass.edu/dissertations_1

Recommended Citation

Hansen, Stanley Severin, "Very long baseline interferometry observations of the masers toward Orion A." (1980). *Doctoral Dissertations 1896 - February 2014*. 1868.
https://scholarworks.umass.edu/dissertations_1/1868

This Open Access Dissertation is brought to you for free and open access by ScholarWorks@UMass Amherst. It has been accepted for inclusion in Doctoral Dissertations 1896 - February 2014 by an authorized administrator of ScholarWorks@UMass Amherst. For more information, please contact scholarworks@library.umass.edu.

UMASS/AMHERST



312066 0015 5911 0

VERY LONG BASELINE INTERFEROMETRY OBSERVATIONS
OF THE MASERS TOWARD ORION A

A Dissertation Presented

By

STANLEY SEVERIN HANSEN II

Submitted to the Graduate School of the
University of Massachusetts in partial fulfillment
of the requirements for the degree of

DOCTOR OF PHILOSOPHY
MAY 1980
PHYSICS AND ASTRONOMY

©

Stanley Severin Hansen II 1980

All Rights Reserved

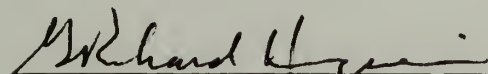
VERY LONG BASELINE INTERFEROMETRY OBSERVATIONS
OF THE MASERS TOWARD ORION A

A Dissertation Presented

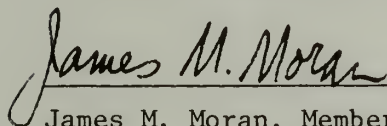
by

STANLEY SEVERIN HANSEN II


Approved as to style and content by:



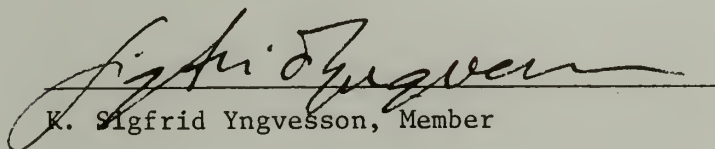
G. Richard Huguenin, Chairman of Committee



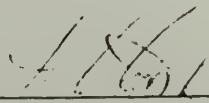
James M. Moran, Member



William A. Dent, Member



K. Sigfrid Yngvesson, Member



LeRoy F. Cook, Head
Department of Physics and Astronomy

A C K N O W L E D G M E N T S

A dissertation cannot be written without the intellectual and emotional help of others. As I hold the finished manuscript in my hands, I recall all the people who have helped me reach this point. I must first thank my advisor, Jim Moran, for all his help, encouragement, education, prompting, and especially patience. Only now as I look back do I realize how much he taught me, and how essential his contributions were to the completion of this dissertation. I also owe many thanks to Mark Reid for his encouragement, guidance and review of my dissertation, and to Ken Johnston for his never slacking harassment. My thanks also go to my committee, Richard Huguenin, Bill Dent, and Sigfrid Yngvesson, for their help over the long years.

A successful VLBI observation requires the untiring efforts of many people at several telescopes. My thanks go to the staffs of the National Radio Astronomy Observatory in Green Bank, the Five College Radio Astronomy Observatory, the Haystack Observatory, the Naval Research Laboratory Telescope at Maryland Point, the Owens Valley Radio Astronomy Observatory, the Algonquin Park Radio Astronomy Observatory, the Harvard Radio Astronomy Station at Fort Davis, and the Hat Creek Observatory. I also must thank all those who toiled with me on the processor: Craig Walker, Aubrey Haschick, Rinehard Genzel, Fred Lo, Pat Crane, John Spencer, and Alan Yen. I also owe a debt of thanks for the support I received from my fellow graduate students, especially Adair Lane, who carefully read this dissertation.

I am particularly indebted to the National Radio Astronomy Observatory (NRAO) for providing a comfortable, perhaps too comfortable, place to work, and for helping me to produce this dissertation. Special thanks go to Joe Burch and his VLBI processing crew: Russ McCrickard, Ted Haight, Allen Jewel, and Chris Rye, and to Benno Rayhrer, Walter Brown, and Bob Elcox for maintaining the processor. I am indebted to Peggy Weems and Pat Smiley of the NRAO graphics department for turning my rough drawings into the figures presented in this dissertation. I must thank Phyllis Jackson for typing the manuscript. And my everlasting gratitude goes to all the people in Charlottesville, past and present, for making my first six years at the Observatory so enjoyable.

And finally, for encouragement and comfort from outside astronomy, I owe so much to Kathy who helped me start graduate school, Georganna, Sandy, and Ellen, who helped me along the way, Ann, who shared much of the agony of writing this dissertation, and Danielle, who kept my spirits up at the end.

To my parents and my sister, I dedicate this dissertation.

ABSTRACT

VERY LONG BASELINE INTERFEROMETRY OBSERVATIONS
OF THE MASERS TOWARD ORION A

May 1980

Stanley Severin Hansen II

B.S., University of Missouri

M.S., Ph.D., University of Massachusetts

Directed by: Professor G. Richard Huguenin

The water vapor masers towards Orion A were mapped at six epochs between 1972 and 1978 by very long baseline interferometry (VLBI) with relative positional accuracy of 0".01 in right ascension and 0".1 in declination. Approximately 30 masers with velocities within 20 km s^{-1} of the molecular cloud velocity lie in an area 30" in diameter centered on the Kleinmann-Low nebula. The masers are typically a few astronomical units in diameter. Most H_2O masers occur in clusters less than 2" (1000 a.u.) in diameter. Within a cluster are several velocity features which are often not coincident. The lifetime of a cluster is longer than ten years. The individual velocity features last for years, but they show amplitude variations on a time scale of weeks or months. Amplitude variations in the individual velocity features or the clusters do not show a correlation which would suggest a common pump. The positions of the velocity features were constant over six years to 50 a.u. The limits on the proper motions of the masers show that their transverse velocities are less than or equal to the radial velocity dispersion of the masers. The features have a full width at

half maximum of 1 km s^{-1} . Most strong features are accompanied by weak emission spread over several kilometers per second. The velocity separations between features in a cluster are typically 1 km s^{-1} , but separations larger than 20 km s^{-1} are occasionally observed.

Based on velocity, variability, and position, the water vapor masers in Orion may be divided into five classes, four of which are associated with stages of star formation. The fifth class may be associated with an evolved star. The masers of the fifth class have velocities from -7 to -3 km s^{-1} and from $+15$ to $+18 \text{ km s}^{-1}$. These masers are larger (10 to 60 a.u.) and less variable than the other H_2O masers, and occur in a single cluster 1000 a.u. in diameter. The OH masers with velocities similar to the fifth class of H_2O masers are less variable, less polarized, and larger than the other OH masers. All the SiO masers have the same velocities as the H_2O masers of the fifth class and are at the same position. This evidence strongly suggests that all these masers exist in expanding shells of gas about a single object.

VLBI observations at 1665 MHz detected three OH masers with apparent diameters of 10-30 a.u. The two strongest of these were spatially coincident, circularly polarized in opposite senses, and of equal amplitude, suggesting that they may be a Zeeman pair. The velocity separation requires a 3 milligauss magnetic field. Single telescope observations at 1612 MHz show a clearly identifiable Zeeman pattern for a 4 milligauss field.

TABLE OF CONTENTS

Chapter		
I.	INTRODUCTION TO STAR FORMATION AND THE ORION NEBULA....	1
1.1	Star Formation.....	1
1.2	The Orion Region.....	9
1.2.1	Overview.....	9
1.2.2	The Large CO Clouds.....	22
1.2.3	The Orion Nebula.....	23
1.2.4	The Compact Core of the Nebula.....	24
1.2.5	The Orion Molecular Cloud and the Central Ridge.....	26
1.2.6	The Kleinmann-Low Nebula.....	27
1.2.6.1	Infrared.....	27
1.2.6.2	High velocity molecular emission.....	28
1.2.6.3	Molecular hydrogen.....	30
1.2.7	Masers.....	31
1.2.7.1	The water vapor masers.....	31
1.2.7.2	The hydroxyl masers.....	32
1.2.7.3	The silicon oxide masers.....	32
1.2.7.4	The methanol masers.....	33
1.2.8	Stars.....	35
1.2.8.1	The Becklin-Neugebauer source.....	35
1.2.8.2	An evolved star.....	36
1.3	Summary.....	38
II.	DATA ANALYSIS.....	39
2.1	Theory.....	39
2.2	Processing.....	41
2.3	Map Making.....	58
2.4	Maser Size.....	62
III.	THE WATER VAPOR MASERS.....	66
3.1	Early Water Vapor Observations of Orion.....	66
3.2	New Maps of the Water Vapor Masers in Orion.....	79
3.2.1	NE11.....	112
3.2.2	NE4.....	113
3.2.3	NE6.....	113
3.2.4	NW3.....	114
3.2.5	The Central Region.....	114
3.2.6	A-2.....	115
3.2.7	A3.....	115
3.2.8	A6.....	116
3.2.9	A15.....	117

3.2.10	A18.....	118
3.2.11	B8.....	118
3.2.12	B9.....	118
3.2.13	B18.....	118
3.2.14	Nondetections.....	119
3.3	Discussion.....	119
IV.	THE HYDROXYL MASERS.....	136
4.1	VLBI Observations.....	136
4.2	The Magnetic Fields.....	142
4.2.1	Introduction.....	142
4.2.2	Observations.....	147
4.2.2.1	1665 MHz.....	148
4.2.2.2	1612 MHz.....	154
4.2.3	Maser Models.....	160
4.2.4	Appendix to Chapter IV: One Dimensional Maser Models.....	164
4.2.4.1	The transfer equation.....	165
4.2.4.2	The physical parameters.....	172
V.	CONCLUSIONS.....	177
.....		
	BIBLIOGRAPHY.....	181
	APPENDIX: DETAILED MODELS FOR THE WATER VAPOR OBSERVATIONS..	190
A.1	Observations of Water Vapor Maser Regions.....	190
A.1.1	Spectra.....	190
A.1.1.1	The low velocity features.....	190
A.1.1.2	The high velocity features.....	191
A.1.2	Association with Other Sources.....	192
A.1.2.1	The water vapor masers.....	192
A.1.2.2	The hydroxyl masers.....	192
A.1.2.3	Infrared sources.....	192
A.1.2.4	HII regions.....	193
A.2	Interpretation of the Observations.....	194
A.2.1	The Basic Model.....	194
A.2.1.1	The maximum gain model.....	194
A.2.1.2	The planetary model.....	194
A.2.2	The Low Velocity Features.....	195
A.2.2.1	The gas motion.....	195
A.2.2.2	The driving force.....	196
A.2.2.3	A detailed model of Orion source "A".....	199
A.2.3	The High Velocity Features.....	200
A.2.4	Other Phenomena.....	202
A.2.5	An HII Region Powered Model.....	203

List of Tables

1. Absolute positions of emission sources towards Orion A.....	19
2. Constant telescope parameters of the H ₂ O VLBI observations...	81
3. Varying telescope parameters of the H ₂ O VLBI observations....	82
4. H ₂ O VLBI observing session parameters.....	83
5. Orion H ₂ O features 1972 December 20.....	84
6. Orion H ₂ O features 1974 January 31.....	85
7. Orion H ₂ O features 1975 March 8-13.....	86
8. Orion H ₂ O features 1976 September 16-18.....	87
9. Orion H ₂ O features 1978 July 22.....	89
10. Orion H ₂ O features 1978 November 2.....	91
11. The number of H ₂ O masers in Orion as a function of flux density and position.....	121
12. Orion OH features 1977 November 14-18.....	151
13. The right and left circularly polarized and unpolarized features in the 1612 MHz spectra of Orion.....	158
14. Model optical depths and saturation intensities for the 1612 MHz masers.....	171

List of Illustrations

1. The Orion molecular complexes and the I Ori OB association.....	5
2. A map of the galaxy showing several maser sources and sites of star formation.....	10
3. The constellation Orion.....	11
4. The region of Orion within Barnard's loop.....	12
5. The Orion nebula with 1.95 cm radio contours.....	13
6. The core of the Orion nebula with 5 GHz contours.....	15
7. The Kleinmann-Low nebula complex and the Trapezium.....	16
8. The Kleinmann-Low nebula with the absolute positions of the H ₂ O, OH, SiO, and CH ₃ OH masers, the compact IR sources, and the H ₂ contours.....	18
9. An idealized schematic diagram of a shell source and the resultant spectra.....	37
10. Sample VLBI fringe rate spectra.....	47
11. A sample plot of fringe amplitude as a function of fringe rate and velocity.....	50
12. Sample velocity spectra at particular fringe rates.....	52
13. A sample plot of the peak amplitude and its fringe rate from the fringe rate spectrum for each velocity channel.....	55
14. The hyperfine lines of the 6 ₁₆ → 5 ₂₃ rotational transition of H ₂ O.....	68
15. Orion H ₂ O 1970 June 21 Mark I VLBI map.....	71
16. Orion H ₂ O 1971 February 20 Mark I VLBI map.....	72
17. Orion H ₂ O 1971 March 28 Mark I VLBI map.....	73
18. Orion H ₂ O 1976 June 6 single telescope map.....	75
19. Orion H ₂ O 1976 October–November single telescope map including the high velocity features.....	77

20.	Orion H ₂ O 1976 December 7 spectrum, including the high velocity features.....	78
21.	Orion H ₂ O 1972 December 20 Mark II VLBI map.....	94
22.	Orion H ₂ O 1974 January 31 Mark II VLBI map.....	95
23.	Orion H ₂ O 1975 March 8-13 Mark II VLBI map.....	96
24.	Orion H ₂ O 1976 September 16-18 Mark II VLBI map.....	97
25.	Orion H ₂ O 1978 July 22 Mark II VLBI map.....	98
26.	Orion H ₂ O 1978 November 2 Mark II VLBI map.....	99
27.	Orion H ₂ O composite map of all the VLBI epochs.....	101
28.	Orion H ₂ O expanded scale composite map of the southwest clusters of masers.....	102
29.	Orion H ₂ O 1972 December 20 spectrum.....	103
30.	Orion H ₂ O 1974 January 31 spectrum.....	104
31.	Orion H ₂ O 1975 March 8-13 spectrum.....	105
32.	Orion H ₂ O 1976 September 16-18 spectrum.....	107
33.	Orion H ₂ O 1978 July 22 spectrum.....	108
34.	Orion H ₂ O 1978 November 2 spectrum.....	110
35.	The intensities and velocities of the 10 and 11 km s ⁻¹ features in the NE11 cluster at each VLBI epoch.....	111
36.	The number of pairs of H ₂ O maser velocity features as a function of their velocity separation.....	122
37.	The shell features in the H ₂ O, OH, and SiO spectra.....	132
38.	The energy levels of the ground state of OH and the Zeeman pattern for the hyperfine transitions.....	144
39.	The total power spectra of the four hyperfine transitions of the ground state of OH.....	150
40.	The circularly polarized spectra for the 1665 MHz transitions of OH.....	153

41.	The circularly polarized spectra for the 1612 MHz transitions of OH.....	155
42.	The S3 spectrum for the 1612 MHz transition of OH with a model Zeeman pattern superimposed on it.....	156
43.	The total power spectrum for the 1612 MHz transition of OH.....	157
44.	A schematic diagram of a one dimensional maser amplifying three independent transitions.....	166

C H A P T E R I

INTRODUCTION TO STAR FORMATION AND THE ORION NEBULA

1.1 Star Formation

The formation, evolution, and destruction of stars determine the morphology and evolution of galaxies and hence the appearance of the universe. The process which creates stars also controls the formation of planets. Thus, an understanding of star formation is essential to both the most universal and most local aspects of astronomy. Yet little is known of how stars form.

The evolution of a star from a cloud of gas to the main sequence is determined by its mass, angular momentum, magnetic field, elemental abundances, molecular concentrations, and proximity to supernovae and density waves. Mass is undoubtedly the most important factor in determining how a star will evolve, and how that star will affect the appearance and evolution of the galaxy. The most massive stars ($> 10 M_{\odot}$) create new elements and stir the interstellar medium. Stars of a few solar masses, in their red giant stage, produce most of the light in a galaxy. Small stars ($< 1 M_{\odot}$) lock up gas for the age of the universe. The initial mass function (IMF), i.e., how many stars of each mass form initially, is poorly known. The best estimate for the local neighborhood is $n(m) = m^{-2.35}$ (Salpeter 1955). Furthermore, since the evolutionary pattern of a protostar changes so greatly with increasing mass, stars greater than $9 M_{\odot}$ must be considered separately from those of smaller mass.

Our galaxy converts a few solar masses of gas into stars each year (see, for example, Mezger and Smith 1977, or von Hoerner 1975). This is done in dark clouds where $T = 10^\circ\text{K}$ and $n_{\text{H}_2} = 1000 - 10\,000\text{ cm}^{-3}$, and in molecular clouds where $T = 30 - 300^\circ\text{K}$ and $n_{\text{H}_2} = 10^4 - 10^6\text{ cm}^{-3}$. For a cloud to collapse, its mass must exceed the Jeans mass ($M_J = 30 T^{3/2} \rho^{-1/2} M_\odot$ for ρ in particles cm^{-3} and T in $^\circ\text{K}$). For the temperature and density of the atomic interstellar medium, the necessary mass is a few thousand solar masses. Open clusters fall in this mass range. In dark clouds and molecular clouds, the necessary mass is only a few tens of solar masses. The IMF is determined by fragmentation of the gas cloud and the mechanism which stops fragmentation. Hoyle (1953) developed the following scenario for fragmentation. As a large gas cloud contracts and the density increases, subsections of the cloud become unstable to gravitational collapse and separate out. These subsections then contract and fragment again. However, as the density becomes very high, radiation is trapped inside the cloud. The cloud becomes hotter and the increased pressure eventually prevents further collapse and fragmentation. At this point, the mass of the star is determined and the object becomes a protostar. Larson (1969) showed that the collapse of a cloud is non-homologous. A gravitationally bound cloud of uniform density develops a central condensation which reaches stellar conditions without further fragmentation. Thus, a cloud fragments only once. Recent theoretical studies (for a review see Larson 1977) which include the effects of angular momentum, non-spherical geometry, and other nearby protostars, indicate that the

result of the single fragmentation is a cloud of a few solar masses which becomes a single star, a binary star, a multiple star system of a few stars, a star with a disk of gas, or a ring of gas which breaks up into a few smaller clouds. The path of evolution is determined by conditions at the time of fragmentation.

A fragment of $1 M_{\odot}$ with initial conditions of $n_{\text{H}_2} = 10^5 \text{ cm}^{-3}$, $T = 10^\circ\text{K}$, and a diameter of 20 000 a.u. will evolve as follows (Larson 1969). For 400 000 years the entire cloud collapses slowly while a hot, dense core develops. This core collapses quickly and for the next 100 000 years the remaining matter falls onto it. The gravitational energy makes the core extremely luminous. For the next 50 million years the cloud evolves towards the main sequence. When the temperature in the core reaches 10 million degrees, fusion starts and the cloud becomes a zero age main sequence star.

A $60 M_{\odot}$ cloud evolves very differently (Appenzeller and Tscharnuter 1974). Once a dense core develops (again after 400 000 years), it contracts so quickly that fusion starts in only 20 000 years. Dust and gas still surround the core and continue to fall onto it, increasing its mass and adding to its luminosity. After another 20 000 years, radiation pressure expels the remainder of the cloud. Of the original $60 M_{\odot}$, only $17 M_{\odot}$ remain in the star. Between the formation of the core and the expulsion of the envelope, the star would appear as a cool, luminous, infrared source.

All massive stars form in OB associations (Roberts 1957). These OB associations, which are usually near molecular clouds, are composed

of subgroups containing about 12 stars (Blaauw 1964). The subgroups have different ages and Blaauw suggested that they show a progression of star formation in time and space. Star birth begins at one edge of a cloud and proceeds through the cloud with a speed of 5 km s^{-1} . Different perspectives on this process can be seen in Orion A and M17. In M17 the OB associations are strung out across the sky, while in Orion the path of star formation is along the line of sight. In Orion, the third and fourth subgroups of the OB association, the optical nebula, and the molecular cloud overlap (Figure 1) (Kutner et al. 1977). In this dissertation I will use the molecular masers to follow this sequence of star formation into the Kleinmann-Low nebula which may become the next subgroup of young stars in the Orion association.

Elmegreen and Lada (1977) and Lada (1980) explain the sequence of star formation by having one OB association of stars, via a shock wave, trigger the next generation of OB stars. Hence, star formation propagates through a cloud in the following manner. A group of OB stars creates an HII region, e.g., the Orion nebula, which soon becomes ionization bound. A shock front precedes the ionization front into the dense molecular cloud. In the intershock region, the gas has been compressed from 10^3 to 10^5 particles cm^{-3} . It is also heated from 15°K to some higher temperature and then cooled to 100°K . The higher density encourages star formation, and the higher temperature ensures that more massive stars form. Silk (1977) shows that the initial mass function is proportional to T^3 or a higher power. The

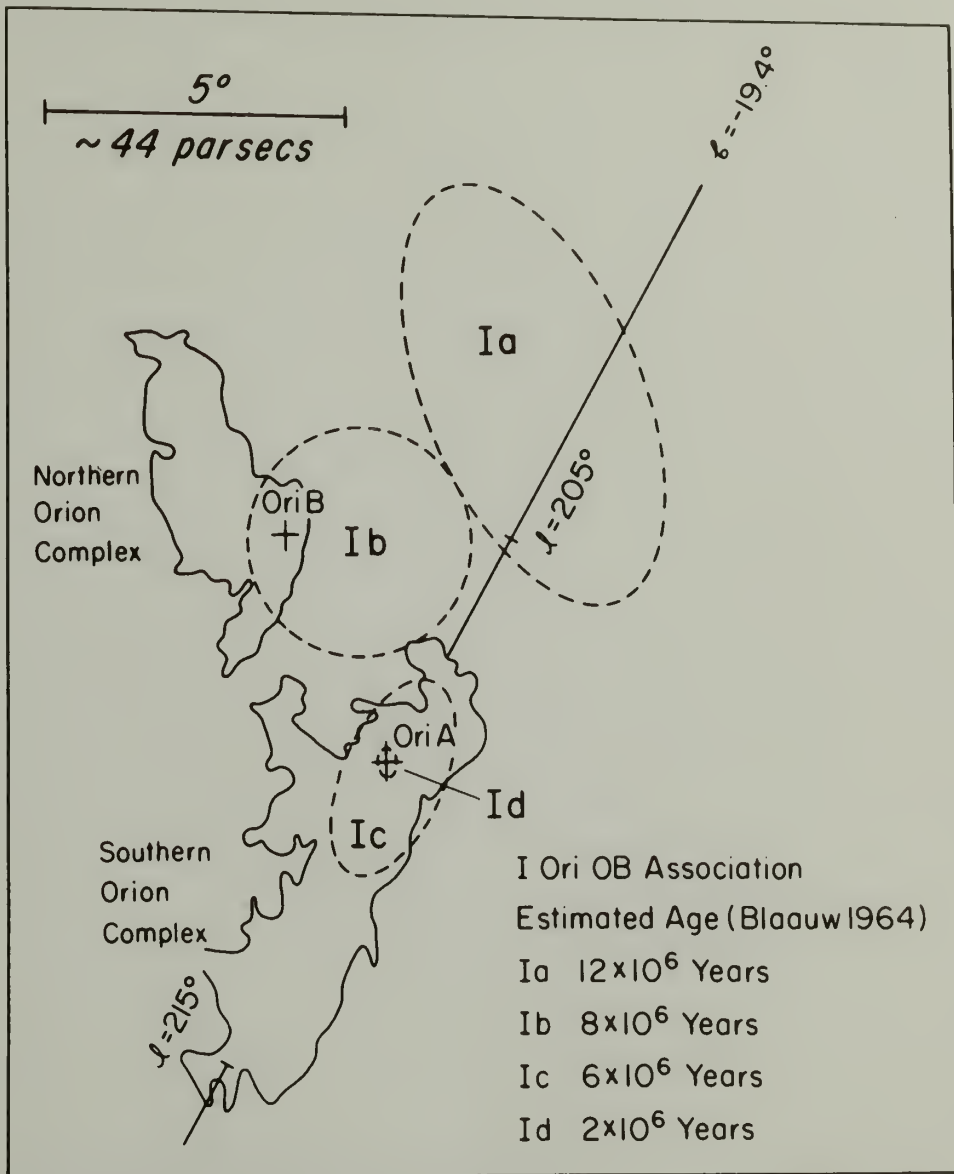


Fig. 1. The Orion molecular complexes and the four subgroups of the OB association I Ori. The molecular complexes are as delineated in Figure 4. The dashed lines are boundaries which roughly enclose the subgroup members as identified by Blaauw (1964). (Reproduced with permission of the authors from Kutner, M. L., Tucker, K. D., Chin, G., and Thaddeus, P. 1977, *The Astrophysical Journal*, 215, 521, copyright 1977.)

dust in this region, which would also have a temperature of 100°K , may be the source of the IR radiation. In a few million years the shock, having propagated 10 - 20 pc, will have snowplowed gas with an initial density of 1000 cm^{-3} to a density high enough for gravitational collapse. The shock slows down, but the stars are dense enough to continue into the cloud. (The Trapezium stars, with a radial velocity of 11 km s^{-1} (Johnson 1965), are moving toward the molecular cloud at 3 km s^{-1} .)

Once a star becomes optically thick to cooling radiation, it contracts to the main sequence in a Kelvin-Helmholtz time scale. This is less than $4 \cdot 10^4$ years for an O star (Herbig 1960). Hence, before one OB association has finished shocking the gas, another one takes over. The original shock now has OB stars on both sides of it and is dispersed. The dense neutral fragments which are observed may be the remainders of the intershock gas. The final disruption of the cooled, post shock region (CPS) may account for the dispersive velocity of OB associations. The Orion groups do seem to be expanding slightly (Cannell and Ianna 1977). The sequence of star formation is thus:

- (1) the formation of protostars accompanied by masers and IR sources in the CPS,
- (2) the formation of a dense HII region where $n = 10^5 \text{ cm}^{-3}$ in the CPS,
- (3) the movement of the new stars into the unshocked cloud and the creation of a low density HII region where $n_{\text{H}_2} = 1000 \text{ cm}^{-3}$,
- and (4) the disruption of the CPS revealing the stars.

The newest Orion OB associations are closer together than the old. This can be explained by either the shocks propagating into the central, denser

regions of the cloud, or the cloud as a whole contracting slowly with time. The shock propagates along the magnetic field lines. Such propagation, which increases the density but not the field strength, encourages star formation since the mass necessary for gravitational collapse varies with the cube of the field and the inverse square of the density (Mestel 1971). The propagation of the shock along the magnetic field accounts for the OB associations lying along the galactic plane. The shock to form the initial OB association may come from a supernova, a cloud-cloud collision, a density wave, or a cloud collapse.

Since young objects (OB stars and HII regions) define spiral arms, perhaps differential rotation of the galaxy creates spiral structure by wrapping up these strings of newly formed stars. If this is the case, spiral structure is the result, and not the cause, of star formation. Alternatively, if spiral density waves cause the initial shock, one would expect to see a correlation between the direction of wave propagation and the location of star formation regions in the clouds. The edge of the cloud on which stars form would change at the co-rotation point in the galaxy.

This analysis of sequential star formation is suitable only for massive stars. Some other mechanisms must create stars smaller than $9 M_{\odot}$ and later than spectral type B3. Many T Tauri stars are seen without HII regions or ionization fronts. These stars may form in the denser, cooler cloud regions by collapse and fragmentation as suggested by Hoyle (1953). Such T associations may have formed long

before the OB stars disrupted the cloud to reveal them (Mezger and Smith 1977).

At some points in the star formation process, conditions are suitable for stimulated emission from various molecules. Genzel and Downes (1977a) propose that the emission from water vapor masers associated with star formation comes from a cloud of dust surrounding a 10 to 30 M_{\odot} zero age main sequence star. The core of the cloud has evolved so fast that it reaches the main sequence while the outer part of the cloud is still collapsing. Radiation pressure halts the collapse of the dust at 100 to 1000 a.u. A dust bound HII region forms and expands. It is preceded by a shock driven by the gas pressure. When the shock reaches 1000 a.u., conditions between the shock front and ionization front are suitable for H_2O masers. The low velocity spectral features, i.e., those with velocities within 20 $km\ s^{-1}$ of the cloud velocity, are either (1) globs of gas where the density, temperature, and chemical composition are right to invert the maser population, or (2) lines of sight through a large region with an inverted population along which the velocity gradient is favorable to stimulated emission. The star also has an intense stellar wind which accelerates subclouds to hundreds of kilometers per second. The high velocity maser features, i.e., those whose velocity is more than 20 $km\ s^{-1}$ from the cloud velocity, come from these condensations. Alternatively, the high velocity features could occur where the wind hits the surrounding cloud (Genzel et al. 1979a). The present evidence supporting this model and the analysis leading to this model

and alternative models are given in the Appendix: "Detailed Models for the Water Vapor Observations".

1.2 The Orion Region

1.2.1 Overview. The Orion nebula and molecular cloud, 460 pc from the sun (Allen 1973), is one of the nearest (Figure 2) and certainly the best studied site of current star formation. The Orion region, which includes the entire constellation, shows the sequence of star formation in time and space. The observations of this region are concentrated within Barnard's Loop (about $10^\circ - 20^\circ$ in diameter (Figure 3)). Within that loop are the large molecular clouds seen in CO (Figure 4) which stretch for several degrees. The OB associations (Figure 1) also span several degrees. These groups of stars are 10 million years old and seem to be dispersing. On a smaller scale is the great Orion nebula (Figure 5) studied in all regions of the spectrum. The optical nebula is also called M42 and NGC 1976. The radio source is called Orion A, W10, or G209.0 - 19.4. The nebula has a mass of $100 M_\odot$ ionized by θ^1_C , an O6 star. (θ Orionis is a double star consisting of θ^1 and θ^2 . θ^1 is actually the four stars (or more) of the Trapezium designated ABCD in order of increasing R.A.) The age of the nebula is $10^4 - 10^6$ years (Isobe 1973). The nebula is approximately $10'$ in diameter with a bright core about $1'$ in size (Figure 6). A bright bar is seen southeast of the Trapezium near θ^2 . M43 is another HII region only $7'$ away from M42 (Figure 5). It is ionized by a B0.5 star and is not connected with M42 physically (Pankonin, Walmsley, and Harwit 1979).

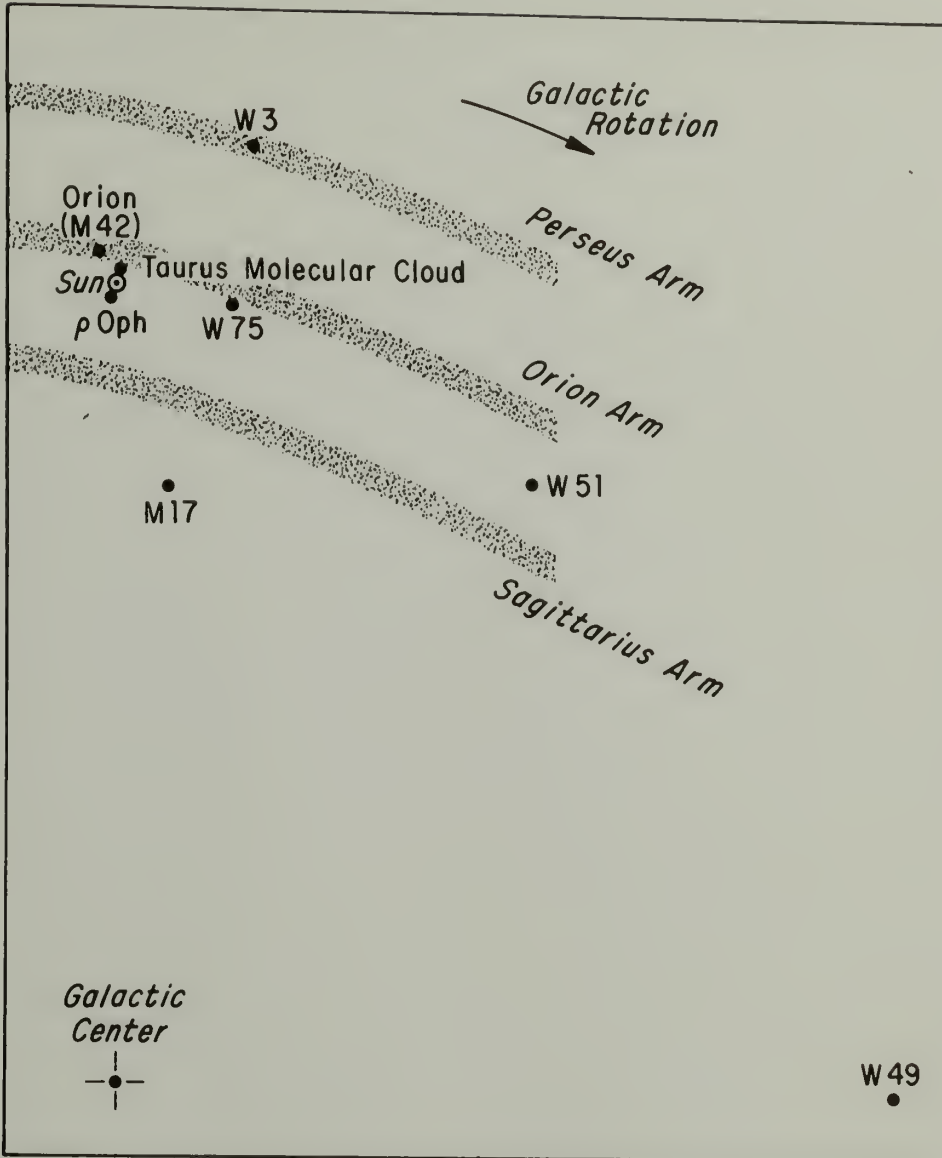


Fig. 2. A map of the galaxy showing several maser sources and sites of star formation.

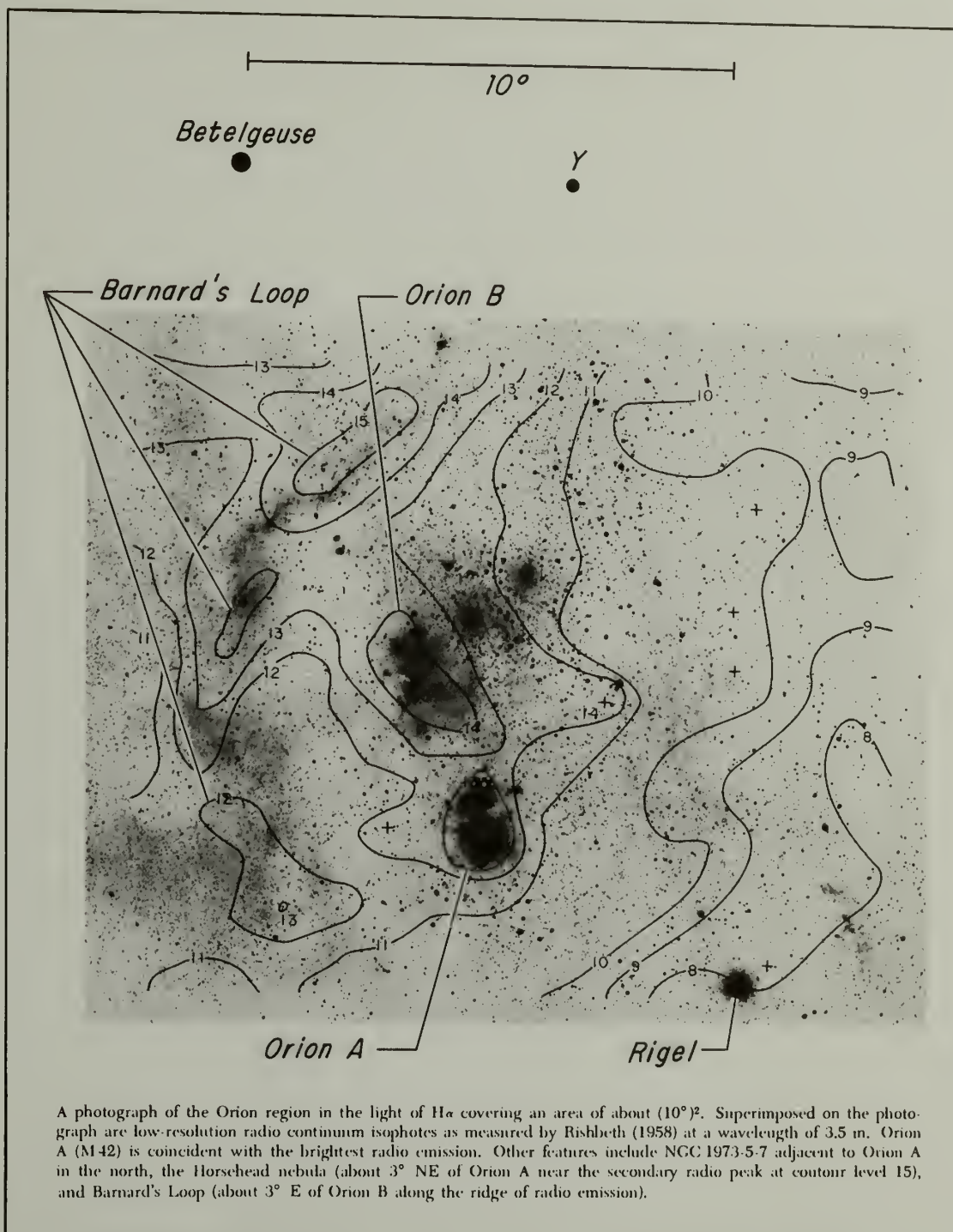
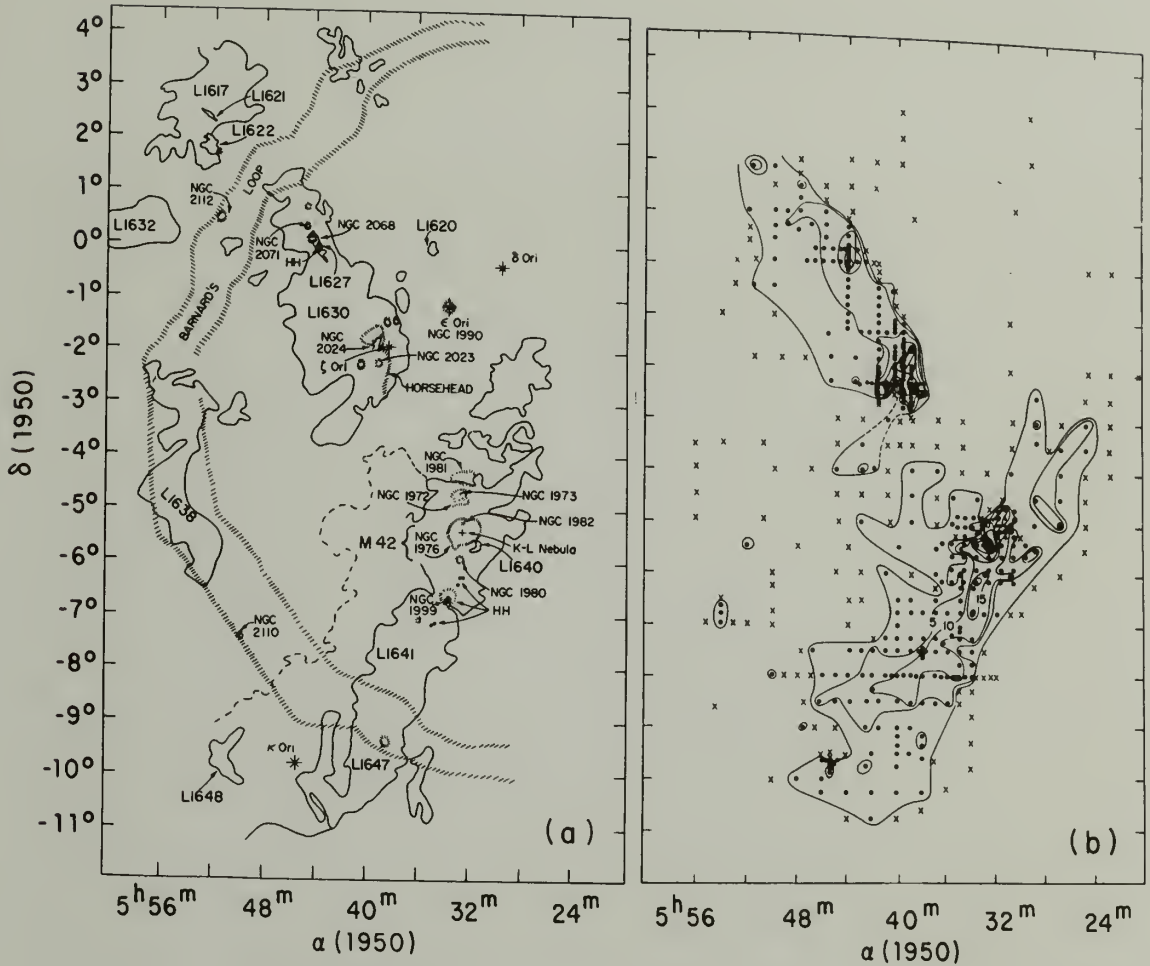


Fig. 3. The constellation Orion. (Photograph and caption reproduced courtesy of the authors and the Publications of the Astronomical Society of the Pacific from Balick, B., Gammon, R. H., and Hjellming, R. M. 1974, *Pub. astron. Soc. Pacific*, **86**, 616, copyright 1974.)



(a) Summary of CO observations in Orion. (a) A sketch of the salient features visible on the Palomar Sky Survey prints. The hatched boundaries indicate the boundaries of optical emission or reflection nebulosity. The approximate boundaries (from the blue print) of dust clouds, designated by Lynds (L) numbers, are given in solid lines; dashed line, a lower extinction edge of L1641. Herbig-Haro objects are designated by HH.

(b) CO distribution in the Orion region from the Texas (16 foot) observations. Intensities are given as line radiation temperatures, corrected for atmospheric attenuation and beam efficiency as described by Davis and Vanden Bout (1973). (T_a in the direction of the KL nebula is 75 K.) Filled circles (approximately the HPBW), CO detections. Crosses, negative results, corresponding to upper limits of 1-2 K. (In the vicinity of the KL nebula, the density of points was too great to show all positions observed.) The contour interval is 5 K in peak radiation temperature, with the outermost contour representing the limit of detections.

Fig. 4. The region of Orion within Barnard's loop. (Reproduced with permission of the authors from Kutner, M. L., Tucker, K. D., Chin, G., and Thaddeus, P. 1977, The Astrophysical Journal, 215, 521, copyright 1977.)

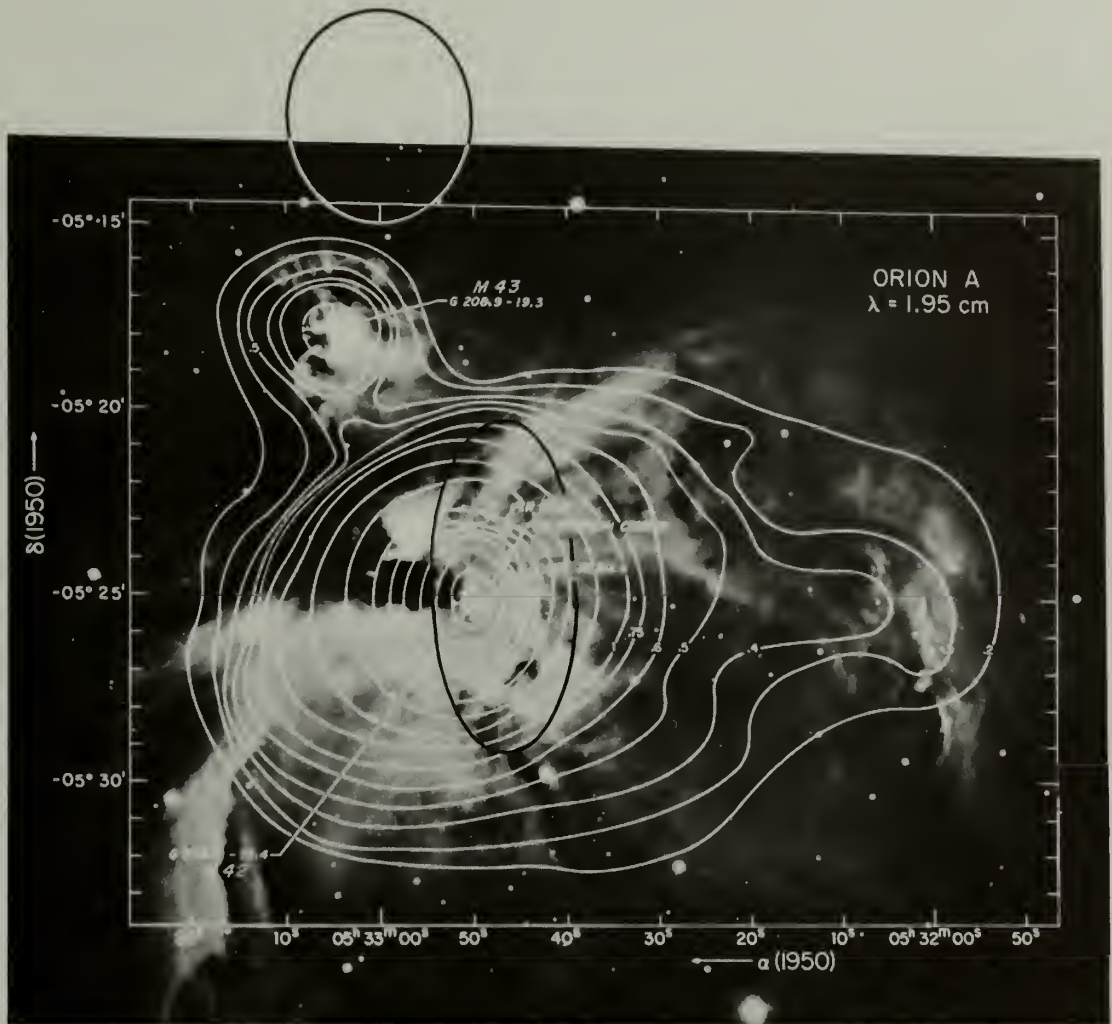
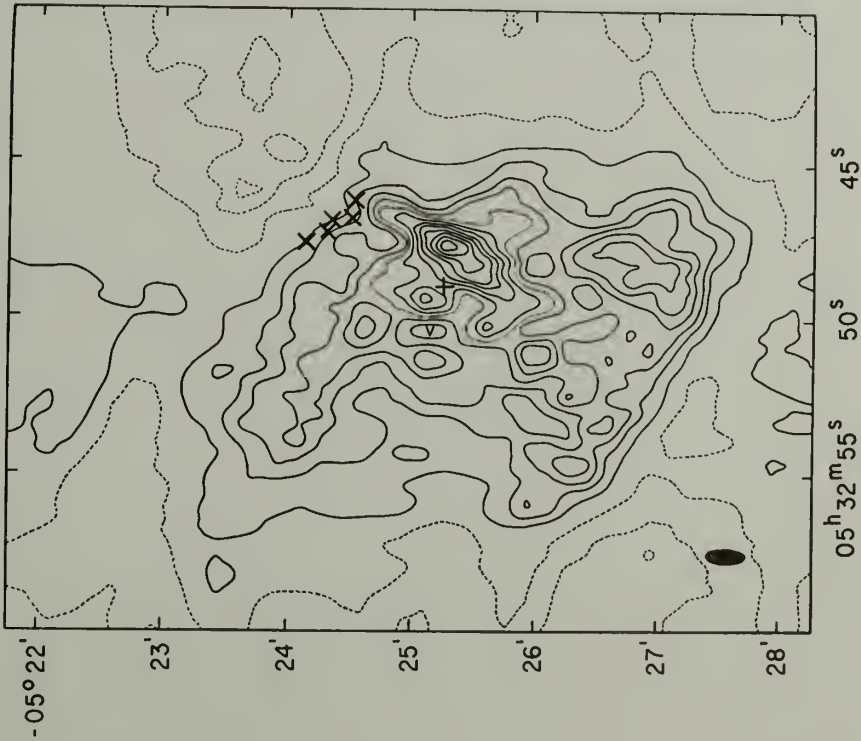


Fig. 5. The Orion nebula. The radio continuum isophotes at 1.95 cm with a spatial resolution of 2' (Schraml and Mezger 1969) are superimposed on a red Mount Palomar plate. (Reproduced with permission of the authors from Schraml, J. and Mezger, P. G. 1969, The Astrophysical Journal, 156, 269, copyright 1969.) The dark ellipse in the center marks the approximate extent of the central ridge of the Orion Molecular Cloud 1 (Liszt et al. 1974). The ellipse at the upper right indicates the extent of the Orion Molecular Cloud 2 (Gatley et al. 1974).

Fig. 6. The core of the Orion nebula with 5 GHz continuum contours. (Reproduced with permission of the authors and the Royal Astronomical Society from Martin, A.H.M., and Gull, S. F. 1976, M.N.R.A.S., 175, 235, copyright 1976). The x's mark the position of five H₂O masers (Forster et al. 1978).



The cleaned map superimposed on an optical photograph of the central region of the Orion Nebula taken by Münch & Wilson (1962). The contour interval is 77 K. The crosses were used to align the overlay.



The cleaned map after 400 beamshape subtractions. The contour interval is 58 K, and the restored beamshape is shown in the lower left. The cross marks the position of the exciting star, θ^1 Orionis. The coordinates are for epoch 1950.0.

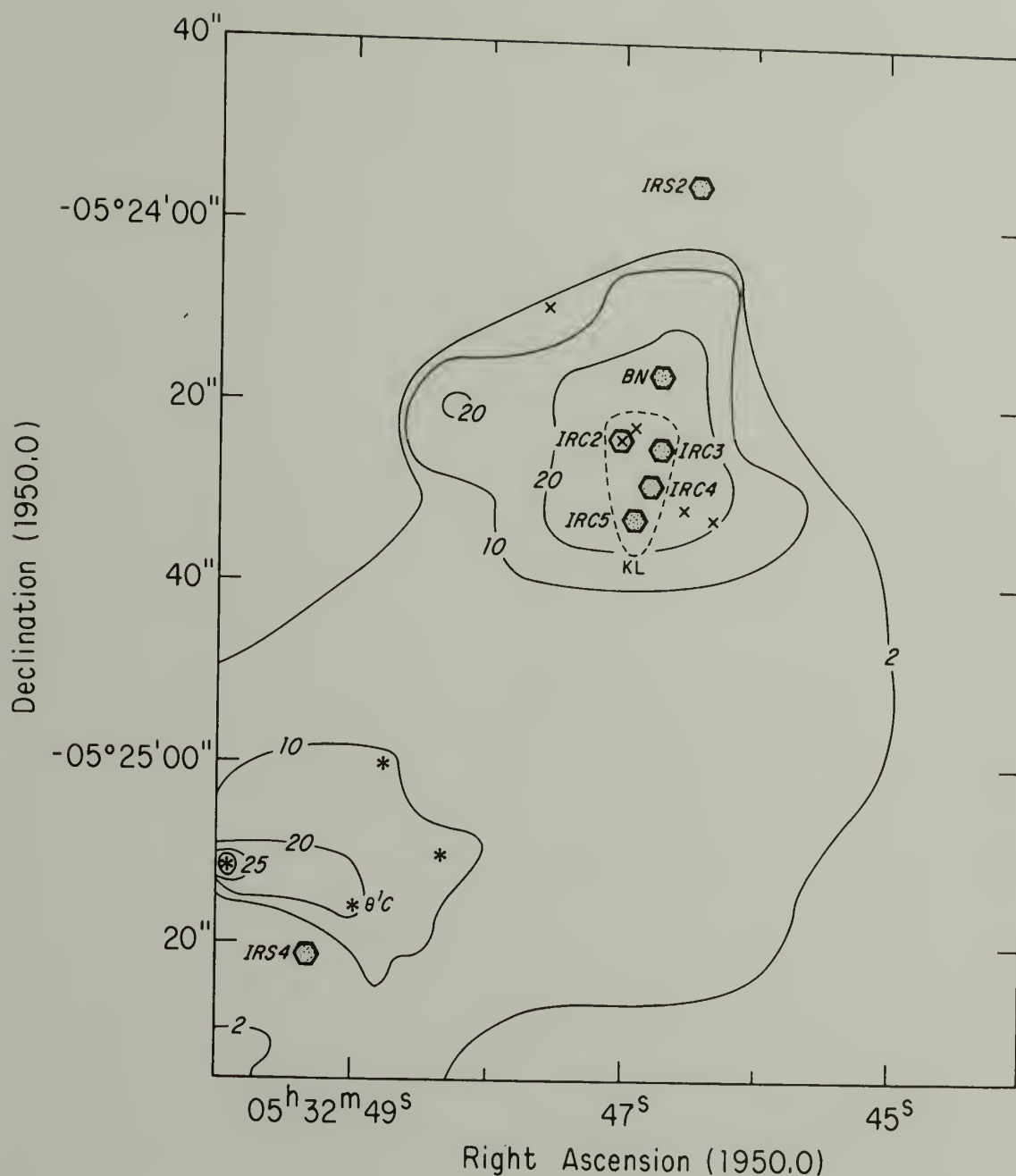


Fig. 7. The Kleinmann-Low nebula complex and the Trapezium (*). The extent of the Kleinmann-Low nebula is indicated by the dashed line. The positions of the water vapor masers (x) are from Forster et al. (1978), the positions of the compact infrared (IRC) sources (hexes) are from Rieke, Low and Kleinmann (1973), the positions of IRS2 and IRS4 (other compact IR sources) are from Wynn-Williams and Becklin (1974), and the 13.1 micron contours ($6 \times 10^{-8} \text{ W cm}^{-2} \text{ micron}^{-1} \text{ sr}^{-1}$) are from Gehrz, Hackwell, and Smith (1975).

Fig. 8. The Kleinmann-Low nebula with the absolute positions of the H₂O, OH, SiO, and CH₃OH masers, the compact IR sources, and the H₂ contours. The data are given in Table 1. Each large circle indicates the position and size of a methanol maser. Each hex indicates the position and upper limit to the size of a compact IR source. The contours of the 2.12 micron emission from H₂ are in units of $1.2 \cdot 10^{-4}$ ergs s⁻¹ cm⁻² sr⁻¹. The ·'s with heavy error bars are the H₂O masers. The northeast region and the southwest region of the map contain most of the H₂O masers. The filled triangles are the compact OH masers of Hansen *et al.* (1977) (Chapter IV) while the open triangles are the extended OH masers of Raimond and Eliasson (1969). The solid vertical bar is the area over which the SiO masers are spread. The absolute positions of the SiO masers have a one sigma error of 12" in each direction. The sizes of H₂O, OH, and SiO masers on the map are much smaller than the symbols which represent them.

All the maps of Chapter III except Figure 28 have the same scale as this map. The infrared sources are shown on those maps to facilitate comparison among the maps. All the VLBI positions of the water vapor masers in Chapter III are relative to the position of the 10.8 km s⁻¹ feature shown here.

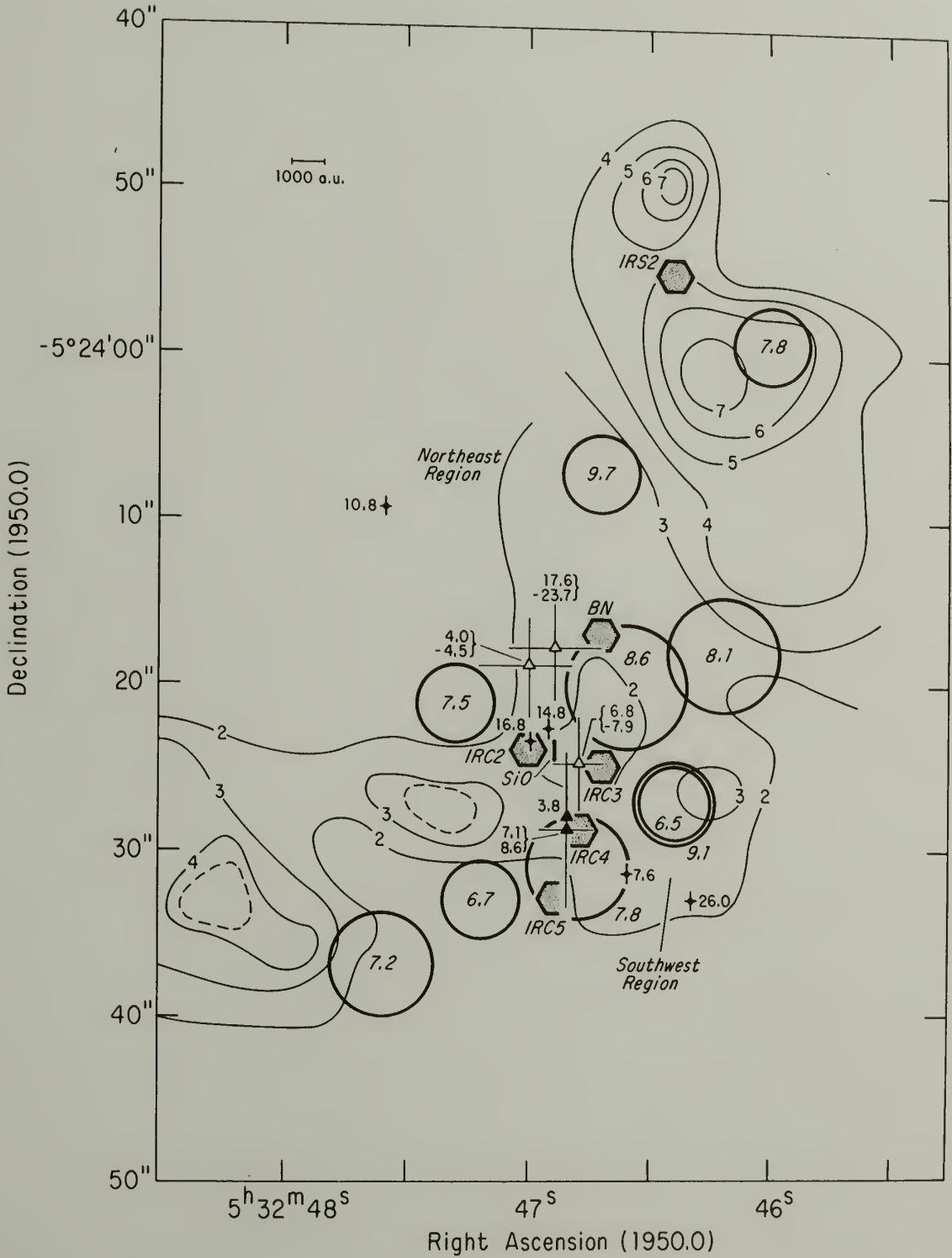


TABLE 1
Absolute Positions of Emission Sources Towards Orion A

Material	Frequency	Velocity or name (km s ⁻¹)	Flux (Jy)	R.A.		DEC		Size 0"00	Reference
				5 ^h s	32 ^m s	-5° "	24' "		
H ₂ O	22235 MHz	7.6		46.59 ± 0.02		31.5 ± 0.5			Forster et al. 1978
		10.6		47.58		9.3			
		14.8		46.92		22.6			
		16.8		47.00		23.5			
		26		46.33		33.0			
OH	1665 MHz	3.8	16					0"025	Chapt. IV & Hansen et al.
		7.1	44					0"05	1977
		8.6	38	46.85 ± 0.1		29 ± 5		0"045	
		4.0-4.5	~20	47.0 ± 0.2		19 ± 3			Raimond & Eliasson
		6.8-7.9	~20	46.8 ± 0.1		25 ± 3			1969
		17.6-23.7	~20	46.9 ± 0.2		18 ± 3			
SiO	43122 MHz	16.8	1160	46.9 ± 0.8		24 ± 12			Moran et al. 1977
			others within 0"1		1.1			0"02	Genzel et al. 1979b
CH ₃ OH	25018 & 25125 MHz	6.5	18	46.4 ± 2		27 ± 4		≤6"	Matsakis et al. 1980
		6.7	20	47.2		33		≤6"	
		7.2	54	47.6		37		6"	
		7.5	24	47.3		21		≤6"	
		7.8	24	46.0		23'59		≤6"	
		7.8	40	46.8		24'31		6"	
		8.1	58	46.2		18		7"	
		8.6	24	46.6		20		8"	
		9.1	14	46.4		27		≤6"	
		9.7	14	46.7		7		≤6"	

Table 1, continued

Material	Frequency	Velocity or name (km s^{-1})	Flux (Jy)	R.A. $5^{\text{h}} 32^{\text{m}}$ s s	DEC $-5^{\circ} 24'$ " "	Size $0''00$	Reference
H_2	2.12 μm	Pk 1	75*	46.2 \pm 2	02 \pm 2		Beckwith et al. 1978
		2	50*	48.3	34		
		3	33*	47.3	26		
		4	32*	46.2	27		
		5		46.4	23'50		
		BN	30*	46.7	24'17		
Dust	10.5 μ (21 μ)	BN	260(420)	46.7	17	<2"	Rieke, Low & Kleinmann 1973
		IRC 2	30(110)	47.0	24	<3"	
		3	15(170)	46.7	25	<5"	
		4	23(250)	46.8	29	<3"	
		5	10(110)	46.9	33	<5"	
Dust	<20 μ	IRS 2		46.4	23'55		Wynn-Williams and Becklin 1974
		4		49.3	25'21	<3"	

* $10^{-4} \text{ erg s}^{-1} \text{ cm}^{-2} \text{ sr}^{-1}$

M43 is more deeply imbedded in the molecular cloud and may be a better example of a spherical HII cloud. This list of objects illustrates the complexity of the Orion nebula region and of the number of objects which overlap. Orion B (W12), the radio counterpart to NGC 2024, is a compact HII region located at $5^{\text{h}} 39^{\text{m}}$, $-1^{\circ} 56'$ (Grasdalen 1974) (Figures 3 and 4).

The optical nebula is a bulge on the surface of a huge molecular cloud which has a mass of 10^3 to $2 \cdot 10^4 M_{\odot}$ (Zuckerman 1973, Balick, Gammon and Hjellming 1974). The cloud is not seen optically, but is abundant in molecular line radiation. It extends over several tens of minutes on the sky and has an H_2 density of 10^5 cm^{-3} . Liszt et al. (1974) mapped this cloud in CO and found a $4' \times 9'$ central ridge (Figure 5). The central ridge is often called the Orion molecular cloud (OMC-1). Emission from other molecules in the cloud is usually confined to a region smaller than the CO ridge.

Gatley et al. (1974), observing between 1.6 and 20 microns, found a second cloud, OMC-2, $12'$ north and $1'$ east of OMC-1 at $\alpha(1950) = 5^{\text{h}} 32^{\text{m}} 59^{\text{s}}.1 \pm 0^{\text{s}}.1$, $\delta = -5^{\circ} 12' 10'' \pm 1''$ (Figure 5). At 2.2 microns the source shows five components, each a few seconds in diameter, within a $1'$ region. The total IR luminosity is less than $500 L_{\odot}$. No optical counterparts to the compact IR sources are seen. CO emission peaks within $1'$ of the IR sources but extends over $6'$.

The densest part of OMC-1 is the Kleinmann-Low nebula (KL) (Kleinmann and Low 1967) shown in Figure 7. It was first detected in the infrared where it has an extent of $10'' \times 20''$. Twenty seconds northwest of the Kleinmann-Low nebula is an infrared point source,

the Becklin-Neugebauer (BN) object (Becklin and Neugebauer 1967). It is in this region, BNKL, where stars are now forming. Hall et al. (1978) determined that BN is a B protostar surrounded by a compact HII region. The IR luminosity of the BNKL is about the same as the optical luminosity of the Orion nebula. This implies that the energy source is probably a collection of O and B stars.

The Kleinmann-Low nebula also contains the H_2O , OH, SiO and CH_3OH masers (Figure 8). They are the smallest and densest products of star formation which are seen before the star itself appears. These masers are a useful tool with which to study a protostar. Masers probe deeper into the clouds, and show smaller structure than any other source of radiation. This dissertation will use the information about these masers to probe conditions in the prestellar clouds during the last stages of star formation.

1.2.2 The Large CO Clouds. Kutner et al. (1977) made a large scale map of CO at 115 MHz in the Orion region. They found the two clouds shown in Figure 4. The southern one stretches over 7° southeast from the KL and the OB associations. It is parallel to the galactic plane at -19.4° and lies along Gould's belt. The northern complex extends northeast from Ori B (NGC 2024) for 5° . In each cloud, the densest part is near the OB associations. The southern complex seems to be rotating with the southern edge receding at only 5 km s^{-1} while the northern edge is receding at 11 km s^{-1} . Since HI is probably less than 5% of the total cloud mass, the 21 cm maps do not delineate the cloud, but they do show the rotation. Alternatively, the differential

velocity could be due to collapse along a line (perhaps a magnetic field line). The rotation of the clouds, which is opposite to galactic rotation, requires a rather special geometry at the time of formation. The stars of the association do not show this rotation. Perhaps the process of star formation causes the rotation. (For a more detailed discussion, see Kutner et al. 1977.) Both clouds end in the region of Barnard's Loop. Intensity measurements, and the virial theorem applied to the measured rotation, require the mass of the southern cloud to be $10^5 M_{\odot}$. The mass of the northern complex is $6 \cdot 10^4 M_{\odot}$.

1.2.3 The Orion Nebula. The Orion nebula (Figure 5) is one of the best studied objects in the sky. Observations range from the radio to the x-ray region of the spectrum. For example, Jaffe and Pankonin (1978) find three carbon recombination lines at 10 GHz with velocities of 6, 8.5, and 11 km s⁻¹. They propose the following model for the nebula: the neutral cloud and HII region have a velocity of 8 km s⁻¹. The dark bay and the dark lane between M42 and M43 are part of the neutral cloud which still wraps around the HII region. The carbon lines come from the HI-HII boundaries which are expanding at 2.5 km s⁻¹ into the neutral region. Hence, the 6 km s⁻¹ line comes from the HI-HII boundary which is moving towards us into the back side of the dark bay, the 11 km s⁻¹ line, from the far HI-HII boundary which is moving into the molecular cloud, and the 8.5 km s⁻¹ line, from the dark lane between M42 and M43 where the motion of the HI-HII boundary is perpendicular to the line of sight.

Schraml and Mezger (1969) observed a number of galactic HII regions and determined important parameters for them. They found that most HII regions of high surface brightness were surrounded by extended emission from ionized hydrogen. Most of the regions were elliptical at wavelengths of 1.95 cm which implied that obscuring dust determined the optical shape. This is certainly true in Orion A. The Orion nebula is unusual in that the ionizing stars are visible. Most HII regions are surrounded by dust which is long lasting even in the intense radiation. Schraml and Mezger observed HII regions with densities as high as 10^4 cm^{-3} . HII regions of higher densities would not be detected at 15 GHz because the spectra turn over above this frequency. Schraml and Mezger propose a model in which a compact HII region with a density greater than 10^4 cm^{-3} forms about an O star. This region expands and its density drops to 100 cm^{-3} . The mass in a compact HII region is a few solar masses while the mass in an extended HII region is a few hundred solar masses. This mass is much lower than the few thousand solar masses in stars in an association. Such a low mass implies that, contrary to current beliefs, star formation consumes much more than one percent of the original cloud mass. The extended HII region may be the remnant of earlier compact HII regions or it may be ionized by many later type stars (i.e., late B type stars).

1.2.4 The Compact Core of the Nebula. Martin and Gull (1976) mapped the inner region of the Orion nebula at 5 GHz with a resolution of $7'' \times 20''$ by combining synthesis data from the Cambridge one-mile telescope and the Owens Valley interferometer (Figure 6). They do not

explain how they determined the absolute position of the source or how accurately it is determined. However, by superimposing their map on an optical photograph of the inner region of the Orion nebula, it is easy to line up a radio continuum gradient with the bright optical bar southeast of the Trapezium. Martin and Gull see a less steep gradient at the position of the line of H_2O masers which they interpret as an ionization front seen on edge. However, since there are several gradients as steep as the one which coincides with the H_2O masers, the correlation is not impressive. Furthermore, the unusual uv coverage and the combination of data from two interferometers make the ridges suspect. Martin and Gull conclude that the dust and gas are well mixed as did Dopita, Isobe, and Meaburn (1975). However, Martin and Gull cannot tell if the dust exists in neutral intrusions or is truly mixed with the gas. The dark bay is definitely in the foreground. Martin and Gull also find a deficiency of ionized gas in the dark bay region, contrary to the results of Schraml and Mezger (1969). The electron density in the compact nebula, assuming a uniform distribution, is 6000 cm^{-3} . Since the gas is clumped, the true density is probably 10^5 cm^{-3} (Osterbrock and Flather 1959).

The Orion nebula is not spectacular when compared to other HII regions. Its compact core has a diameter of half parsec and a mass of a few solar masses. Other compact HII regions (e.g., W49 and W51) have diameters of several parsecs and contain several hundred solar masses. If the Orion nebula were not so close, we would hardly notice it. However, it is probably a more typical star formation site than the spectacular HII regions.

1.2.5 The Orion Molecular Cloud and the Central Ridge. Behind the optically bright HII nebula lies the dark molecular cloud. Liszt et al. (1974) found that the cloud has a 4' x 9' central ridge in CO. ^{13}CO and CS showed a smaller ridge and the ^{13}CO , being optically thin, showed peaks 7' north and 5' south of the ridge, each as strong as, but smaller than, the central peak. Formaldehyde (H_2CO) (Evans, Plambeck and Davis 1979), ammonia (NH_3) (Barrett, Ho, and Myers 1977), methanol (CH_3OH) (Gottlieb et al. 1979, Hills et al. 1975, Liszt 1974, Kutner et al. 1973), and IR (Rieke, Low and Kleinmann 1973) also have a smaller central ridge than the CO. The observations are best explained if the gas is in clumps 10" to 30" in diameter. The ridge in CO blends into a much larger background source at 20% of the peak intensity. The line widths are 6 km s^{-1} in the ridge and only 4 km s^{-1} in the background cloud. The ridge has a velocity gradient of 2 km s^{-1} over a range of 3' ($1.4 \cdot 10^{-12}$ radians s^{-1}). Liszt et al. (1974) attribute this gradient to rotation, while Ho and Barrett (1978) attribute it to two clouds in collision. The background gas in all directions about the central ridge has a velocity of 8.5 km s^{-1} , which is hard to understand if there are two separate clouds.

The kinetic temperature in the ridge is about 70°K (see the references in the preceding paragraph). The mass of the central ridge, as determined for emission from several molecules by different methods, is at least a few hundred solar masses, and is probably $500 M_\odot$ including the denser clumps (again see the references in the preceding paragraph). The cloud is not supporting itself by rotation, and Liszt et al. (1974) feel that expansion or contraction offer the best

explanation of the line shapes. They show that the H_2 density must be at least 10^4 cm^{-3} and is most probably $2 \cdot 10^5 \text{ cm}^{-3}$. Therefore, the central ridge is similar to the Orion nebula, which has a maximum density of 10^5 cm^{-3} , and a total mass in stars and gas, including the extended HII region, of $500 M_{\odot}$.

Kutner, Evans, and Tucker (1976), while mapping H_2CO , found a cloud with a total mass of $7000 M_{\odot}$ and $n_{H_2} = 5 \cdot 10^4 \text{ cm}^{-3}$ connecting OMC-1 and OMC-2. The connecting cloud is $1.5 \times 5 \text{ pc}$ (about 30' long). The velocity pattern suggests rotation with much of the angular momentum in the orbital motion of OMC-1 and OMC-2.

1.2.6 The Kleinmann-Low Nebula

1.2.6.1 Infrared. Within the central ridge is the Kleinmann-Low nebula (KL), which was first detected by $22 \mu\text{m}$ IR measurements (Kleinmann and Low 1967). Its size, $10'' \times 20''$, is not much smaller than the CH_3OH or NH_3 emission regions mentioned in the previous section. Rieke, Low and Kleinmann (1973), observing at 5, 10.5, and $21 \mu\text{m}$, determined that BN was less than $2''$ in diameter. They also found four more compact ($<5''$) IR sources in KL (Figure 7). They estimated that KL had a total luminosity of $5 \cdot 10^4 L_{\odot}$ whereas IRE1 (the optical HII region) had a luminosity of $1.1 \cdot 10^5 L_{\odot}$.

Werner et al. (1976), observing Orion at 20, 50, and $100 \mu\text{m}$ found the central N-S ridge had a temperature of 85°K near its core and 55°K to the north. The individual compact IR components are not resolved at these wavelengths. The luminosity of the KL between 10 to $1000 \mu\text{m}$ is $7 \cdot 10^4 L_{\odot}$. The luminosity of the OMC excluding the

KL is $10^5 L_{\odot}$. The difference between the luminosity estimated from the near infrared measurements and that measured in the far infrared suggests that the near infrared radiation from the compact objects is absorbed by the surrounding dust and reemitted in the far infrared. The energy source must be in or on the surface of the ridge, for, if it were not, the heating efficiency would be so low that the total luminosity would have to be $10^6 L_{\odot}$, which is greater than the luminosity of the entire optical nebula. The IR emission extension to the south they attribute to heating of the molecular cloud by the Trapezium. This requires that the Trapezium stars be only 0.1 pc from the molecular cloud, a distance which agrees with the 0.1 to 0.3 pc determination of Schiffer and Mathis (1974) from optical data. Further south near Ori θ^2 is an IR ridge which coincides nicely with the edge of the optical core of the HII region (Becklin *et al.* 1976).

1.2.6.2 High velocity molecular emission. The spectra of many molecules from Orion A can be divided into a spike feature at 8 km s^{-1} with a FWHM of 5 km s^{-1} and a plateau feature centered at the same velocity but with a FWHM of 40 km s^{-1} (e.g., Zuckerman and Palmer 1975). The narrow component comes from the entire OMC while the plateau emission is seen only from the KL. The broad feature has strong emission from molecules such as H_2S , SO , SO_2 , and SiO , while the narrow feature shows its strongest emission from organic molecules. Since most of the molecules have similar excitation energies but are not seen at the same locations, the concentration of the molecules is probably different.

Kwan and Scoville (1976) and Zuckerman, Kuiper, and Rodriguez (1976) detected high velocity CO emission as far as $\pm 75 \text{ km s}^{-1}$ from the spectral peak at 8 km s^{-1} . The high velocity data implies that the KL is evolving with a time scale of 10^3 rather than 10^{4-5} years. Kwan and Scoville conclude that a very energetic event, possibly a supernova, has taken place in the cloud recently and that the BN object is the result. The gas motion alone has 0.1% of the energy of a supernova. There is no other source in the region now which could provide the energy necessary to drive the shock. Although a supernova would not disrupt the cloud, it should have other effects which are not seen.

Scoville (1980) has analyzed the high velocity CO emission from the region of KL. He reports that CO can be seen out to $\pm 50 \text{ km s}^{-1}$ over a region only $37''$ ($20\,000 \text{ a.u.}$) in diameter which coincides with the KL. He estimates the H_2 density in the high velocity flow to be $10^5 - 10^6 \text{ cm}^{-3}$. The optical depth is low because of the large velocity spread. From the smoothness of the emission, he considers large scale ordered motion necessary. Since there is no velocity gradient across the source, rotation is unlikely. Furthermore, the large mass, i.e., $10^4 M_\odot$, required for rotation or gravitational collapse at $\pm 50 \text{ km s}^{-1}$ should have other observational effects which are not seen. The different chemical concentrations in the spike and plateau regions are hard to understand if the surrounding gas is just being drawn into the plateau region. The relative strength of SiO implies that the core of gas is hot enough to destroy organic molecules. The

line profiles are best fit by an expanding gas cloud with $v \propto r$, $n \propto r^{-3}$, and $T_{\text{ex}} \propto r^{-1/2}$.

Several observations of the $J = 3 \rightarrow 2$ transition of CO at 870 μm (346 GHz) (e.g., Phillips et al. 1977) show the plateau emission region has $T > 100^\circ\text{K}$, $m > 100 M_\odot$, $n_{\text{CO}} > 6 \cdot 10^{18} \text{ cm}^{-2}$, $n_{\text{H}_2} \geq 10^{23} \text{ cm}^{-2}$, and $n_{\text{H}_2} \geq 5 \cdot 10^5 \text{ cm}^{-3}$. The broad wings in CO are much more pronounced at 870 μm than at 115 GHz (2600 μm). The plateau emission at 870 μm has a velocity width of 40 km s^{-1} , and a spatial extent of 37" in declination and less than 22" in R.A. It is centered at $5^{\text{h}} 32^{\text{m}} 47^{\text{s}.7} \pm 0^{\text{s}.3}$ and $-5^\circ 24' 19'' \pm 5''$. The cloud associated with the emission spike has $T = 75^\circ\text{K}$, a velocity width of 6 km s^{-1} , and is optically thick over 2' or 3'. Since the high velocity wings do not show absorption by the bulk of the cloud, the high velocity gas must lie near the front of the cloud. Wilson, Downes, and Bieging (1979) have detected high velocity NH_3 with a width of 50 km s^{-1} from a region less than 20" in diameter coincident with the Kleinmann-Low nebula.

1.2.6.3 Molecular hydrogen. Joyce et al. (1978) measured the H_2 spectrum of the Kleinmann-Low nebula at 2.12 μm and found a velocity of $9.5 \pm 4 \text{ km s}^{-1}$ and a FWHM of less than 30 km s^{-1} . Because the H_2 emission is best explained by collisional excitation at a high temperature, Kwan and Scoville (1976) proposed that the H_2 emission came from a shock front preceding the high velocity gas. If this is true, the high velocity gas has somehow slowed. The shock velocity must be greater than 7 km s^{-1} to excite the H_2 , but less than 25 km s^{-1} to avoid dissociating the gas.

Beckwith et al. (1978) have published high resolution maps of the OMC-1 region in H_2 emission at $2 \mu m$ (Figure 8). The emission comes from an irregular area about $40''$ in size centered on the Becklin-Neugebauer, Kleinmann-Low (BNKL) position. There are 5 peaks, none of which exactly coincides with the BNKL area. Two peaks are on the eastward IR ($10 \mu m$) extension from KL found by Gehrz, Hackwell and Smith (1975). The two strongest peaks are near, but not coincident with, the IR source IRS2 shown in Wynn-Williams and Becklin (1974). The shape of the H_2 emission does not match the shape of the 5 GHz continuum emission measured by Martin and Gull (1976). In general, the H_2 emission peaks are near to, but not coincident with, the emission peaks at other frequencies. The H_2 excitation temperature determined by various methods is $2000^\circ K \pm 300^\circ K$. The density must be greater than 10^5 cm^{-3} for the H_2 to be thermalized, and since the optical depth requires only $n_{H_2} = 10^{19} \text{ cm}^{-2}$, the thickness is one a.u. The H_2 thus exists in a thin hot sheet. A natural conclusion is that the H_2 emission comes from a region where the high velocity gas hits the neutral cloud.

1.2.7 Masers. The Orion A maser emission region is shown in Figure 8. The absolute positions of the H_2O masers, the OH masers, the SiO masers, and the infrared point sources are indicated on the map and listed in Table 1.

1.2.7.1 The water vapor masers. The water vapor emission from Orion comes from an area $20\ 000$ a.u. in diameter. Most of the maser positions are clustered within a region 5000 a.u. in diameter in the

southwest corner of the larger region. (See any of the maps of Chapter III.) There are approximately 30 strong spectral features between -10 km s^{-1} and $+30 \text{ km s}^{-1}$. Weak, unresolved maser emission probably exists at every velocity in that range. There are also weak features as far as 100 km s^{-1} from the strong features. The water vapor masers show time variations on a scale of a few weeks to years. The H_2O masers are the subject of Chapter III.

1.2.7.2 The hydroxyl masers. Hydroxyl maser emission is seen at 1612 MHz and 1665 MHz from the ${}^2\Pi_{3/2}$ $J = 3/2$ state and at 6035 MHz from the $J = 5/2$ state. The OH masers are not as widely spread in space as the H_2O masers. The velocity range is 30 km s^{-1} . The intensity varies on a time scale of months to years. OH is discussed in more detail in Chapter IV.

In Chapter III, I will present evidence which will associate the 1665 MHz OH masers at 3.8, 7.1, and 8.6 km s^{-1} with one cluster containing H_2O masers at the same velocity, and the 1665 MHz OH masers between -8 and -5 km s^{-1} and between $+15$ and $+23 \text{ km s}^{-1}$ with another set of H_2O masers. This is contrary to the results of Mader et al. (1975 and 1978) which showed that the 1665 MHz OH masers, the 1667 MHz OH masers, and the 22 GHz H_2O masers were all spatially separate.

1.2.7.3 The silicon oxide masers. Snyder and Buhl (1974) detected SiO maser radiation in the $v = 1, J = 2 \rightarrow 1$ transition at 86 GHz from Orion A in 1973. Maser emission was soon detected from the $v = 1, J = 3 \rightarrow 2$ transition at 129.4 GHz (Davis et al. 1974), the $v = 1, J = 1 \rightarrow 0$ transition at 43.1 GHz (Thaddeus et al. 1974), and

the $v = 2, J = 1 \rightarrow 0$ transition at 42.8 GHz (Buhl et al. 1974). The SiO spectra are dominated by a peak around -5 km s^{-1} and a peak around $+18 \text{ km s}^{-1}$. Double peaks are often found in SiO maser spectra with each peak consisting of several lines. The Orion SiO masers are the only ones known which are not obviously associated with an evolved star. However, the velocity separation of the peaks in Orion is much greater than the velocity separation of the peaks in any other SiO source. Each of the two strong peaks in the $v = 1, J = 1 \rightarrow 0$ (43 GHz) spectrum of Orion shows weak maser pedestal emission (Snyder et al. 1978). Zuckerman (1979) found SiO maser emission at all velocities from -18 km s^{-1} to $+29 \text{ km s}^{-1}$. Moran et al. (1977) looked for rapid variations in Orion but found none on a time scale of 30 minutes to 4 days. The SiO maser at 16 km s^{-1} dropped to half its previous intensity over several years.

My recent VLBI observations (Genzel et al. 1979b) have determined the diameter of the SiO masers to be about 10 a.u. Those observations also showed that the masers at -5 and $+18 \text{ km s}^{-1}$ are coincident ($<0.3''$) which suggests that all the emission is associated with a single object.

1.2.7.4 The methanol masers. Barrett, Schwartz, and Waters (1971) first detected methanol maser emission toward Orion A in 5 transitions between 24.9 and 25.3 GHz. Hills, Pankonin, and Landecker (1975) found three methanol masers in Orion A at 7.24, 7.80, and 8.20 km s^{-1} with a FWHM of 0.4 km s^{-1} and an intensity between 71 and 151 Jy. They also detected a broad component with FWHM of 1.4 km s^{-1} . There is no polarization ($<20\%$). Each velocity feature is seen in at

least three transitions ($J = 6, 7, 4$) with similar intensities. The energy of these levels ranges over a factor of two. The theoretical reason for the agreement in intensity is that the energy of the methanol maser transition is comparable (10%) to the energy separation between other levels (Lees 1973). Buxton et al. (1977), in a search of 132 other maser sources, found no methanol masers. They could have detected the Orion methanol masers at a distance of 2.5 kpc.

Barrett, Ho, and Martin (1975) discovered time variations of a factor of three in the 25 GHz methanol masers during 1973-1974. Tucker and Kutner (private communication to Barrett, Ho, and Martin 1975) also found time variations of a factor of 2 in CH_3OH at 84.52 GHz. In addition to the features reported by Hills et al., Barrett, Ho, and Martin (1975) found features at 7.0, 8.5, and 9.5-10.0 km s^{-1} . Temporal variations in different J levels of the same velocity feature, and of different velocity features, are roughly correlated. The time scale for intensity variations is a month.

Matsakis et al. (1980), using the Hat Creek interferometer, found the ten velocity components shown in Figure 8. The size, position, and flux determined from the $J = 6$ and $J = 7$ rotational levels are given in Table 1. Note that the methanol masers are a thousand times weaker than the H_2O masers. The methanol masers have a velocity range of only 4 km s^{-1} . Again, there is no exact correlation in position with other types of emission in or around the Kleinmann-Low nebula. The brightness temperature is approximately 1000°K. The populations of the measured rotational levels, i.e., $J = 2, 3, 4, 6, 7$,

and 10, are close to thermodynamic equilibrium at 110°K. Since all the methanol masers show correlated time variations on a time scale of months, and since the masers are light months apart, they are probably pumped by infrared radiation from a single source.

1.2.8 Stars

1.2.8.1 The Becklin-Neugebauer source. Until recently, IR observations could not exclude the possibility that the Becklin-Neugebauer object was a highly reddened supergiant. From the ratios of Brackett α , Brackett γ , and Pfund γ lines, Hall et al. (1978) determined that the BN object is a B0 or B1 protostar surrounded by a compact HII region and an expanding shell. Ninety percent of the emission in these hydrogen lines comes from an area within 1''4 of the BN object. A substantial amount of the IR continuum must come from dust. The radial velocity of the lines is 21 km s^{-1} . Since the authors doubt that the true velocity of BN is 13 km s^{-1} higher than the molecular cloud, they postulate that the emission has been reflected off dust, or that absorption has shifted the apparent center of the line. The Brackett α emission has weak wings out to $\pm 100 \text{ km s}^{-1}$.

Hall et al. also measured two CO absorption patterns. One at 9 km s^{-1} they attribute to the large molecular cloud. The other at -18 km s^{-1} they attribute to the edge of an expanding shell. The temperature of the 9 km s^{-1} cloud is 100°K, and that of the -18 km s^{-1} cloud, 85°K. These low temperatures require that the clouds be far from the star. There are no broad absorption lines corresponding to the emission peak. From the emission velocity and the radius of the

plateau emission region (20"), they estimate an age of the object of 1800 years. Chelli, Lena, and Sibille (1979), using a speckle interferometer at 3.45 μm and 4.78 μm , determined that BN had a halo of 0".9 FWHM, and a central source less than 0".10 in diameter. They attribute this geometry to a dust shell about a B3 star with a luminosity of 2900 L_{\odot} .

1.2.8.2 An evolved star. Although Orion A is certainly a region of active star formation, a number of observations force one to consider the possibility of an evolved star in the region. First, Orion A is the only HII region which has SiO masers. Second, the high velocity gas and the phenomena connected with it (e.g., H₂ emission) are unusual.

Moran et al. (1977), having determined the positional coincidence (within 2") of all the SiO velocity features and some of the H₂O features at similar velocities, proposed that the maser emission came from an expanding shell of gas about an evolved star which was losing mass. A diagram of a shell model star and the resulting spectra are shown in Figure 9. Radiation pressure on the grains accelerates the gas and establishes a velocity gradient in the gas. The velocity varies directly, and probably linearly, with radius. The longest path for maser amplification in such a shell is on the line of sight to the star. Along other paths the velocity gradient limits the amplification. Consequently, the most intense radiation comes from the gas directly approaching and receding from us. This creates the double peak spectra indicative of a shell structure. The SiO masers require the greatest excitation and lie close to the stellar surface. The H₂O

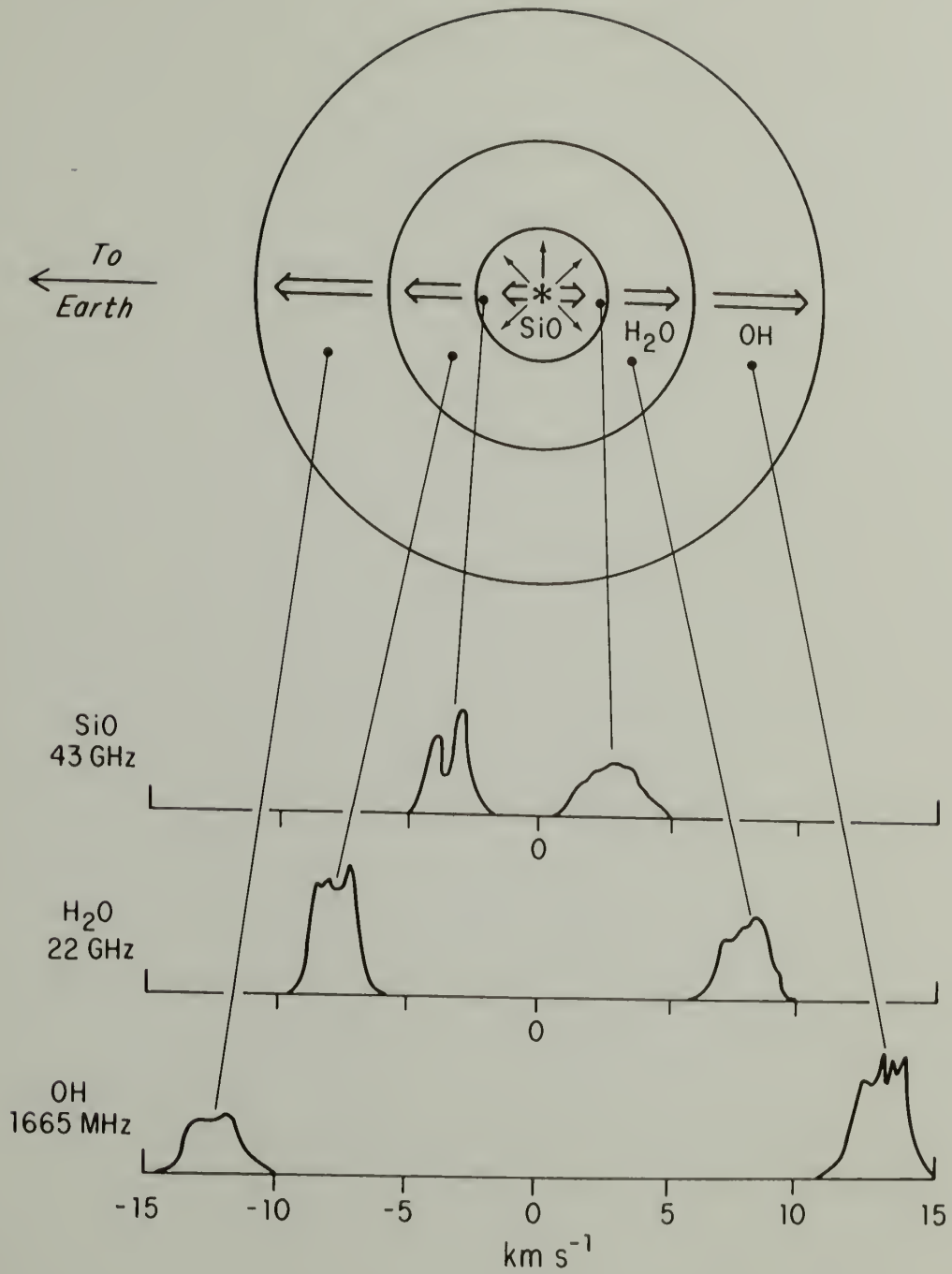


Fig. 9. An idealized schematic diagram of a shell source and the resultant spectra. The actual Orion spectra are shown in Figure 37.

masers, which require less excitation, arise in a shell further from the star. The OH masers, which have the lowest excitation temperatures, are farthest from the star. Since the velocity increases with radius, the velocity separation of the OH peaks is greater than the separation of the H₂O peaks, which is greater than the separation of the SiO peaks. No methanol masers are associated with the shell source. Observations presented in this dissertation support the shell model.

1.3 Summary

This chapter has reviewed the Orion region of the sky and related it to the sequence of star formation. In the Orion region are clouds of CO extending over several degrees. In one of them is the Orion molecular cloud with an extent of tens of minutes of arc. The optical nebula is a bulge on the surface of this cloud where young stars have ionized the gas from which they formed. Within the molecular cloud is a central ridge with an extent of 4' x 9' and a density of 10^5 cm^{-3} . The densest part of that ridge is the Kleinmann-Low nebula which is the next site of star formation in the Orion region. In the remainder of this dissertation I will use the molecular masers to probe the conditions in and around the Kleinmann-Low nebula. Most of the masers are associated with the final stage of star formation, although a few are probably associated with an evolved star. Before discussing the observations and interpretations, I will review the data analysis techniques.

CHAPTER II

DATA ANALYSIS

2.1 Theory

Observational astronomers measure the intensity of radiation from the sky as a function of position, frequency, polarization, and time. Very long baseline interferometry (VLBI) gives the most precise relative positions with an accuracy better than a milliarcsecond. The concept of VLBI is not simple, and the use of VLBI becomes more complicated with the desire for more accuracy. The principles of VLBI in general and spectral line VLBI in particular are discussed by Moran (1973). Several VLBI recording systems have been reviewed by Moran (1976). In this Chapter I will review the theory and techniques which I used to determine the size and position of the maser sources.

The response of an interferometer to radiation from a point on the sky may be expressed as a complex function whose magnitude is proportional to the intensity of the radiation and whose phase is determined by the total delay between the signal from the two telescopes. In the ideal case, all the delay is due to the extra travel time of the radiation to the second telescope. The phase due to this geometric delay is

$$\phi = \frac{f}{c} \bar{B} \cdot \bar{S} \text{ turns} \quad 2.1$$

where S is the unit vector pointing to the source, B is the baseline

vector pointing from telescope 1 to 2, f is the observing frequency and c is the speed of light. In a coordinate system with the Z axis parallel to the earth's instantaneous pole, the X axis in the direction of 0° longitude and the Y axis in the direction of 90° west longitude,

$$\phi(f) = \frac{f}{c} [\sqrt{(X^2 + Y^2)} \cos \delta \cos (\text{IHA}) + Z \sin \delta] \quad 2.2$$

where IHA (interferometer hour angle) = UTC + GASTM - α - $\tan^{-1} (Y/X)$, UTC is the coordinated universal time, GASTM is the Greenwich apparent sidereal time at midnight UTC, α and δ are the right ascension and declination of the source, and X , Y , and Z are the separations of the telescopes in meters along each axis. If α and δ are the only uncertain quantities in Equation 2.2, and if the phase determined from Equation 2.2 is removed from the data, then the residual phase must be due to an offset of the source from the assumed position, i.e.,

$$\Delta\phi = \frac{\partial\phi}{\partial\alpha} \Delta\alpha + \frac{\partial\phi}{\partial\delta} \Delta\delta \quad 2.3$$

or

$$\Delta\phi = \left[\frac{f}{c} \sqrt{(X^2 + Y^2)} \sin (\text{IHA}) \right] \cos \delta \Delta\alpha + \left[-\frac{f}{c} \sqrt{(X^2 + Y^2)} \sin \delta \cos (\text{IHA}) + \frac{f}{c} Z \cos \delta \right] \Delta\delta.$$

The quantities in brackets are called u and v . They are the projected baseline components in wavelengths. The fringe spacing, i.e., the separation between lines on the sky whose interferometer phases differs

by 2π , is $0.206 (u^2 + v^2)^{-1/2}$ for u and v in millions of wavelengths. From a series of measurements of $\Delta\phi$ at different times, $\Delta\alpha$ and $\Delta\delta$ may be found by a least squares fit.

In practice, of course, the determination of the phase is much more complicated. There are instrumental phase drifts, errors in the clocks at each station, errors in the local oscillator rates, atmospheric effects, and errors in the baseline determination. A major effort in VLBI is to remove all contributions to the phase which are not due to source structure.

During a VLBI observation up to 10^{11} bits of information per day can be recorded at each telescope. From that data one wants to determine the size and position of a few tens of velocity features. The data processing of a VLBI observation is described in Section 2.2, map making in Section 2.3, and size determination in Section 2.4. The observational results from each epoch will be the velocities, intensities, and relative positions of the masers. The size of the masers were determined from the 1978 observations which had baselines most suitable for that measurement.

2.2 Processing

The original Mark II VLBI recording system was described by Clark (1973). The use of the Mark II processor was described by Hansen (1977). In essence, the VLBI processor delays the signal from the second telescope by the appropriate time, removes from that data stream the phase effect for a number of specified parameters, and then cross

correlates the two data streams for 192 complex delay channels. The processor Fourier transforms the cross correlation functions into cross power spectra discarding the sideband not observed, and applies the fractional bit shift correction, i.e., a frequency dependent phase shift which compensates for finite resolution in the digitized delay. The result is a cross power spectrum in velocity of 96 complex channels. The processor also autocorrelates the data for each individual telescope for 96 time delays to obtain a total power spectrum in velocity for each telescope. All these correlations are summed for 0.2 seconds and then recorded on magnetic tape for further processing by a general purpose computer.

The first postprocessing program scans the 0.2 second records from the processor for bad records and discards them. The good records are averaged coherently for a time interval which is limited by factors discussed later in this paragraph. The advantage to coherent averaging is that the signal to noise ratio increases as the square root of the integration time. The disadvantage is that, since the phase of the signal varies with time, the average of the real part and the average of the imaginary part each approach zero. Some part of the phase change is systematic. The change which is due to errors detected in the analysis of the data, e.g., baseline, frequency, or source position errors, may be removed by rotating the phase through the correct angle. The remaining systematic phase changes are used to determine source structure. Imperfections in the frequency standards or changes in the atmosphere introduce random phase noise into the

data which limits the averaging time to a duration much shorter than the coherence time, i.e., the time over which phase noise will reduce the amplitude of the correlated signal to one half its true value. The coherence time varies from a minute to an hour depending on the stability of the frequency standards (hydrogen masers or rubidium clocks) at the telescope, the atmosphere, and the observing frequency of the observation. Typically, the cross power spectra are averaged for one or a few seconds. The autocorrelation data, having no phase information, may be averaged for a few minutes. The only limitation on the integration time of the autocorrelation data is the time scale for any change in the spectra due to telescope drift, changes in the weather, or changes in the receivers. In addition to improving the signal to noise ratio of the data, averaging also reduces the amount of data which must be stored and further processed. This slightly averaged data is usually the least postprocessed data which is kept. If no source has been detected in the cross correlation data by this point in the processing, the experiment is probably a failure. If sources have been detected, several additional processing techniques can be applied to the data.

The most important technique is phase referencing. At this point in the processing, the intensity of a few maser features in the spectrum should be far above the noise intensity and the phase of the data for that velocity channel should be determined by the radiation rather than by the noise. The phase of a strong feature contains all the systematic errors and random phase noise discussed above. The

phase reference technique subtracts the phase of a reference channel, i.e., one with a strong signal from a single point source, from all the other channels. This removes the random phase noise, and reduces the phase effect of many other errors. The remaining phase is due mainly to source structure and clock errors.

$$\phi = \frac{f}{c} [\bar{\mathbf{B}} \cdot (\bar{\mathbf{S}} - \bar{\mathbf{S}}_0)] + (f - f_0) \tau_{\text{error}} \quad 2.4$$

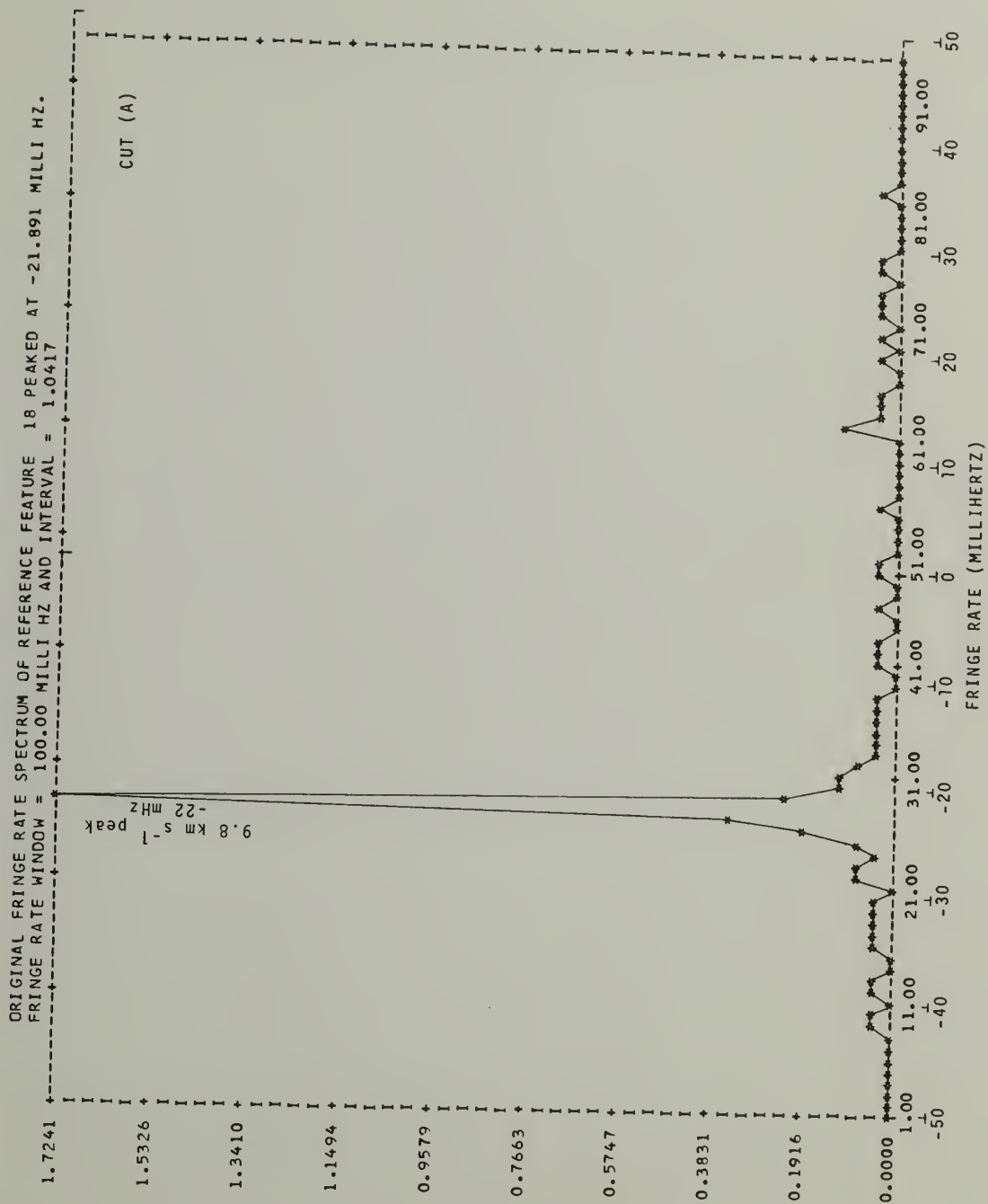
where f is the sky frequency, $\bar{\mathbf{S}}_0$ points to the reference feature, $\bar{\mathbf{S}}$, to the feature whose phase is measured, f_0 is the sky frequency of the lower edge of the bandpass, and τ_{error} are other errors in the delay. The gross effects of delay errors may be estimated and removed if strong, unresolved continuum sources were observed. Since phase referencing removes all the random phase fluctuations, one may integrate far beyond the coherence time. However, all information on the absolute position of the source is lost, and, if the reference feature has any spatial structure, it is superimposed on all the other velocity features.

The phase still contains second order effects from errors in the parameters. There are also 2π ambiguities in the phase. If one takes the time derivative of the phase, then all the error effects which are independent of time, as well as the 2π ambiguities, disappear. This time derivative is called the phase rate or the "fringe rate". The major contribution to the relative fringe rate is the change in u and v as the earth rotates. In practice, the fringe rate

is determined by Fourier transforming a time sequence of complex amplitudes for a particular velocity. The result is the fringe rate spectrum for that velocity. Two examples of fringe rate spectra are shown in Figure 10. Each fringe rate spectrum was obtained by Fourier transforming a 96 point time sequence of data for one velocity, each point of which was the signal averaged for 10 seconds. The fringe rate of the strongest peak in a spectrum is taken as the fringe rate for that velocity. (The peak in the 9.8 km s^{-1} fringe rate spectrum is at -22 MHz (channel 28).) A table of the fringe amplitude as a function of fringe rate and velocity is shown in Figure 11. Each vertical column is a fringe rate spectrum for a velocity channel, and each horizontal line is a velocity spectrum at a particular fringe rate. The data shown in Figure 10(a) and (b) are cut (A) and (B) in Figure 11. Figure 12(a) shows a velocity spectrum at one particular fringe rate (the rate of the peak amplitude for the 9.8 km s^{-1} channel). It is cut (C) on Figure 11. Figure 12(b) is the velocity spectrum at the fringe rate of the peak amplitude for the 8.8 km s^{-1} channel. It is cut (D) in Figure 11. Figure 13 shows the amplitude (bottom) and fringe rate (top) of the peak in the fringe rate spectrum of each velocity channel. The points shown in Figure 13 are enclosed in boxes in Figure 11.

Averaging the data is done in several stages. The data is averaged and the residual fringe rate analyzed to determine why it is not zero. If the cause of the fringe rate can be determined, the phase effect of that cause is removed from the data. This reduces the fringe

Fig. 10. Sample VLBI fringe rate spectra of Orion from 1978 November 2 1125 UT for (a) the 9.8 km s^{-1} velocity channel, and (b) the 8.8 km s^{-1} velocity channel. The horizontal axis is the fringe rate in MHz. The amplitude is in units of the geometric mean of the system temperatures of the two telescopes.



ORIGINAL FRINGE RATE SPECTRUM OF REFERENCE FEATURE 22 PEAKED AT -0.010 MILLI HZ.
FRINGE RATE WINDOW = 100.00 MILLI HZ AND INTERVAL = 1.0417

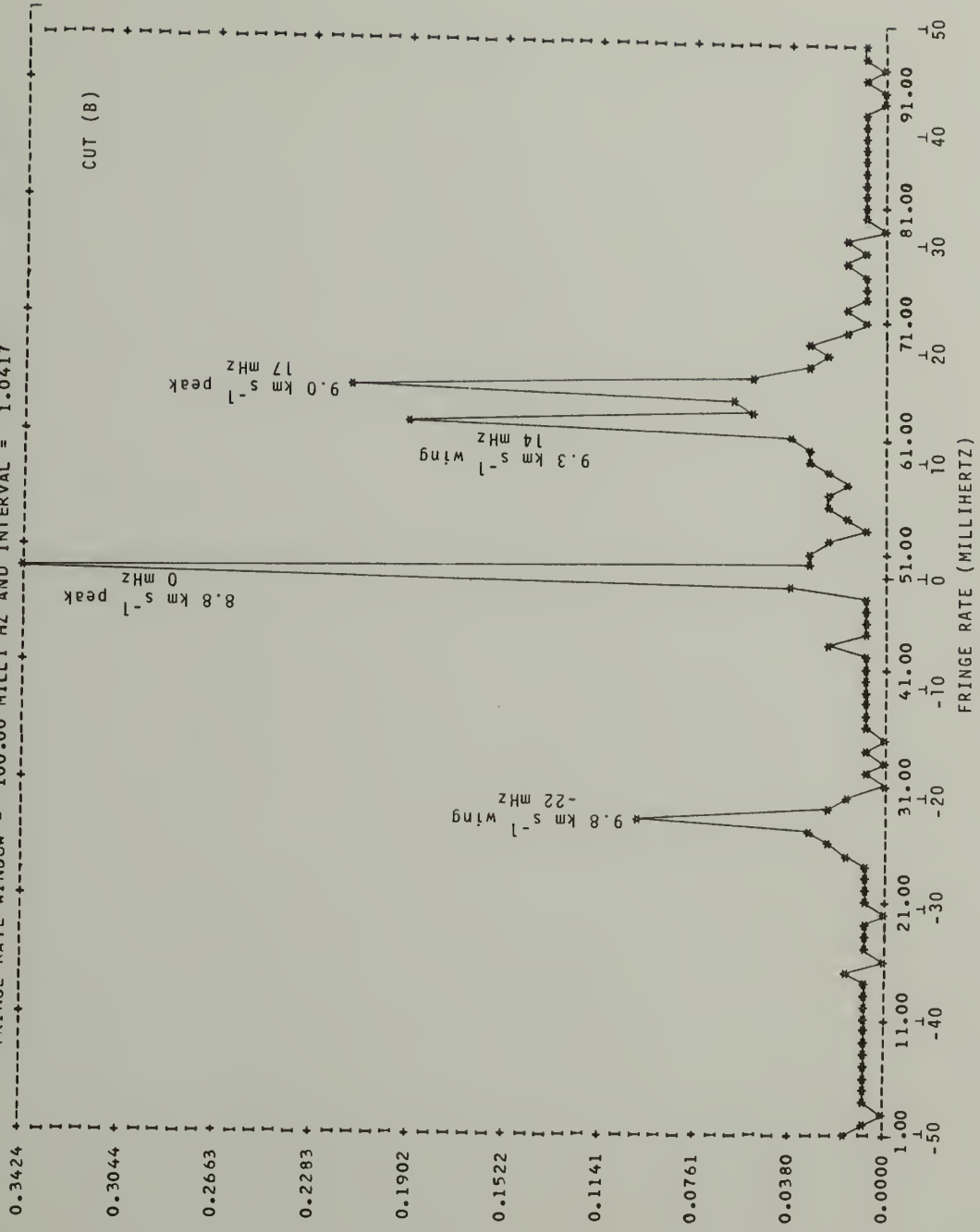


Fig. 11. A sample plot of fringe amplitude as a function of fringe rate and velocity for Orion from 1978 November 2 1125 UT. The amplitudes are relative and run " ", 1, ... 9, A, ... Z, with "Z" being the greatest amplitude. The cuts through the plots are (A) the fringe rate spectrum for the 9.8 km s^{-1} channel (Figure 10a), (B) the fringe rate spectrum for the 8.8 km s^{-1} channel (Figure 10b), (C) the velocity spectrum at the fringe rate of the strongest maser at 9.8 km s^{-1} (Figure 12a) and, (D) the velocity spectrum at the fringe rate of the strongest maser at 8.8 km s^{-1} (Figure 12b). The boxes enclose the strongest feature in each velocity channel.

FRINGE AMPLITUDE VS FRINGE RATE (DOWN PAGE) AND FREQUENCY (ACROSS PAGE)
FRINGE RATE INTERVAL = 1.042 MILLI HZ FREQUENCY INTERVAL = 15.50 KHZ



Fig. 12. Sample velocity spectra of Orion from 1978 November 2 1125 UT at the fringe rate of the peak in the fringe rate spectra for (a) the 9.8 km s^{-1} channel, and (b) the 8.8 km s^{-1} channel. The velocity scale is for the local standard of rest in units of km s^{-1} . A number by a spectral peak is its LSR velocity. The amplitude for the spectrum is in units of the geometric mean of the system temperatures of the two telescopes.



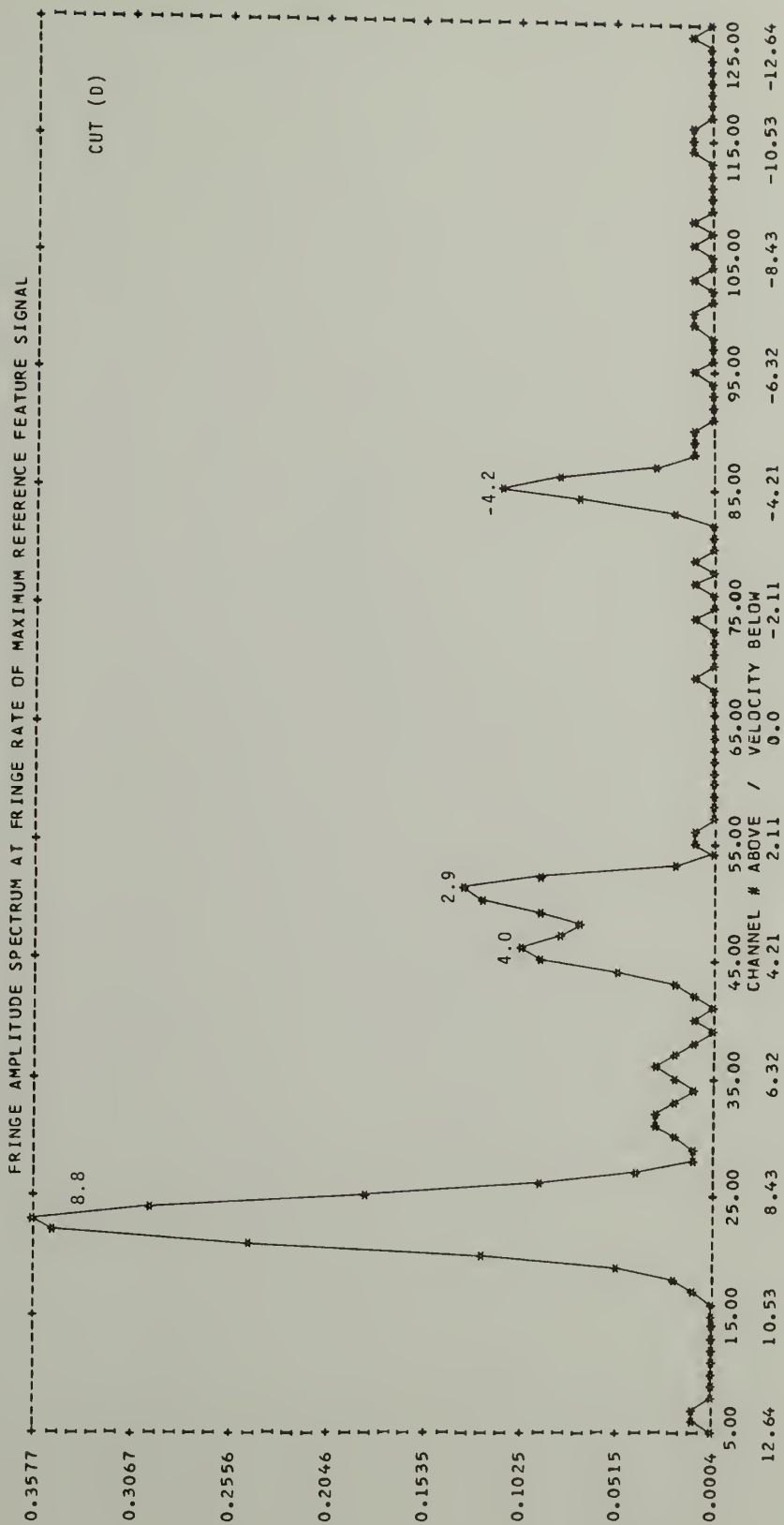
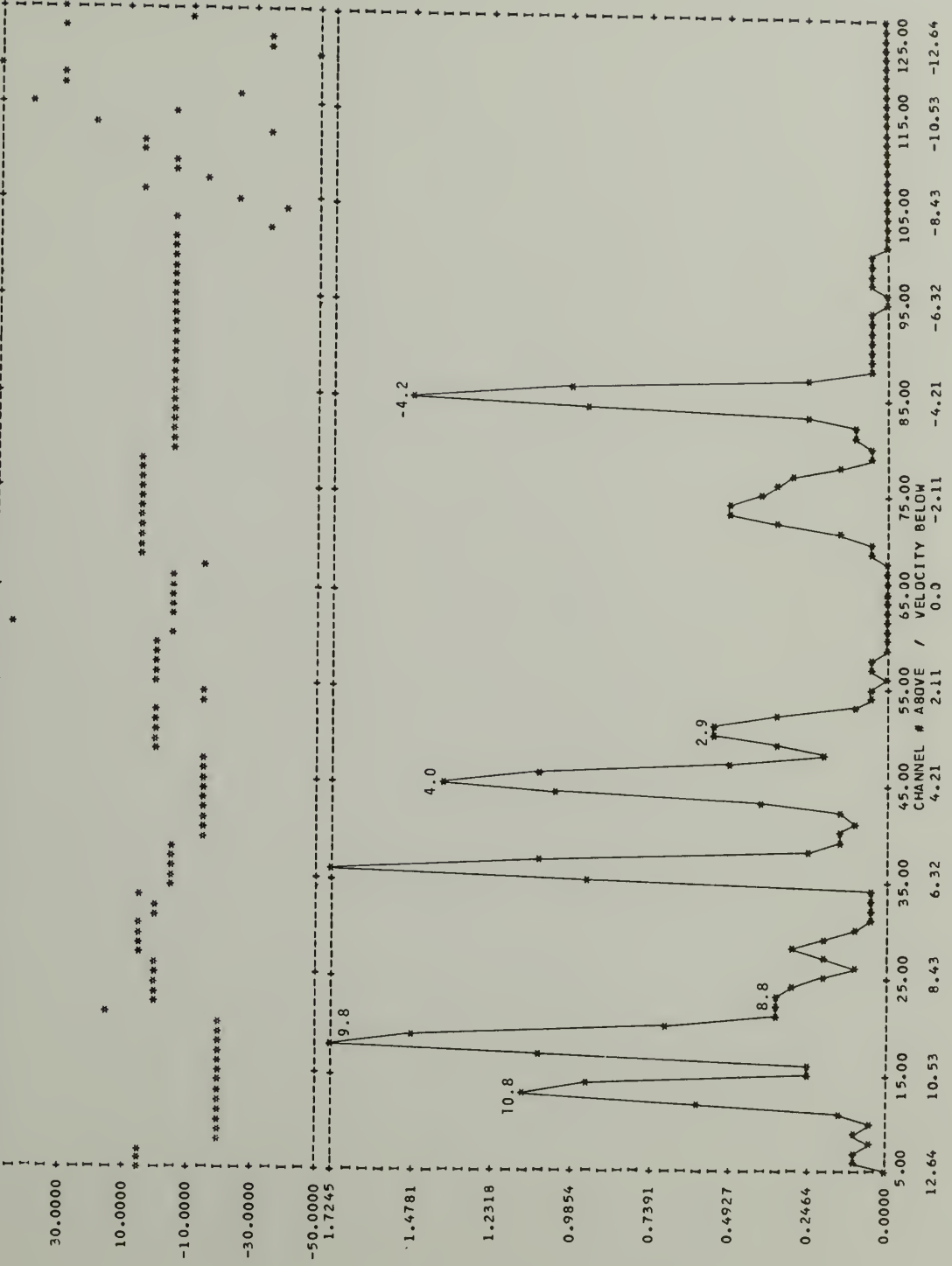


Fig. 13. A sample plot of the peak amplitude and its fringe rate from the fringe rate spectrum for each velocity channel for Orion from 1978 November 2 1125 UT. The velocity scale is for the local standard of rest in units of km s^{-1} . A number by a spectral peak is its LSR velocity. The amplitude of the spectrum is in units of the geometric mean of the system temperatures of the two telescopes. The vertical scale for the fringe rates is in millihertz. The points shown in this spectrum are enclosed in boxes in Figure 11.

PEAK FRINGE AMPLITUDE (PEAKED IN FRINGE FREQ SPECTRUM), AND RESIDUAL FRINGE RATE IN THE WINDOW 100.000 MILLI HZ WIDE
 DATA FROM 11 17 14.5 TO 11 33 04.5 SPANS A TIME PERIOD OF 00 15 50.0



rate and the data can be further averaged. Hopefully, one reaches the point where the phase of the data is due entirely to source structure.

The fundamental limit on the integration time is the size of the area over which the masers are spread. If the masers are far apart, the difference in their fringe rates will be large. If one reduces the fringe rate of one maser to zero, the others will still have non-zero fringe rates. Upon integration, the amplitude of a feature falls off as $\sin(\pi ft) (\pi ft)^{-1}$ where f is the fringe frequency (rate) and t is the integration time. Hence, the integration time should be less than about $(4f)^{-1}$. If necessary, the area on the sky can be divided into subsections which are further averaged and processed separately.

Once averaging has reduced the quantity of data to a more manageable size, the amplitude of each cross power velocity spectrum is calibrated. During the observations, some data were taken with the telescopes off source (or on a continuum source). These observations reveal the bandpass of the individual telescopes. As for a single telescope observation, the spectrum for each individual telescope is

$$\frac{S_v(\text{on}) - S_v(\text{off})}{S_v(\text{off})} T_{\text{sys}}$$

Since the noise at each telescope is uncorrelated, it is not necessary to subtract the off source spectrum from the cross power spectrum.

However, the cross power spectra are divided by the geometric mean of

the bandpasses of the individual telescopes to correct for gain variations across the bandpass.

The cross power and total power spectra can now be corrected for the Doppler shift due to the earth's rotation. In an observation with a single telescope, the local oscillator frequency is updated regularly under computer control. VLBI requires that the observing frequency be known to a small fraction of a Hertz. The best way to achieve this accuracy, and to reduce the opportunity for nonrecoverable errors at record time, is to set the frequency once for a source and remove the Doppler shift in postprocessing.

The final step of the calibration is to normalize the cross power spectra of each telescope pair to the best composite single telescope spectrum. The first phase in this process is to obtain a good spectrum from each individual telescope. Since noise may dominate the spectrum from some telescopes, a template spectrum is made by averaging the good data from the best telescope(s). The total power spectrum from each telescope is then fit to this template by adding a constant factor to the spectrum and multiplying by a scale factor. The cross power spectra from each telescope pair are then divided by the geometric mean of the scaling factors of the two telescopes to normalize the cross power spectra to the template spectrum.

The postprocessing has reduced the data to a total power spectrum for each telescope and a time sequence of appropriately averaged complex cross power spectra for each telescope pair. Further analysis will determine the position and size of each maser.

2.3 Map Making

A cross power spectral value measures one point in the Fourier transform of the brightness distribution of a source at one velocity. This value is the vector sum of the complex responses, i.e., amplitudes and phases, of the interferometer to emission from each point within the telescope beam. The responses add constructively or destructively depending on the u-v position and the separation of the points on the sky. A precise map of a source could be reconstructed from a complete collection of cross power spectra for each point in the u-v plane. The limited u-v coverage (especially for low declination sources such as Orion), unknown variations in the delay (hence phase), and computer limitations (a water vapor map of Orion would have several billion points at each velocity) prevent this. To overcome these problems, a number of assumptions are made. The masers are considered to be point sources to determine their relative positions. This is reasonable because the size of a maser is a few astronomical units, while the area over which they are spread is 20 000 a.u. in diameter. It is also assumed that at any particular velocity there is only one maser. This is not always correct and a processing system for determining the positions of several masers with the same velocity is under development.

With the above limitations and assumptions, phase mapping is the most accurate technique to determine the relative position of a velocity feature. A least squares fit is found to Equation 2.3 for the measured relative phase at a number of u-v points. Since 2π ambiguities

in the phase must be resolved, the technique is limited to features which are so close together and baselines (in wavelengths) which are so short that the relative phase goes through only a few turns in a day. Phase mapping yields the extremely accurate relative positions of the Orion OH masers given in Section 4.1.

The Orion H₂O masers are spread over a larger region on the sky than the OH masers and the baselines between the same telescopes, when measured in wavelengths, are 13 times longer. Since direct phase mapping was impossible because of 2π ambiguities, fringe rate mapping was used. In this technique, a least squares fit is found to the time derivative of Equation 2.3, i.e.,

$$\begin{aligned} \dot{\phi} = \Omega \frac{f}{c} \sqrt{(X^2 + Y^2)} & [\cos (IHA) \cos \delta \Delta\alpha \\ & + \sin (IHA) \sin \delta \Delta\delta] , \end{aligned} \quad 2.6$$

for the fringe rates measured at a number of u-v points. The rotation rate of the earth, $\Omega (7.29 \cdot 10^{-5} \text{ radians s}^{-1})$, is implicit in Equation 2.2 to convert UTC, GASTM, and α from units of time to radians. A great deal of sensitivity is lost in going from phase mapping to fringe (phase) rate mapping. Furthermore, the sensitivity of the fringe rate to offsets in declination contains a factor of $\sin \delta$. For Orion with a declination of -5° , fringe rate mapping is ten times less sensitive to an offset in declination than to an equal offset in right ascension.

In addition to the fundamental problems of fringe rate mapping, there are also technical problems. The processing programs select the

fringe rate of only the strongest feature in the fringe rate spectrum for a particular velocity channel. The program ignores secondary peaks in the fringe rate spectrum due to emission at the same velocity but from another position on the sky. For example, while the fringe rate spectrum for the 9.8 km s^{-1} velocity channel (Figure 10(a) and Figure 11 cut (A)) had only one peak (at -22 mHz), the fringe rate spectrum for the 8.8 km s^{-1} velocity channel (Figure 19(b) and cut (B) on Figure 11) contains four peaks. This implies that emission at 8.8 km s^{-1} comes from at least four distinct positions on the sky. Only the amplitude and fringe rate of the peak at 0 mHz (channel 49) will be used for the fringe rate map of the 8.8 km s^{-1} emission. The peaks at -22 mHz and $+14 \text{ mHz}$ are emission from the wings of the velocity features centered at 9.8 and 9.3 km s^{-1} . Those masers will be mapped by the peak fringe rates at those velocities. However, the peak at 17 mHz represents a feature which does not dominate any velocity channel. With a fringe rate mapping program which selects only the strongest peak in each fringe rate spectrum, this maser will be missed entirely. This selection technique of picking only the strongest peak not only ignores some sources but may select the wrong source because the size of a peak depends on the degree of resolution of the source as well as the intensity of the source. Thus, a large strong source might be the biggest feature in the fringe rate spectrum on a short baseline but be completely resolved on a long baseline. On a long baseline, a weak but small source might dominate the fringe rate spectrum. In this case, a least mean squares fit would fail because

the selected fringe rate at different u - v points would correspond to different positions on the sky.

For an illustration of how fringe rate mapping works, consider a velocity spectrum at one particular fringe rate (Figure 12(a) and cut (C) on Figure 11). The fringe rate for Figure 12(a) is the rate of the peak amplitude for the 9.8 km s^{-1} channel. All the features which appear in that spectrum have the same fringe rate and therefore lie on a line on the sky of constant fringe rate. (An interferometer is sensitive to position offsets in only one direction at any one time.) As the earth rotates, the lines of constant fringe rate change angle on the sky; hence, features at different positions on the sky will not always have the same fringe rate. The dependence of the fringe rate on u and v makes fringe rate mapping possible (Equation 2.6). The two velocity features shown in Figure 12(a) had nearly equal fringe rates at all times during the day, proving that the masers were very close together. The velocity spectrum at the fringe rate of the peak in the 8.8 km s^{-1} fringe rate spectrum (cut D in Figure 11) is shown in Figure 12(b). That figure indicates that the masers at -4.2 , $+2.9$, 4.0 , and 8.8 km s^{-1} all lie close to a line on the sky of equal fringe rate. At other times of the day these velocity features had different fringe rates proving that they had different positions on the sky.

Dispite all the problems, the relative positions of the strong water vapor masers in Orion are determined by fringe rate mapping to an accuracy of $0''.01$ in right ascension and $0''.1$ in declination. At

the distance of the Orion Nebula, $0''.01$ corresponds to 5 a.u., the approximate size of a water vapor maser.

2.4 Maser Size

Once the position of a maser, which was assumed to be a point source, has been found by phase or fringe rate mapping, one would like to determine its actual spatial structure. If the maser has structure, the interferometer response to each point on the source will be slightly out of phase. As u or v increases, the phase difference increases. The measured amplitude, which is the vector sum of the interferometer responses to each point on the source, will vary (usually decrease) as the phase difference increases. With complete u - v coverage, the source brightness distribution could be precisely reconstructed. With reasonable u - v coverage, the most probable source structure could be reconstructed. With typical VLBI u - v coverage, the source is modeled, and the model parameters are adjusted to fit the data.

The most common models are a few closely spaced point sources, a circular source of constant intensity, or a circular source with a Gaussian intensity distribution. A circular Gaussian source is characterized by its position, total intensity, and full width at half maximum (FWHM). The FWHM and the visibility (V), i.e., the ratio of the cross correlated power to the total power, of a source are related by

$$v = \exp \left\{ -3.56 \left[\frac{\text{FWHM}}{\text{fringe spacing}} \right]^2 \right\} .$$

Both the total power and the cross power are difficult to measure accurately. The total power of a velocity feature is derived from the single telescope spectrum taken during the VLBI experiment. If an observer has gone to the extra effort of a VLBI experiment over a single telescope experiment, he wants to spend most of his time recording signals which can be correlated. Therefore, the off source time is usually much shorter than the on source time. Furthermore, the on and off scans are typically half an hour apart. Spectral baseline determination is extremely difficult in the water vapor spectra of Orion A and other strong sources because the emission spans the 2 MHz VLBI bandpass. A constant baseline offset is often removed using the lowest one (1) channel. With a switched frequency VLBI spectrum, a constant baseline may be fit to one side of the spectrum. However, fitting a slope is difficult and is usually not done.

The cross correlated power of a velocity feature is assumed to be the amplitude of the strongest peak in the fringe rate spectrum for that velocity. This value is usually a lower limit to the amplitude. Each integration reduces the amplitude by $\sin(\pi ft) (\pi ft)^{-1}$ where f is the fringe rate and t is the integration time (see Section 2.2). This effect is usually negligible except for the final integration before the calculation of the fringe rate spectrum. The amplitude reduction in that final integration may be as large as 36% ($ft = 0.5$),

but, since the fringe rate is determined for the feature, the amplitude may be corrected. Oscillator phase noise also reduces the amplitude until the data is phase referenced. The effect of oscillator noise can be calculated and corrected if the data contains observations of an unresolved source. Any effect which spreads the power from a source over more than one fringe rate interval will reduce the peak in the fringe rate spectrum, and hence, the determined cross power amplitude. Fourier transforming data which spans too long a period of time will broaden a peak in the fringe rate spectrum because the source will have one fringe rate at the beginning of the transform period and another rate at the end.

The cross correlated power determined from the fringe rate spectrum for a certain velocity measures the power from only one position on the sky. To properly calculate the visibility one must know the total flux from just that position. Unfortunately, a single telescope spectrum measures all the power at a particular velocity within the telescope beam. For example, in the 1978 November 2 spectrum (Figure 34), the 6.1 km s^{-1} feature has a visibility of 0.79 ± 0.01 for fringe spacings ranging from 37 to 211 milliarcseconds. The remaining 21% of the flux density, i.e., 1000 Jy, must come from diffuse sources and/or point sources at other positions in the telescope beam. In the velocity range from 3 to 18 km s^{-1} there could be flux density of several hundred Janskys from weak diffuse sources. If 400 Jy were subtracted from the autocorrelation spectra in the range from 12 to 18 km s^{-1} , the visibility of the features in that velocity interval

would range from 0.5 to 1.0 instead of the measured 0.1 to 0.4.

Other problems in determining the visibility arise because some telescopes have circularly polarized feeds and others have linearly polarized feeds. For an unpolarized source, the effect of unmatched feeds is removed by multiplying the cross power spectra by $\sqrt{2}$. In a source with polarized emission like Orion, the correction factor depends on the degree of polarization and the angle of the feed. Since linearly polarized feeds usually have a fixed angle to the horizon, the plane of polarization on the sky to which the feed is sensitive changes as the telescope tracks the source. Consequently, the correction factor varies with feature, telescope, and time. The template fitting process described in Section 2.2 depends on the spectra from each telescope being identical except for a constant baseline offset and scale factor. This, of course, is not true for polarized features observed with feeds at different position angles. Template fitting will replace random noise with systematic effects. The net effect may still be beneficial, but the fit must be done with caution. Particular attention was paid to the polarization problem in Orion in the 1978 November 2 water vapor data. The effect on the measured visibility was less than 10%.

Considering all sources of error, one can usually estimate the size of a feature whose FWHM is greater than 0.2 of the smallest fringe spacing but less than 0.7 of the largest fringe spacing. Outside these size limits the calculated diameter is extremely sensitive to small changes, i.e., noise, in the visibility and only upper or lower limits to the FWHM can be determined with much certainty.

C H A P T E R I I I
THE WATER VAPOR MASERS

3.1 Early Water Vapor Observations of Orion

Cosmic water vapor lines were first detected by Cheung et al. (1969) in 1968 towards Orion A, Sgr B2 and W49. The high intensity and unusual narrowness of the lines suggested that the population of water vapor molecules was not in thermodynamic equilibrium, and that maser action was producing the intense radiation. The lines which Cheung et al. (1969) detected were from a rotational transition at 22 235 MHz. The water molecular is an asymmetric rotator, i.e., the moments of inertia about all three axes are unequal. For this reason, K , the projection of the angular momentum, J , onto any axis is not a good quantum number. However, the molecule may be approximated as a combination of a prolate and an oblate symmetric top. A state with angular momentum J is labeled as

$${}^J_{K_{\text{prolate}}} K_{\text{oblate}}$$

where the K 's are the projection of J onto these prolate and oblate axes. The water vapor lines at 22 GHz come from the $6_{16} - 5_{23}$ rotational transition. It is coincidental that these states lie so close together. Most of the rotational transitions are in the infrared. The energy of the 6_{16} and 5_{23} levels corresponds to a temperature of approximately 650°K. In the ground electronic state, the

first and second electron shells are full. The electrons are paired and have a net spin and angular momentum of zero. The sum of the spins of the hydrogen nuclei, which must be 1, interacts vectorially with J to produce three hyperfine states in each rotational level. The allowed hyperfine transitions of the $6_{16} - 5_{23}$ rotational transition and the resulting spectrum are shown in Figure 14.

Many observations of the Orion nebula region in the water vapor transition at 22 GHz followed the initial detection (Knowles et al. 1969a,b, Meeks et al. 1969, Buhl et al. 1969). Sullivan (1971 and 1973) monitored several H_2O sources (e.g., W49, Orion A, VY CMa, W3, ON-1, W75(S)) from 1969 January to 1970 June for time variations in intensity, velocity, line width, and polarization. His observations in 1969 and 1970 showed that Orion had four main spectral groups at -6, +2, 9 and 15 km s^{-1} . The -6 and 15 km s^{-1} groups varied only slightly in amplitude and showed little or no polarization. (In Section 4.3 I will associate these features with an evolved star.) The other groups contained features which varied by more than a factor of two. (The individual features of Sullivan's velocity groups at 2 and 9 km s^{-1} are now known to be spatially separate.) The 11 km s^{-1} feature was constant in both intensity and velocity. The more intense features were usually the most linearly polarized, although the features at 6.5 and 11 km s^{-1} showed no linear polarization at the 10% level. The position angle of the polarization varied with time, and the position angle and percent of polarization were not constant across a velocity feature. No circular polarization greater than 10% was seen in Orion.

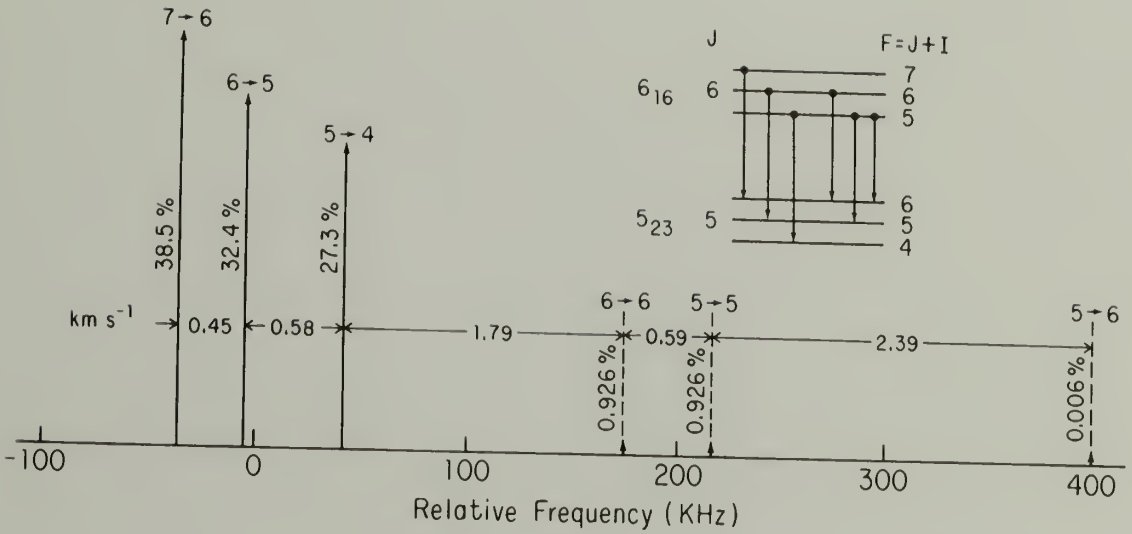
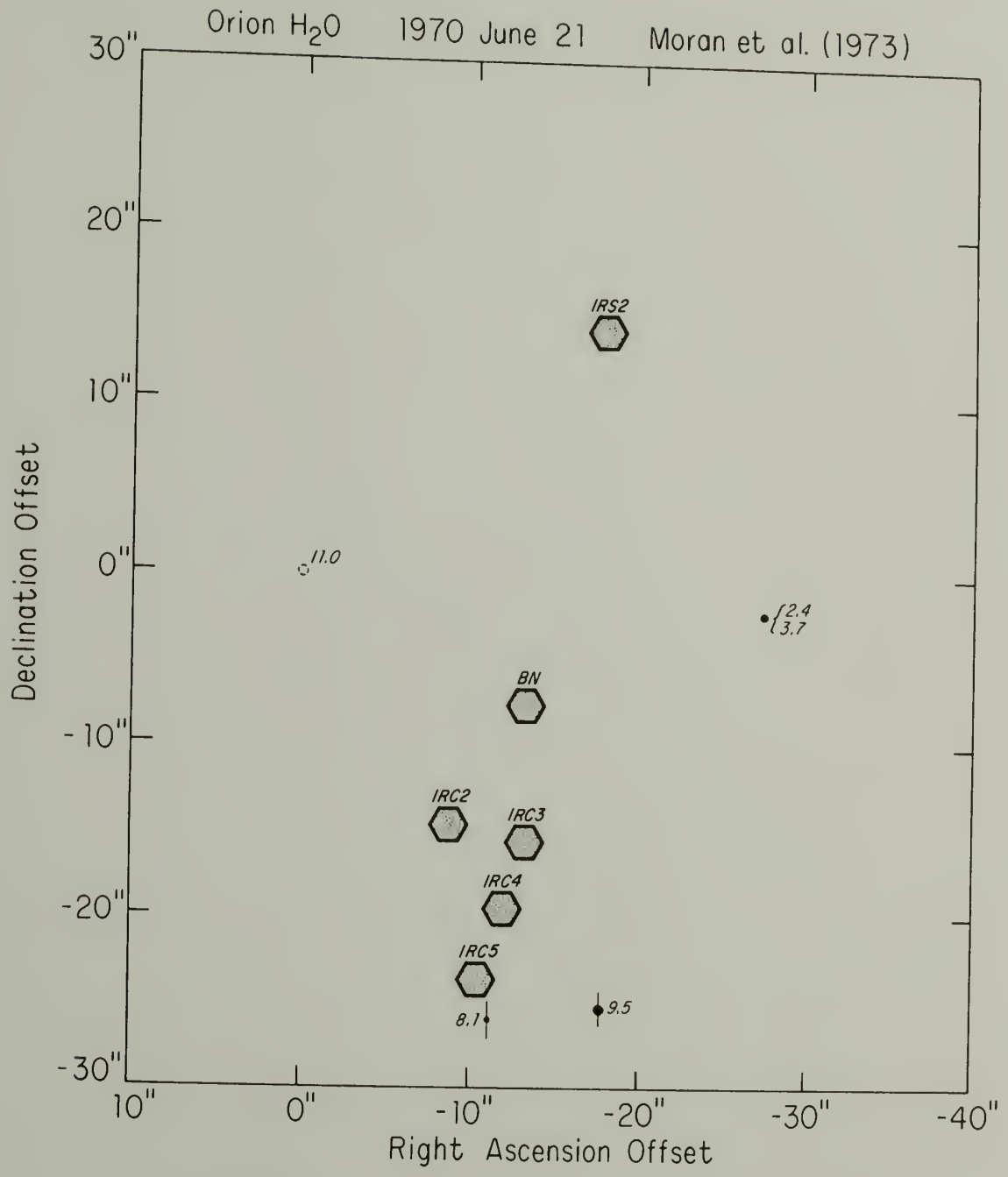


Fig. 14. The hyperfine lines of the $6_{16} \rightarrow 5_{23}$ rotational transition of H_2O . The zero of the horizontal axis is 22 235 079 846 Hz, which is the average of the frequencies of the six hyperfine components weighted according to the LTE intensities. The separation of the lines is given in km s^{-1} . The LTE relative intensity is given beside each spectral line. The frequencies are from Kukulich (1969) and the LTE intensities are from Townes and Schawlow (1955 p. 501).

The number of water vapor observations of Orion diminished after 1970. Polarization studies were done by Bologna et al. (1975) and Knowles and Batchelor (1978). Little, White, and Riley (1977) monitored Orion from 1974 August to 1976 January. Their results supported those of Sullivan. In an interesting analysis of time variations, they produced a histogram for W49 and Orion of the number of features which varied by a certain percent during 40 to 50 day periods. Orion had no features which varied by more than a factor of two while 25% of the features sampled in W49 varied by more than a factor of two in that time period.

As early as 1969, Meeks et al. (1969) attempted to map the relative positions of the H_2O masers in Orion to within a few arc-seconds. Burke et al. (1970) and Johnston et al. (1971) showed that the individual masers were extremely small (1 - 10 a.u.). Moran et al. (1973), using VLBI, determined the sizes and relative positions of several features (Figures 15, 16, 17). The general characteristics of the VLBI maps have been confirmed by single telescope maps made from a five point offset pattern (Moran et al. 1977 Figure 18, and Genzel and Downes 1977 Figure 19). The relative positions determined with VLBI are hundreds of times more accurate than single telescope maps because phase information is used. In 1977 Forster et al. (1978) determined the absolute positions of five water vapor masers in Orion. Those positions are shown on the map (Figure 8) relating the H_2O masers to the OH masers, the SiO masers, the CH_3OH masers, the infrared point sources, and the H_2 emission.

Fig. 15. A Mark I VLBI fringe rate map (Moran *et al.* 1973). The number identifying a maser is its LSR velocity (km s^{-1}). The amplitude of a feature is proportional to the area of the circle at the maser position. The bars are the formal errors from the least squares fit of the position offset to the relative fringe rates. A feature without error bars had offset uncertainties smaller than the circle. The origin of the axis is the position of the 11 km s^{-1} feature at $\alpha(1950) = 5^{\text{h}} 32^{\text{m}} 47^{\text{s}}.58 \pm 0^{\text{s}}.02$ and $\delta(1950) = -5^{\circ} 24' 9''.3 \pm 0''.5$ (Forster *et al.* 1978). The open circle indicates the estimated location of the 11 km s^{-1} feature from the 1971 March map. The map has the same scale as Figure 8. The IRC sources are shown to facilitate the comparison of maps from different epochs.



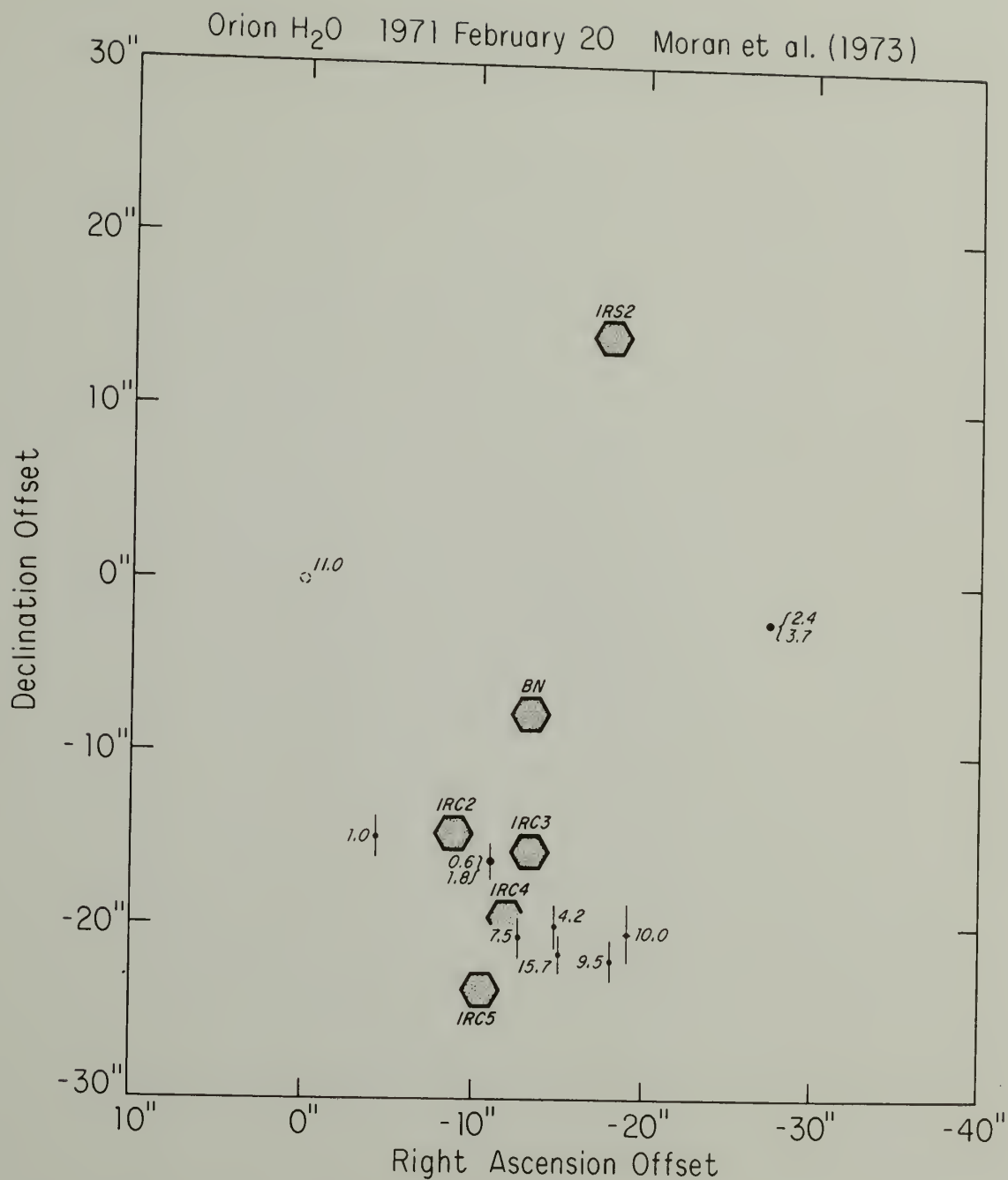


Fig. 16. A Mark I VLBI map from Moran *et al.* (1973). A more detailed description of the map is given in the caption for Figure 15.

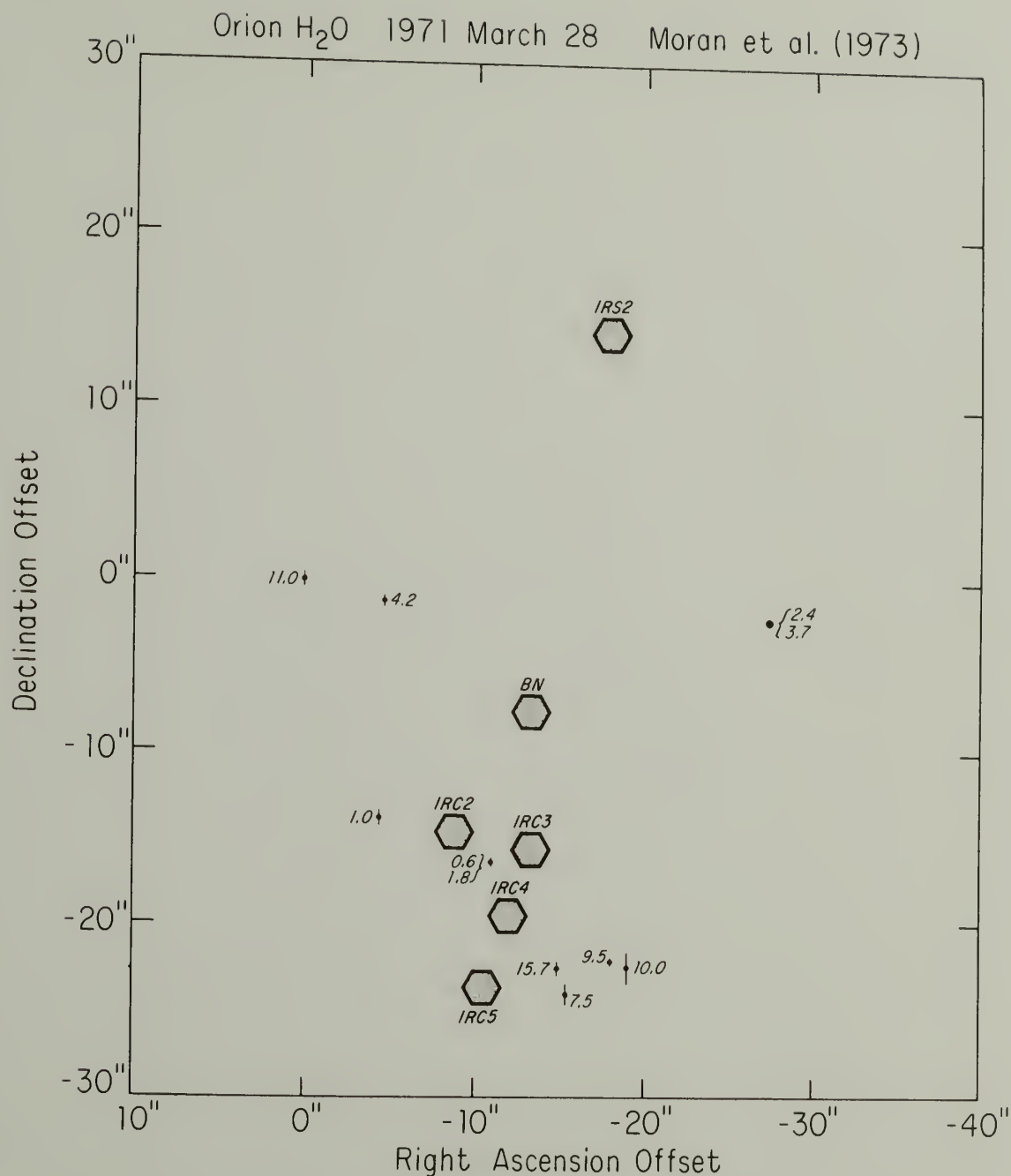


Fig. 17. A Mark I VLBI map from Moran *et al.* (1973). Note that the 11 km s^{-1} feature was actually detected at this epoch. A more detailed description of the map is given in the caption for Figure 15.

Fig. 18. A single telescope water vapor map for 1976 June from the Haystack observatory (Moran et al. 1977). The number identifying a maser is its LSR velocity (km s^{-1}). The amplitude of a feature is proportional to the area of the circle at the maser position. The error bars are the uncertainties in the positional offsets from the 17.2 km s^{-1} feature. A feature without error bars had offset uncertainties smaller than the circle. The error bars without \cdot 's indicate the position of a maser with a peak flux density of less than 700 Jy . The origin of the axis is the position of the 11 km s^{-1} feature at $\alpha(1950) = 5^{\text{h}} 32^{\text{m}} 47^{\text{s}}58 \pm 0^{\text{s}}02$ and $\delta(1950) = -5^{\circ} 24' 9''3 \pm 0''5$ (Forster et al. 1978). The map has the same scale as Figure 8. The IRC sources are shown to facilitate the comparison of maps from different epochs. Problems in telescope pointing resulted in the displacement of the position offsets compared to the VLBI maps.

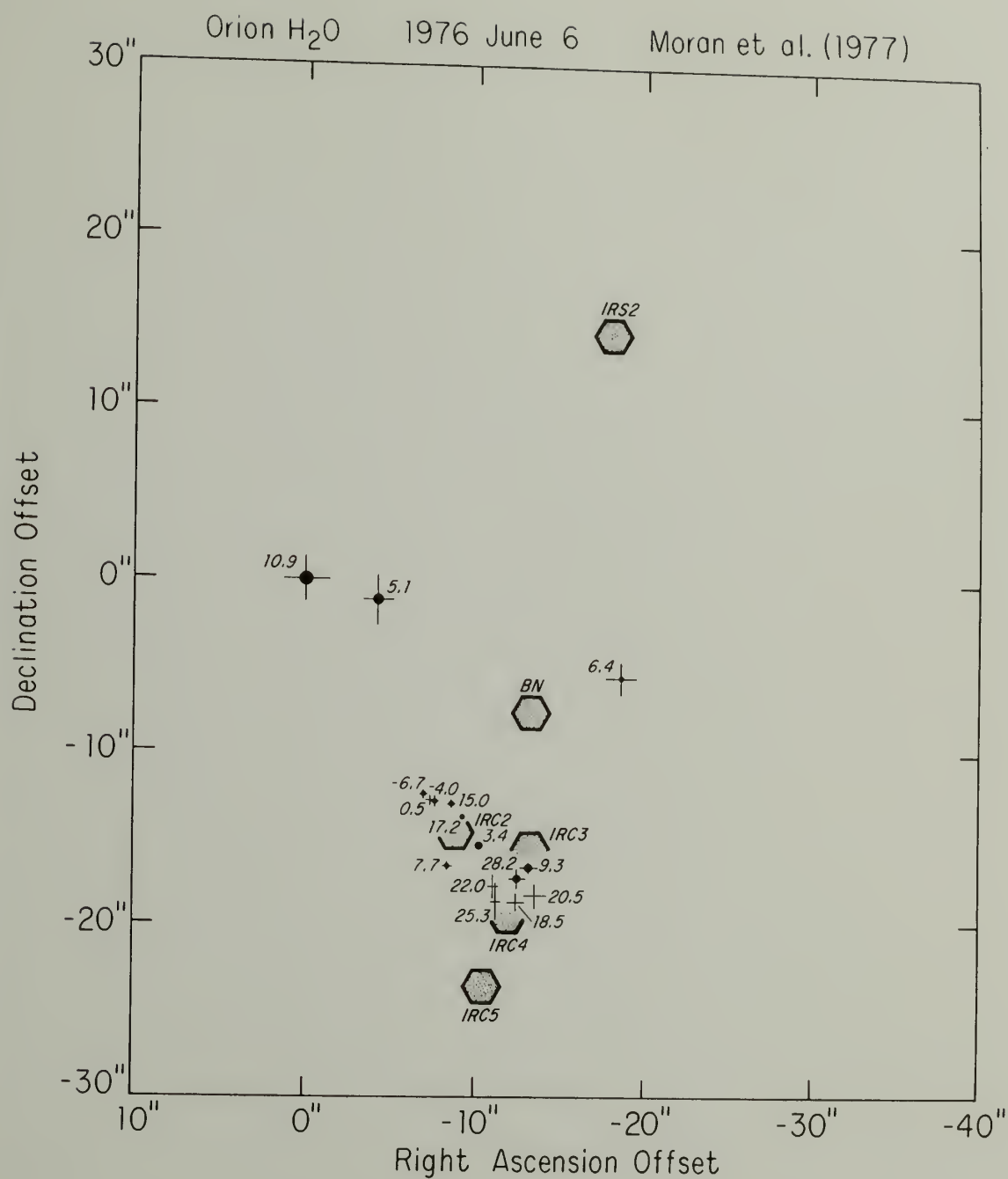
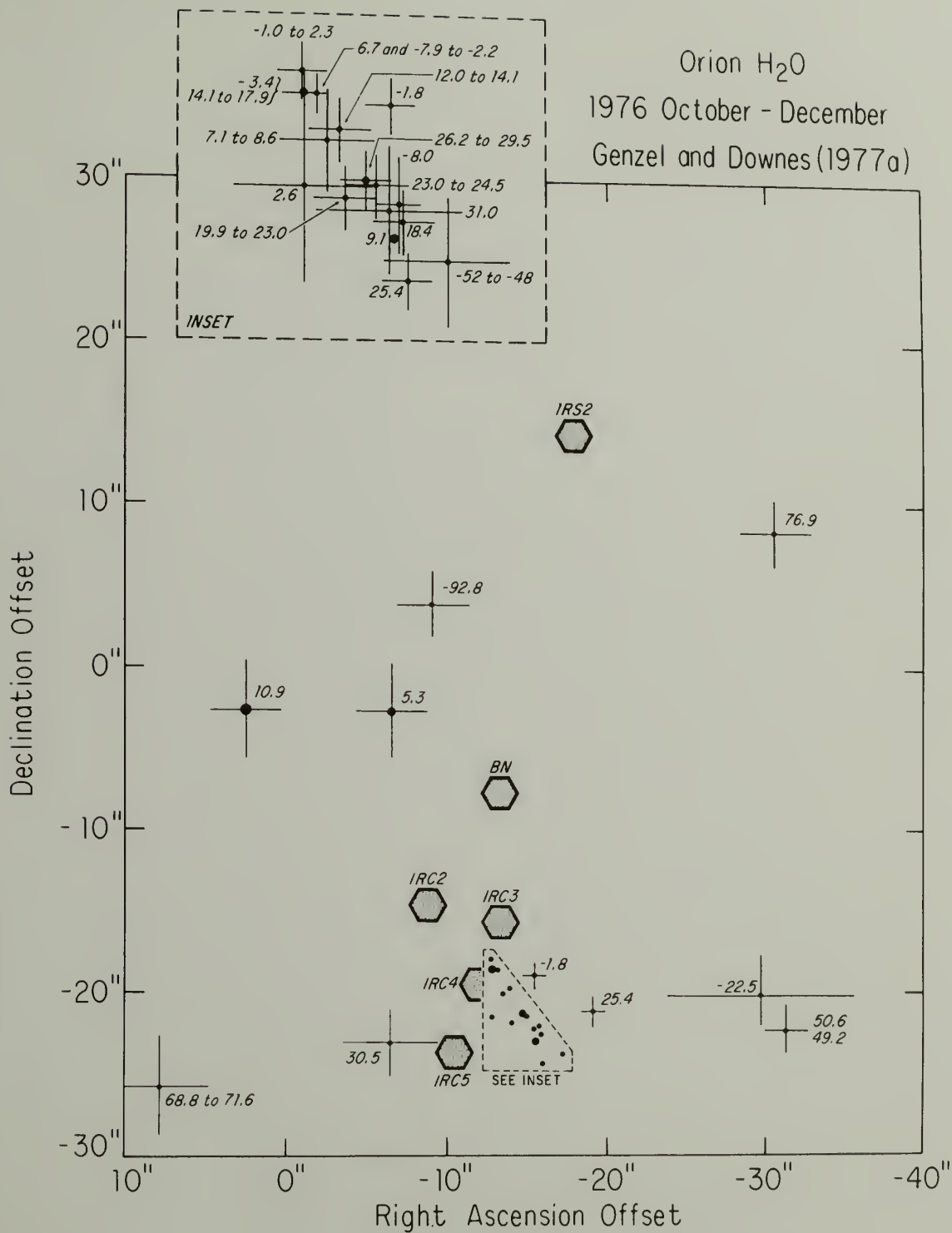


Fig. 19. A single telescope water vapor map with high velocity features for 1976 October-December from the Bonn 100 m telescope (Genzel and Downes 1977a). The number identifying a maser is its LSR velocity (km s^{-1}). The amplitude of a feature is proportional to the area of the circle at the maser position. The error bars are the uncertainties in the relative positions of the masers. The uncertainty in the absolute positions of the masers is $2''$ in both right ascension and declination. The maser positions are relative to the 10.9 km s^{-1} feature. However, the position found by Genzel and Downes (1977a) for the 11 km s^{-1} feature, i.e., $\alpha(1950) = 5^{\text{h}} 32^{\text{m}} 47^{\text{s}}.75 \pm 0^{\text{s}}.15$ and $\delta(1950) = -5^{\circ} 24' 12'' \pm 3''$, is offset from the origin of the map as determined by Forster *et al.* (1978) by $\Delta\alpha = +2''.6$, $\Delta\delta = -2''.7$. This positional error allows for a large shift of the masers relative to the IRC sources. The scale of the inset is twice that of the larger map. The spot sizes, which indicate the flux density of the masers, have the same scale in the inset and the larger region.



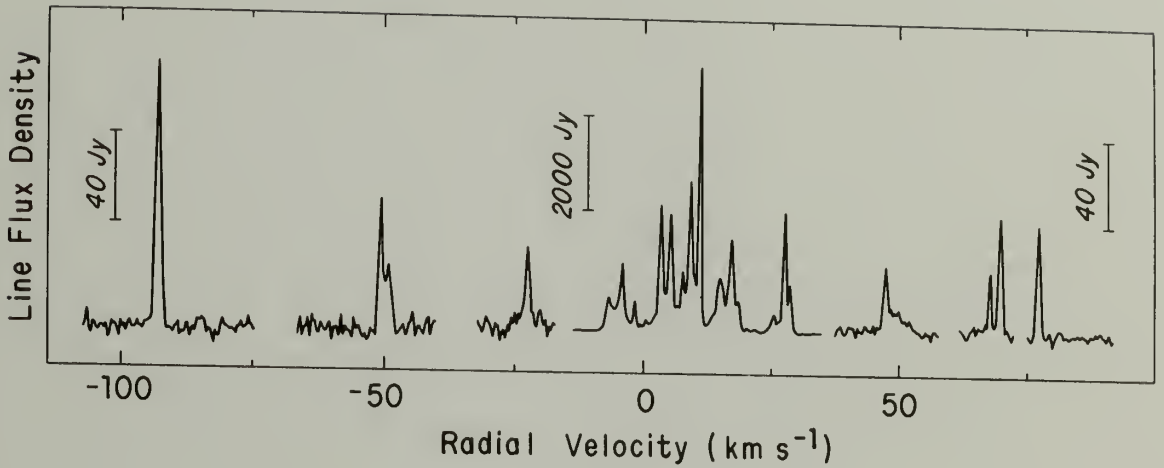


Fig. 20. A composite spectrum of the Orion H_2O lines observed on Dec. 7, 1976 near the positions of maximum line intensity given in Figure 19. The resolution is 0.43 km s^{-1} . Note the change in the intensity scale for the range -15 to $+35 \text{ km s}^{-1}$, which was observed in the position of Source A. (Reproduced with permission of *Astronomy and Astrophysics* and the authors from Genzel, R., and Downes, D. 1977, *Astron. Astrophys.*, 61, 117, copyright 1977.)

Genzel and Downes (1977a) reported 13 high velocity features in Orion A from 10 positions as far as 30" from the KL nebula (Figure 19). The spectrum is shown in Figure 20. The high velocity features are scattered all over the map and cannot be spatially associated with the IR sources or the low velocity features. The high velocity features have only one or two lines. There are no high velocity OH or SiO masers.

3.2 New Maps of the Water Vapor Masers in Orion

In the spring of 1974, I proposed a VLBI monitoring program to measure the time variations in the water vapor masers associated with Orion A. The goal of that project was to determine the permanent characteristics of the masers, the variable characteristics of the masers, and the manner in which they vary. The long-lasting characteristics are indicative of the underlying energy source, while the variations are indicative of changes in the gas flow, the maser pump, and the degree of saturation. Extremely accurate positions were essential to this project to (1) distinguish intrinsic changes in an individual maser from apparent changes caused by variations in several frequency blended but spatially separated masers, and (2) determine if the masers had proper motion. With positional accuracy of 10 milliarcseconds (5 a.u.), one could detect transverse velocities of 25 km s^{-1} in a year. Hence, if the transverse velocities were comparable to the radial velocity dispersion of the masers, I should have seen the masers move.

To measure the time variations in the water vapor masers, I observed Orion A in 1975 March, 1976 September, 1978 July and 1978 November. Using the new, high spectral resolution, 96 channel VLBI processor, I also reanalyzed data recorded in 1972 and 1974. The constant parameters of the telescopes are given in Table 2, the parameters which varied from experiment to experiment, in Table 3, and the range of velocities and fringe spacings, in Table 4. The resulting maps of the region at these six epochs are shown in Figures 21 through 26. A composite map of all six epochs is shown in Figure 27 with an enlargement of the southwest section in Figure 28. The total power and cross power spectra associated with each map are shown in Figures 29 through 34. Tables 5 through 10 summarize the data for each epoch.

The maps and the tables give the positions of the masers relative to the 11 km s^{-1} feature which is the most constant and least blended of the strong features. Its absolute position (Forster *et al.* 1978) is shown in Figure 8. Any motion in the 11 km s^{-1} emission would appear as a shift in all the other source positions. Fortunately, no shift was seen. The 11 km s^{-1} feature is present in all maps except the 1970 June and 1971 February maps of Moran *et al.* (1973).

For the detailed discussion of the time variations in the water vapor masers, I will divide the entire maser region, which is 20 000 a.u. (500 a.u. = 1") in diameter, into "clusters". A cluster is a region less than 1000 a.u. (2") in diameter containing one, two, or occasionally more velocity features. I identify 13 clusters in

TABLE 2
Constant Telescope Parameters of the H₂O VLBI Observations

Observatory	Abbreviation	Diameter (feet)	22 GHz Peak Efficiency %	22 GHz Sensitivity (Jy °K ⁻¹)
Five College Radio Astronomy Observatory New Salem, Massachusetts	FCRAO	45	50	37
National Radio Astronomy Observatory Green Bank, West Virginia	NRAO	140	25	7.7
Haystack Observatory Westford, Massachusetts	Haystack	120	20	13
Naval Research Laboratory Maryland Point, Maryland	NRL	85	40	13
Owens Valley Radio Observatory Big Pine, California	OVRO	130	25	9
Algonquin Radio Observatory Lake Traverse, Ontario	ARO	150 (120)	11 (17)	15

TABLE 3

Varying Telescope Parameters of the H₂O VLBI Observations

Telescope	T _{sys} (°K)	Time Standard	Receiver	Polarization
December 1972				
NRAO	2000	Hydrogen Maser	Mixer	Linear East-West
Haystack	150	Hydrogen Maser	Maser	Linear Horizontal
NRL	600	Hydrogen Maser	NRAO Paramp	Linear East-West
January 1974				
NRAO	600	Hydrogen Maser	Paramp	Linear East-West
Haystack	150	Hydrogen Maser	Maser	Left Circular
March 1975				
NRAO	700	Hydrogen Maser	Paramp	Linear East-West
Haystack	200	Hydrogen Maser	Maser	Left Circular
NRL	2000	Hydrogen Maser	Mixer	Linear East-West
ARO	500	Hydrogen Maser	Paramp	Left Circular
OVRO	700	Hydrogen Maser	Paramp	Linear
September 1976				
NRAO	600	Hydrogen Maser	Cooled Mixer	Linear East-West
Haystack	150	Hydrogen Maser	Maser	Left Circular
NRL	1100	Hydrogen Maser and Rubidium	Degenerate Paramp	Linear East-West
July 1978				
FCRAO	2000	Hydrogen Maser	Mixer	Linear Horizontal
Haystack	200	Hydrogen Maser	Maser	Left Circular
November 1978				
FCRAO	2000	Hydrogen Maser	Mixer	Linear Horizontal
Haystack	200	Hydrogen Maser	Maser	Left Circular

TABLE 4
 H_2O VLBI Observing Sessions

Experiment	Velocity Range (km s^{-1})	Fringe Spacing	
		Minimum (milliarcseconds)	Maximum
December 1972	-6 to +20	3.2	22
January 1974	-5 to +21	3.3	4
March 1975	-5 to +21	0.7	38
September 1976	-16 to +33	3.6	16
July 1978	-5 to +21	37	37
November 1978	-12 to +34	3.9	211

TABLE 5
Orion H₂O Features 1972 December 20

Velocity (km s ⁻¹)	Region (name)	Total Power (Jy)	Cross Power (Jy) (0.0009) [†]	Visibility	Velocity Range* (km s ⁻¹)	ΔX (" ± ")	ΔY (" ± ")
-5.0		459	107	0.2			
-1.5	A-2	449	210	0.5	-2.1 to - 1.3	-15.00 ± 0.03	-17.2 ± 0.3
0.0	AL5	209	151	0.7		-14.91	-18.1
1.3	Field	2735	1139	0.4	-0.8	- 4.25	-13.3
2.7	Field	837	131	0.2	2.4	- 5.90	-10.8
4.0	NE 4	5067	552	0.1	3.2	- 4.61	- 0.8
5.3	NE 4	1277	549	0.4	5.8	- 4.57	+ 0.1
6.9	A6	1548	330	0.2	6.6	-15.47	-22.7
7.7	A6	7874	2316	0.3	8.3	-15.48	-22.1
9.4	B8	5720	1305	0.2	8.6	-18.04	-20.7
11.0	NE11	14100	6023	0.4	10.5	-0-	-0-
14.1		450	131	0.3	11.7	-0-	
15.0	AL5	1704	182	0.1	14.7	-14.77	-18.5
15.6	AL5	2167	419	0.2	15.9	-14.78	-18.4
17.0		2406	116	0.05			
17.7	B18	2324	691	0.3	17.3	-19.55	-20.7
18.7	Field	335	170	0.5	18.4	- 4.84	-21.5
					19.0	0.5	0.5

[†] Fringe spacing at which cross power was measured.

* The emission in this velocity range was strong enough in some scans to set the peak fringe rate for that channel to the fringe rate of the listed feature.

TABLE 6

Orion H₂O Features 1974 January 31

Velocity (km s ⁻¹)	Region (name)	Total Power (Jy)	Cross Power (Jy) (0.0004) [†]	Visibility	Velocity Range* (km s ⁻¹)	ΔX (" ± ")	ΔY (" ± ")
-3.2		296	11	0.0			
-2.1	A-2	177	85	0.5	-2.7 to -0.1	-15.02 ± 0.01	-17.46 ± 0.05
1.3	Field	787	75	0.1	1.0	- 4.2	-13.6
1.6	Field	2038	84	0.0	2.1	"	"
2.9	A3	2841	318	0.1	2.4	-12.21	-18.95
3.5	NE4	5356	571	0.1	3.0	- 4.60	- 0.88
4.4	NE4	3280	375	0.1	3.2	- 4.60	- 0.87
6.0	A6	1856	149	0.1	5.8	-15.54	-22.31
7.2	A6	5967	1390	0.2	8.0	-15.52	-22.43
7.7	A6	11952	684	0.1	"	-14.6	-22.9
9.7	B8	8057	1589	0.4	3.2	- 4.60	- 0.87
11.1	NE11	17283	990	0.1	8.3	-18.04	-20.87
14.5	Field	869	49	0.1	10.8	-0-	-0-
15.3	A15	1772	78	0.0	14.2	-12.74	-22.11
17.2	B18	1831	97	0.1	15.0	-14.77	-19.15
18.1	B18	481	73	0.2	16.7	-19.60	-22.06
18.7	A18	311	27	0.1	18.4	-19.65	-22.04
					18.7	-11.31	-22.34
					19.0	0.01	0.03

[†]Fringe spacing at which cross power was measured.

*The emission in this velocity range was strong enough in some scans to set the peak fringe rate for that channel to the fringe rate of the listed feature.

TABLE 7

Orion H₂O Features 1975 March 8-13

Velocity (km s ⁻¹)	Region (name)	Total Power (Jy)	Cross Power (Jy) (0".005) [†]	Visibility	Velocity Range* (km s ⁻¹)	ΔX (" \pm ")	ΔY (" \pm ")
-2.2	A-2	115	87	0.9	-2.7 to	-15.05 \pm 0.03	-17.4 \pm 0.3
-1.1	A-2	236	154	0.7	-0.4	-15.03	-17.4
+0.6	Field	331	130	0.4	-0.2	+26.44	-18.9
2.0		502	75	0.1			0.1
2.9	A3	1332	161	0.1	2.7	-12.24	-19.0
4.1	NE4	5404	748	0.2	3.5	- 4.63	- 0.6
5.8	A6	300	90	0.3	5.5	-15.08	-21.8
6.5	A6	865	163	0.2	5.5	-15.10	-22.1
7.3	AI5	5014	1151	0.2	6.9	-14.63	-19.2
8.2	B8	1273	159	0.1	8.0	-18.09	-20.4
9.3	B9	4374	347	0.1	8.8	-19.04	-22.6
11.1	NE11	7594	472	0.1	10.2	-0-	-0-
14.6	Field	690	28	0.0	14.5	-12.82	23.0
15.5	AI5	1492	181	0.1	14.5	-14.77	-18.9
17.4	B18	1951	195	0.1	16.7	-19.57	-22.0
19.5	B18	∞0	∞0		19.2	19.74	-22.3
20.9	B18	459	303	0.7	20.1	-20.07	-21.6

[†] Fringe spacing at which cross power was measured.

* The emission in this velocity range was strong enough in some scans to set the peak fringe rate for that channel to the fringe rate of the listed features.

TABLE 8

Orion H₂O Features 1976 September 16-18

Velocity (km s ⁻¹)	Region (name)	Total Power (Jy)	Cross Power (Jy) (0.016) [†]	Visibility	Velocity Range* (km s ⁻¹)	ΔX (" ± ")	ΔY (" ± ")
-7.6	Field	94	72	0.8	-8.0 to - 6.8	-19.36 ± 0.05	-19.4 ± 0.2
-6.8		1231	216	0.2			
-4.2	A-2	2214	257	0.1	- 1.0	-15.07	-17.7 0.2
-1.7		404	209	0.5			
-1.4	Field	458	172	0.4	-1.2	- 5.96	-10.4 0.2
+0.4		601	340	0.6	-0.8	- 8.37	-13.3 0.2
2.1	A15	538	151	0.3	+1.6	14.92	-19.5 0.2
3.3	A3	4475	1511	0.3	2.7	-12.26	-19.1 0.2
4.1	A6	1455	224	0.2	3.9	-14.52	-24.2 0.2
5.2	NE4	4424	1162	0.3	2.5	- 4.60	- 1.1 0.2
6.5	A6	1024	171	0.2	6.3	-15.15	-21.6 0.3
7.6	A3	2062	403	0.2	6.8	-12.12	-19.8 0.12
8.5	B8	1145	143	0.1		-18.16	-21.0 0.2
9.2	B9	4912	927	0.2	8.4	-19.10	-23.0 0.12
10.1	A6	1672	302	0.2		-14.41	-22.6 0.2
10.9	NE11	9628	2945	0.3	9.5	-0-	-0-
13.0		568	198	0.3	11.6		
14.9	Field	1510	156	0.1	14.9	- 1.03	- 1.2 0.3
16.6	B18	806	193	0.2	16.6	-19.66	-22.1 0.2
17.2	B18	2762	237	0.1	18.0	"	"
18.0	B18	979	157	0.2	17.7	-20.10	-21.8 0.2
					18.5	0.05	0.05

Table 8, continued

Velocity (km s ⁻¹)	Region (name)	Total Power (Jy)	Cross Power (Jy) (0".016) [†]	Visibility	Velocity Range* (km s ⁻¹)	ΔX (" \pm ")	ΔY (" \pm ")
18.6	A18	559	201	0.4	18.3 to 10.5	-11.35 \pm 0.10	-21.2 \pm 1.0
20.2	A6	205	162	0.8	19.5 20.4	-14.90 0.08	-22.3 0.3
25.7	A18	378	137	0.4	24.4 25.5	-11.12 0.03	-21.1 0.2
27.8	A15	3150	2080	0.7	25.9 27.3	-14.66 0.04	-19.3 0.2
28.8	A15	1398	706	0.5		"	"
29.2	Field	369	81	0.3	29.0 30.3	-14.50 0.10	-20.4 0.4

[†]Fringe spacing at which cross power was measured.

*The emission in this velocity range was strong enough in some scans to set the peak fringe rate for that channel to the fringe rate of the listed feature.

TABLE 9

Orion H₂O Features 1978 July 22

Velocity (km s ⁻¹)	Region (name)	Total Power (Jy)	Cross Power (Jy) (0".037) [†]	Visibility	Velocity Range* (km s ⁻¹)	ΔX (" ± ")	ΔY (" ± ")
-4.2	Center	3209	1687	0.5	-4.6 to -3.8	- 8.56 ± 0.04	-13.71 ± 0.03
-3.2	A-2	451	156	0.3	-3.2	-15.01	-17.59
-2.0	A-2	840	734	0.9	-3.0	-15.00	-17.52
+1.5	A3	100	40	0.4	+1.5	-12.64	-18.97
2.9	NE11	< 921	188			near 11 km s ⁻¹	
3.2	A3	1034	769	0.7	2.7	-12.33	-18.96
4.2	A3		454			"	"
4.1	NE4	3570	2319	0.6	3.6	- 4.65	- 0.74
5.2	NE4	1210	1118	0.9		- 4.58	- 0.83
6.5	A6	378	190	0.5	6.3	-14.46	-21.47
7.8	A6	422	168	0.4	7.4	-13.72	-23.14
8.6	A18	< 452	203	0.4	8.4	-11.88	-20.96
9.2	B9	<1754	1133	0.6	8.8	-19.0	-22.4
9.9	NE11	4823	4756	1.0	9.5	+ 0.14	- 0.08
10.9	NE11	3022	1859	0.6	12.0	-0-	-0-
11.6	NE11					+ 0.32	+ 0.11
12.4	A6	220	110	0.5	12.2	-15.6	-22.2
					12.8	0.5	0.4

Table 9, continued

Velocity (km s^{-1})	Region (name)	Total Power (Jy)	Cross Power (Jy) (0."037) [†]	Visibility	Velocity Range (km s^{-1})	ΔX (" \pm ")	ΔY (" \pm ")
13.7	Center	245	38	0.2		- 8.8 \pm 0.7	-13.7 \pm 0.6
14.5	Center					- 6.0	-15.6
14.5	B18	474	125	0.3	14.3 to 15.0	-19.84	0.4
14.8							-21.31
15.8	Field	245	45	0.2	15.8	-10.3	+24.8
17.5	Center	824	131	0.2	17.5	- 7.4	-14.2
18.6	A18	500	600	1.2	18.3	-11.25	-21.00
20.6	Center	35	31	0.9	20.6	+ 5.09	-23.26
					21.1		0.50

[†]Fringe spacing at which cross power was measured.

*The emission in this velocity range was strong enough in some scans to set the peak fringe rate for that channel to the fringe rate of the listed feature.

TABLE 10

Orion H₂O Features 1978 November 2

Velocity (km s ⁻¹)	Region (name)	Total Power (Jy)	Cross Power (Jy) (0"211) [†]	Visibility	Velocity Range* (km s ⁻¹)	ΔX (" \pm ")	ΔY (" \pm ")
-7.0	Center	572	351	0.6	-7.6 to -6.5	-8.48 \pm 0.02	-14.1 \pm 0.3
-5.9	Center	266	49	0.2	-6.1	-8.74	-13.6
-4.2	Center	4567	4532	1.0	-5.1	-8.53	-14.2
-3.2	Center	505	276	0.5	-3.6	-8.6	-14.1
-2.3	A-2	937	809	0.9	-3.4 to	-15.03	-17.9
-1.8	A-2	1150	1250	1.0	-0.4	-15.03	-17.9
+1.7	A3	196	92	0.5	1.5	-12.16	-18.7
2.9	A3	2012	1578	0.8	1.3	-12.20	-19.5
3.0						Near	4.2
4.0						Near	2.9
4.2	NE4	4484	3231	0.7	2.3	-4.61	-1.0
5.2		450	300	0.7	5.5		0.1
6.1	NE6	4724	3752	0.8	5.7	-8.08	+3.2
6.7	A6	458	93	0.2	6.7	-15.15	-21.4
7.8	A6	946	742	0.8	7.2	-14.41	-23.1
8.8	Al8	1553	845	0.5	8.2	-11.46	-21.5
9.5	B9	<2600	914	0.3	8.8	-18.98	-23.9
9.8	NE11	6100	4000	0.7	9.5	0.16	-0.2
11.0	NE11	4180	2881	0.7	10.5	-0-	-0-
12.3	A6	600	200	0.3	12.0	-15.56	-23.0
13.4	Center	548	133	0.2	12.9	-9.31	-13.5
13.9	Field	700	156	>0.2	13.2	-9.52	23.3
					13.6		1.2
					14.0		

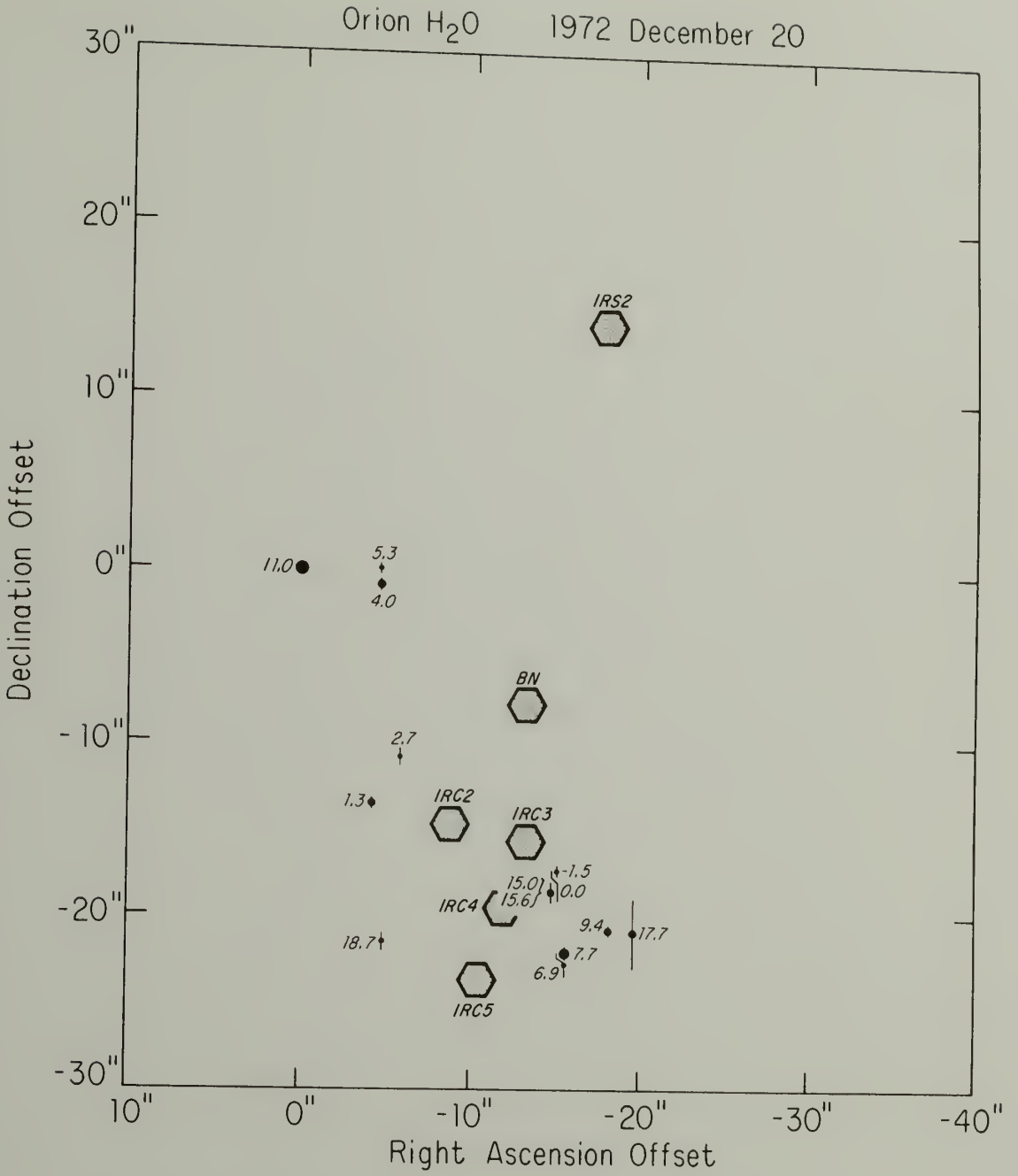
Table 10, continued

Velocity (km s^{-1})	Region (name)	Total Power (Jy)	Cross Power (Jy) (0"211) [†]	Visibility	Velocity Range* (km s^{-1})	ΔX (" \pm ")	ΔY (" \pm ")
14.4	B18	580	163	0.3	14.2 to 15.0	-19.95 \pm 0.12	-22.1 \pm 0.9
14.6	Center	762	240	0.3	14.2	- 9.31	-15.4
15.5	Center	470	36	0.1	14.6	- 9.58	-13.8
17.5	Center	1440	400	0.3	16.1	- 8.62	-13.9
18.0	B18	540	220	0.4	17.8	-19.60	-22.5
18.6	A18	1090	784	0.7	18.4	-11.32	-21.6
20.3	Field	263	109	0.4	19.7	+ 4.44	-21.5
21.6	A18	204	102	0.5	20.9	-11.42	-21.3
25.1	A18	300	200	0.6	24.3	-11.04	-21.6
27.1	A15	93	74	0.8	26.4	-14.59	-19.4
					27.5	0.03	0.5

[†] Fringe spacing at which cross power was measured.

* The emission in this velocity range was strong enough in some scans to set the peak fringe rate for that channel to the fringe rate of the listed features.

Fig. 21. A Mark II VLBI fringe rate map. The number identifying a maser is its LSR velocity (km s^{-1}). The amplitude of a feature is proportional to the area of the circle at the maser position. The bars are the formal errors from the least squares fit of the position offset to the relative fringe rates. A feature without error bars had offset uncertainties smaller than the circle. The error bars without \cdot 's indicate the position of a maser with a peak flux density less than 700 Jy. The origin of the axis is the position of the 11 (10.8 km s^{-1}) feature at $\alpha(1950) = 5^{\text{h}} 32^{\text{m}} 47^{\text{s}}58 \pm 0^{\text{s}}02$ and $\delta(1950) = 5^{\circ} 24' 9''.3 \pm 0''.5$ (Forster *et al.* 1978). The map has the same scale as Figure 8. The IRC sources are shown to facilitate the comparison of maps from different epochs.



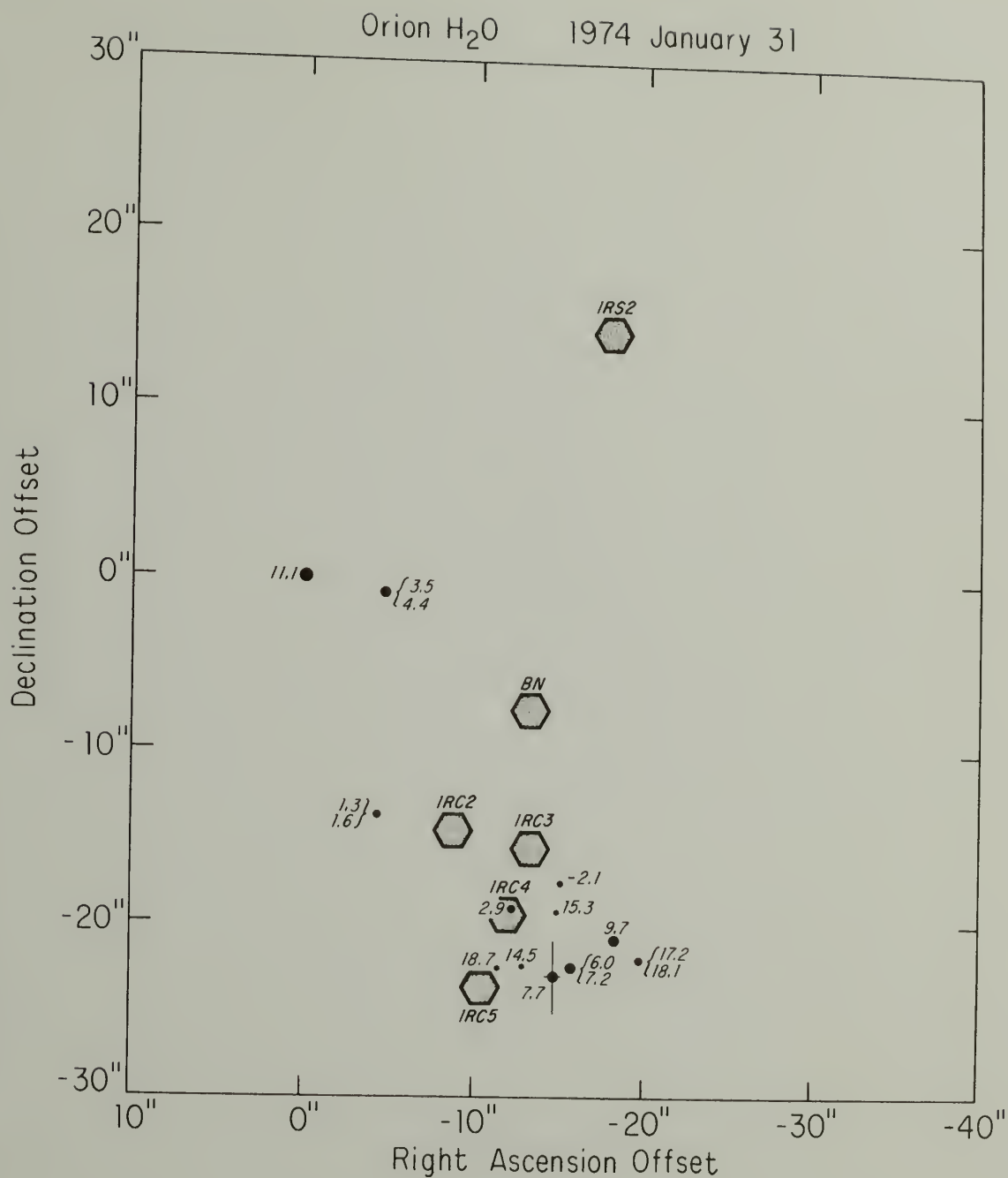


Fig. 22. A Mark II VLBI fringe rate map. A more detailed explanation of the map is given in the caption for Figure 21.

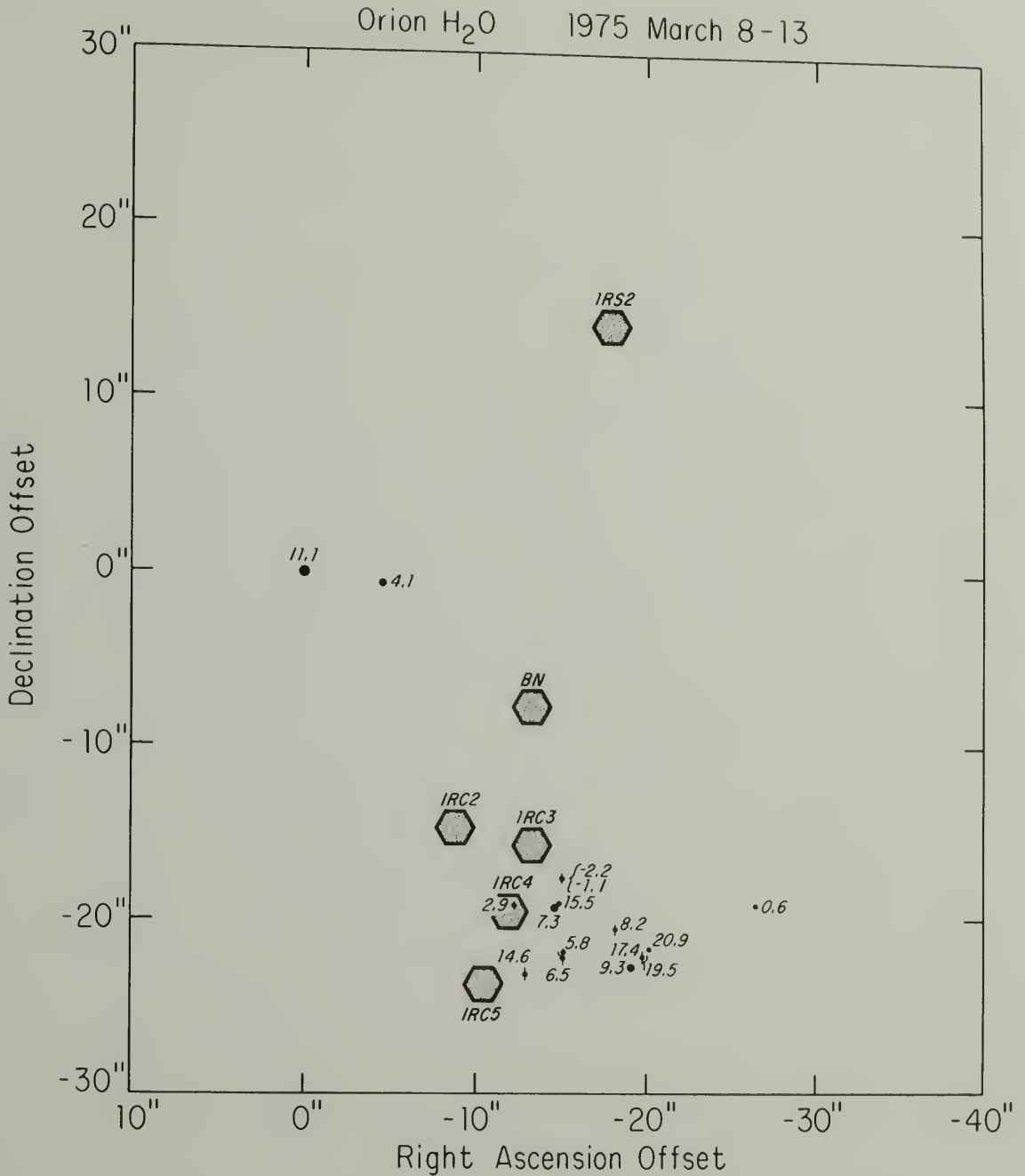


Fig. 23. A Mark II VLBI fringe rate map. A more detailed explanation of the map is given in the caption for Figure 21.

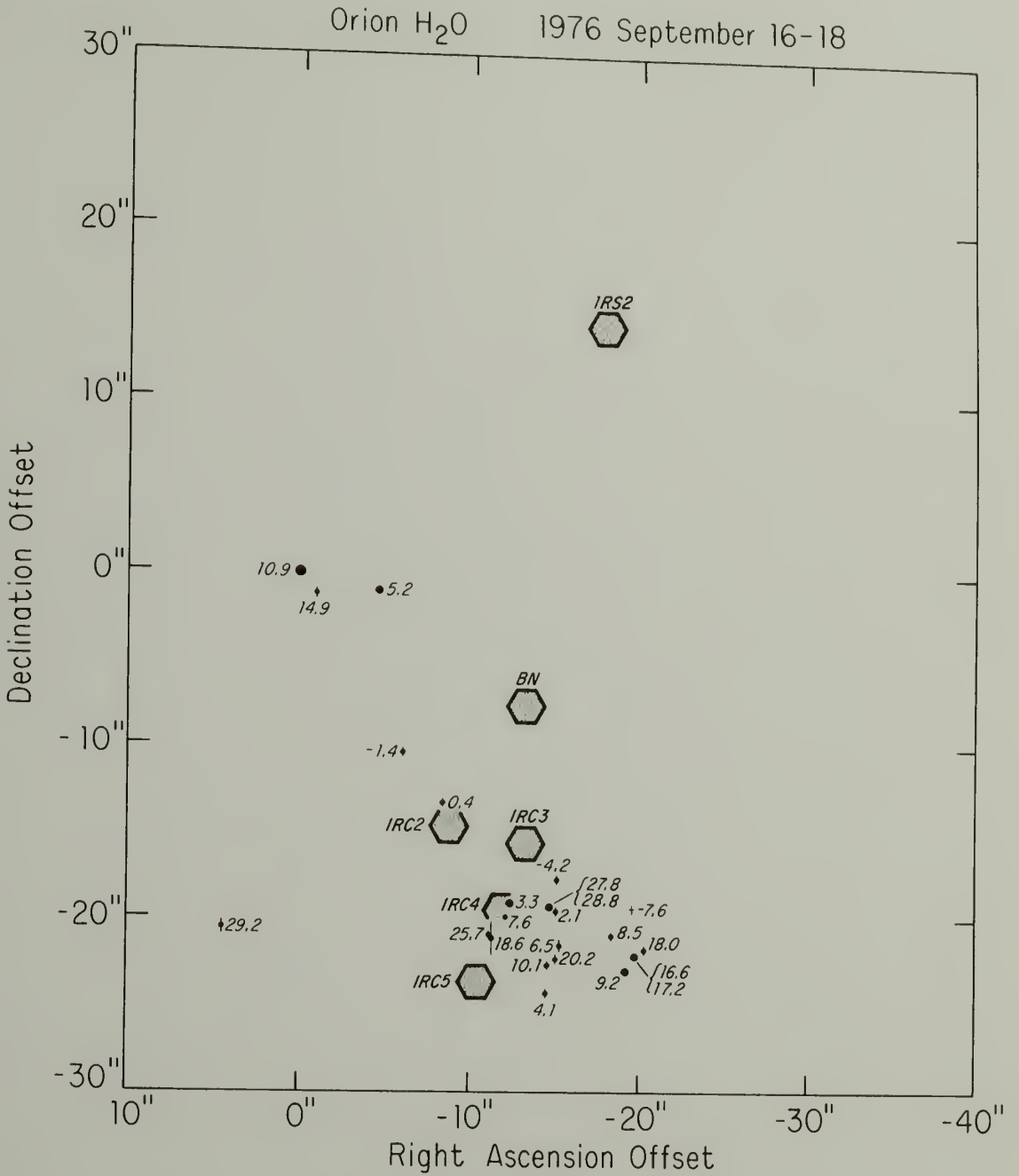


Fig. 24. A Mark II VLBI fringe rate map. A more detailed explanation of the map is given in the caption for Figure 21.

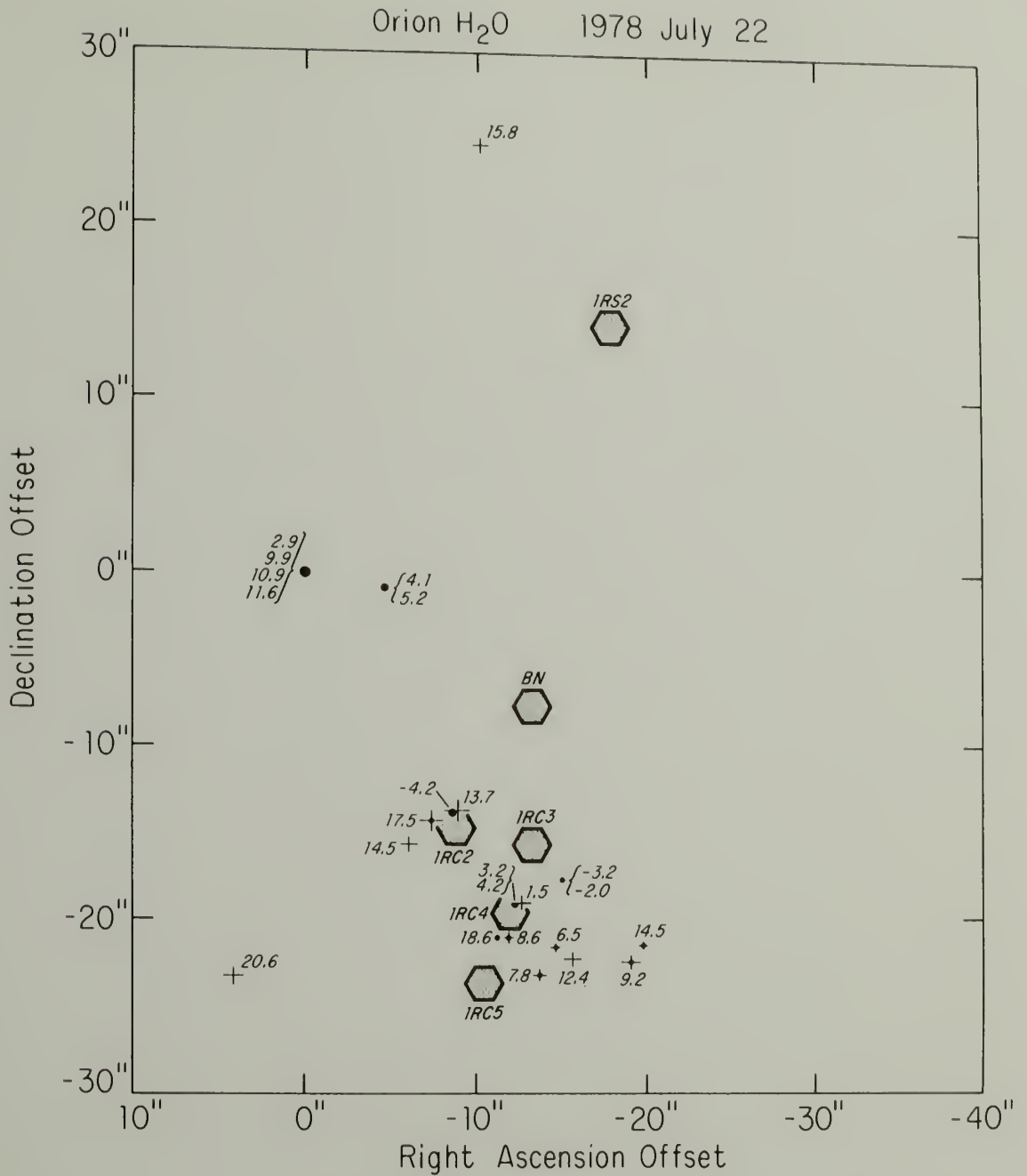


Fig. 25. A Mark II VLBI fringe rate map. A more detailed explanation of the map is given in the caption for Figure 21.

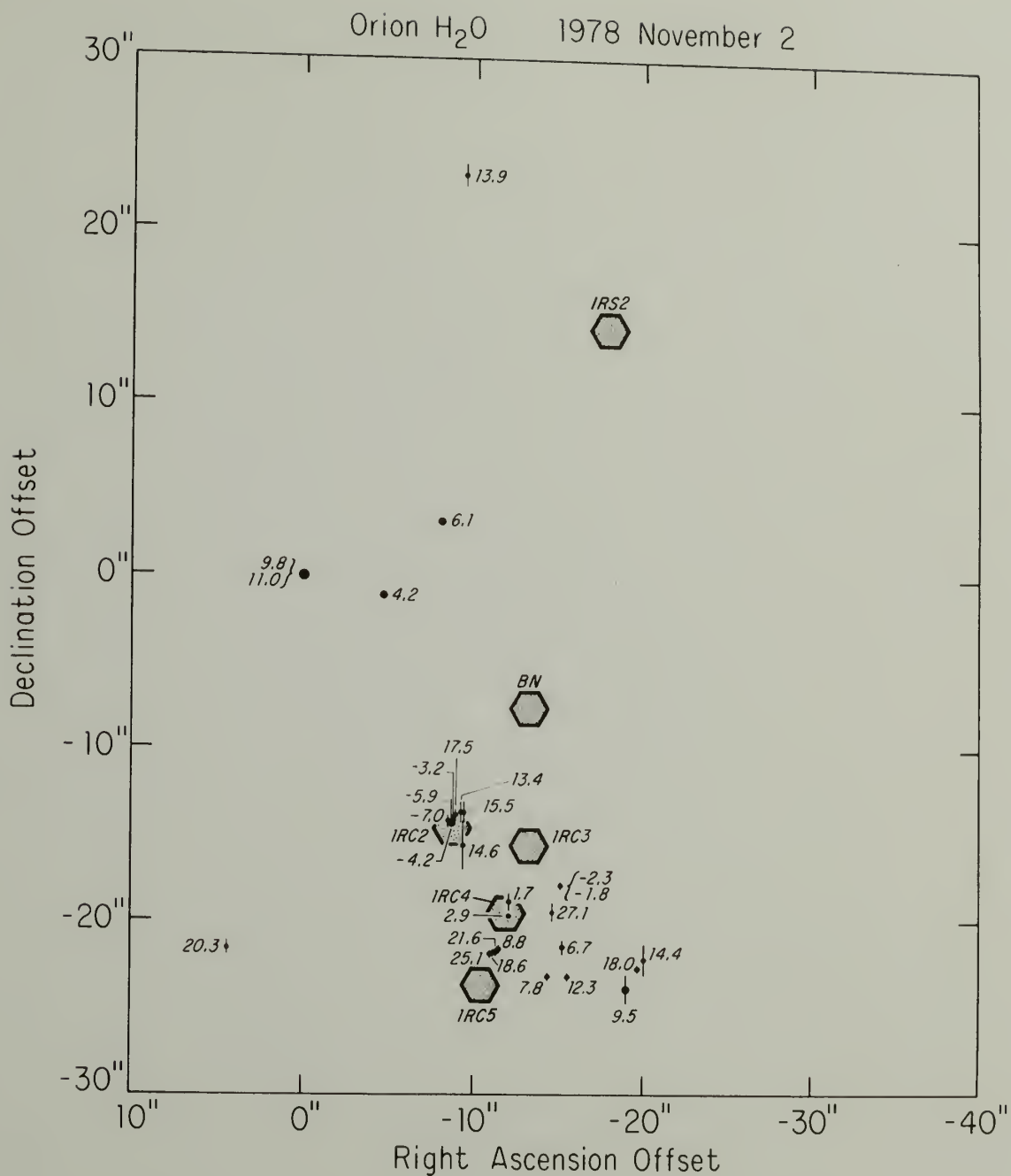
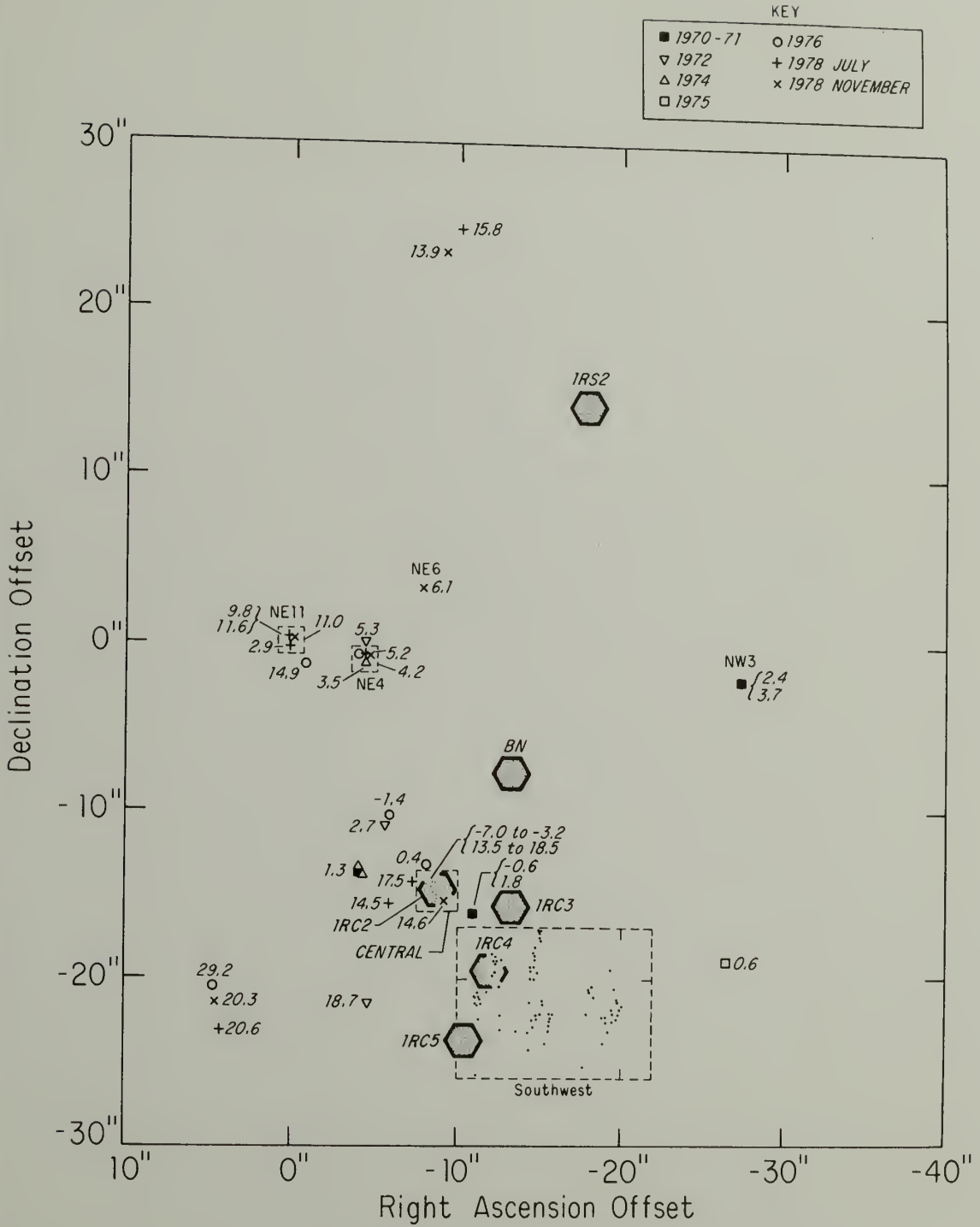


Fig. 26. A Mark II VLBI fringe rate map. A more detailed explanation of the map is given in the caption for Figure 21.

Fig. 27. A composite map of all water vapor masers seen in any of the six VLBI experiments of this dissertation plus those of Moran *et al.* (1973) in 1970 and 1971. A maser is again identified by its LSR velocity (km s^{-1}). The symbol indicates the epoch when the maser was present. The size of the symbol has no significance. Error bars are omitted for clarity. The small boxes in the northeast indicate the positions of the 11 and 4.2 km s^{-1} features. The 11 km s^{-1} feature was seen in all epochs and the 4.2 km s^{-1} feature was seen in all epochs except 1976 when it was probably hidden by a strong feature at 4.1 km s^{-1} at another position. The symbols in the boxes were within 200 a.u. of the 11 km s^{-1} or 4.2 km s^{-1} feature. The central box contains the shell features. Because of their large size, the shell features were mapped only on the short baseline experiment of 1978. An expanded map of the southwest section is shown in Figure 28.



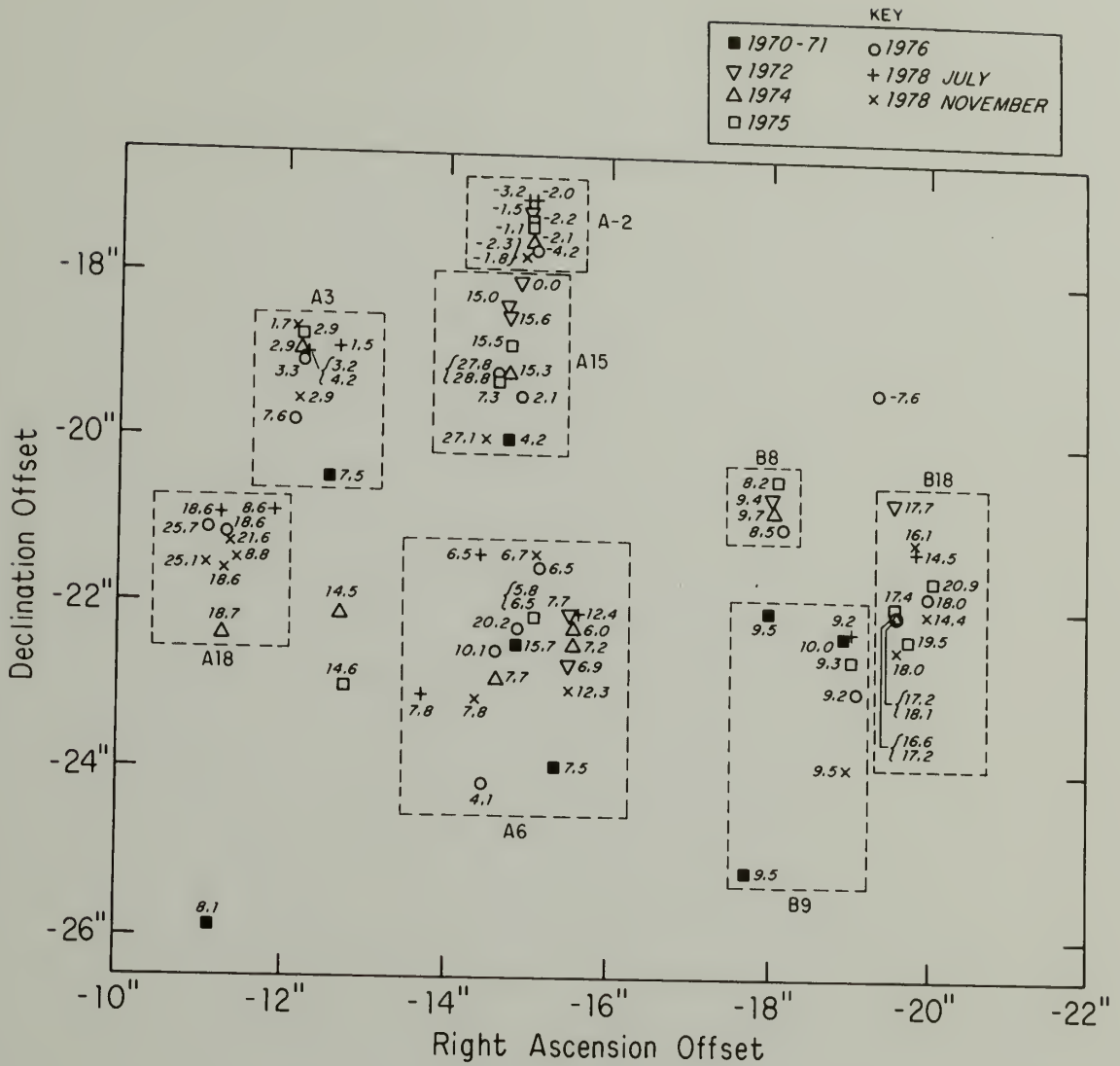


Fig. 28. An expanded scale composite map of the southwest cluster of masers. The broken lines delineate the clusters discussed in the text.

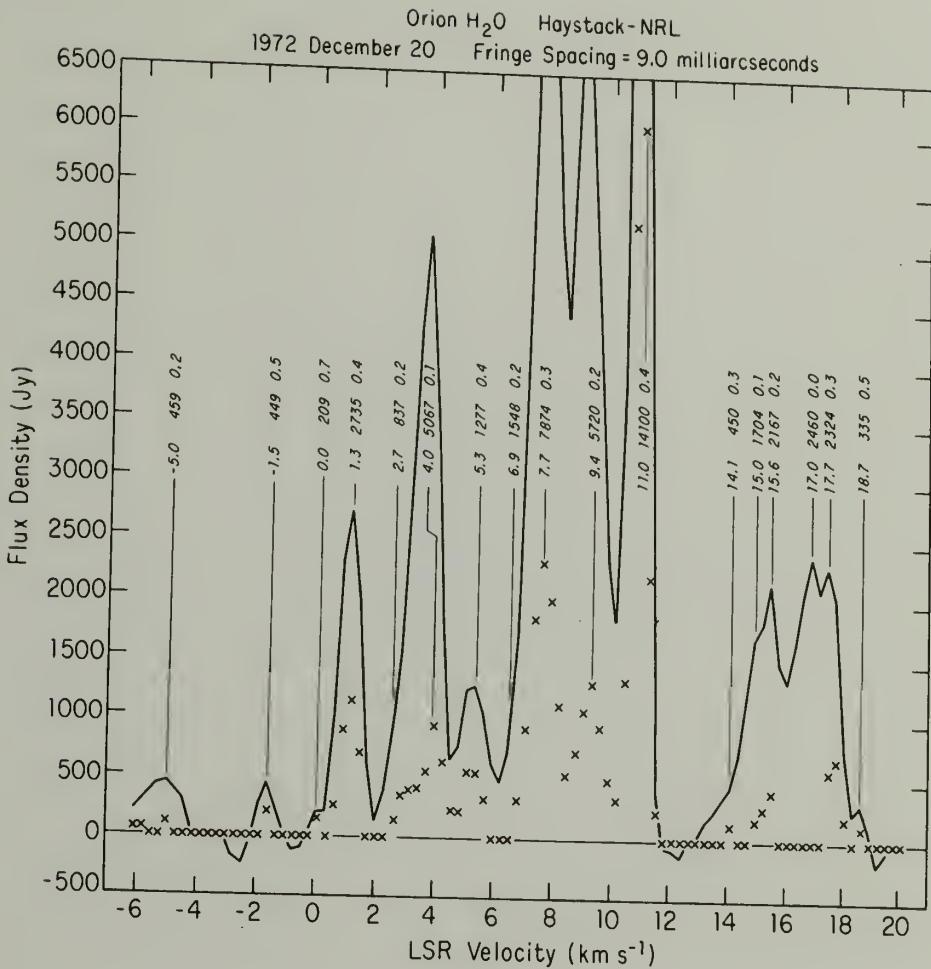


Fig. 29. A water vapor spectrum for Orion A. The solid line is the total power spectrum while the x's are the cross power spectrum, i.e., the amplitude of the strongest peak in the fringe rate spectrum for each velocity channel (see Chapter II). The fringe spacing at which the cross power spectrum was taken is given above the spectrum. Because most strong masers in Orion A are resolved, the cross correlated power is usually for the largest fringe spacing available. The numbers above the features are the velocity (km s⁻¹), total power (Jy), and visibility of the feature at this spacing. Other parameters of the spectral features are given in Tables 5 - 10.

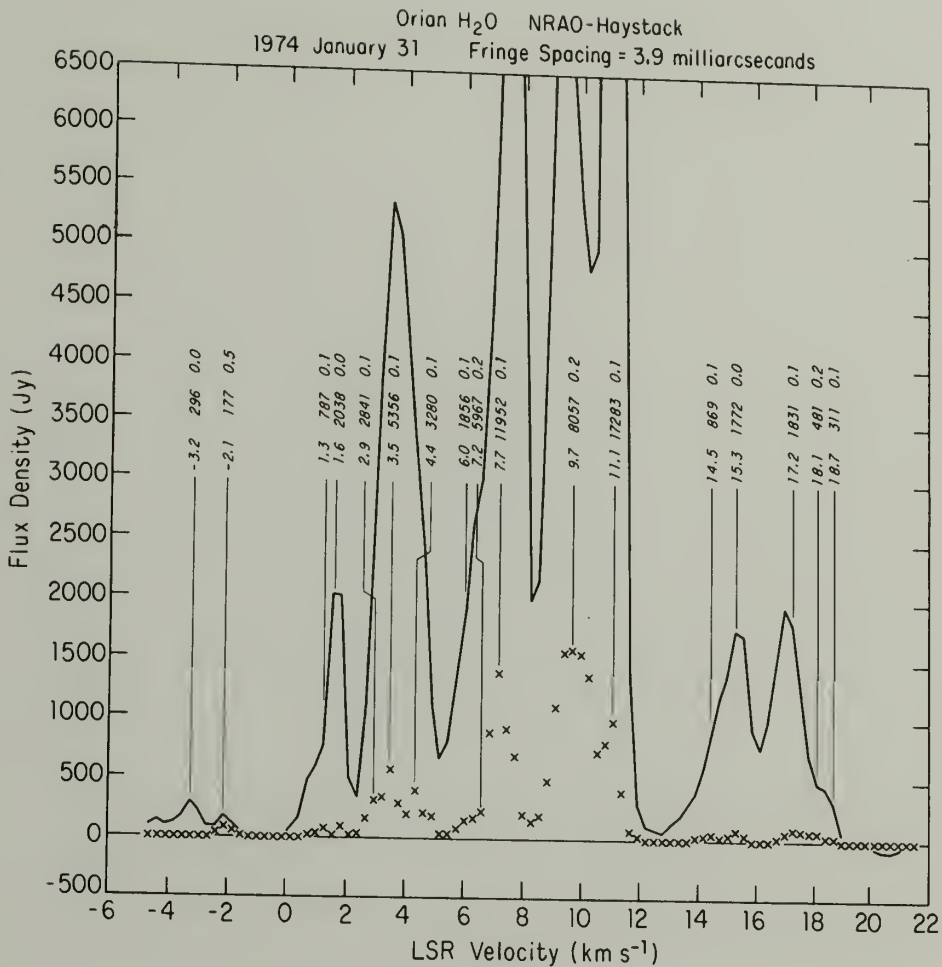


Fig. 30. A water vapor spectrum for Orion A. The solid line is the total power spectrum while the x's are the cross power spectrum, i.e., the amplitude of the strongest peak in the fringe rate spectrum for each velocity channel (see Chapter II). The fringe spacing at which the cross power spectrum was taken is given above the spectrum. Because most strong masers in Orion A are resolved, the cross correlated power is usually for the largest fringe spacing available. The numbers above the features are the velocity (km s⁻¹), total power (Jy), and visibility of the feature at this spacing. Other parameters of the spectral features are given in Tables 5 - 10.

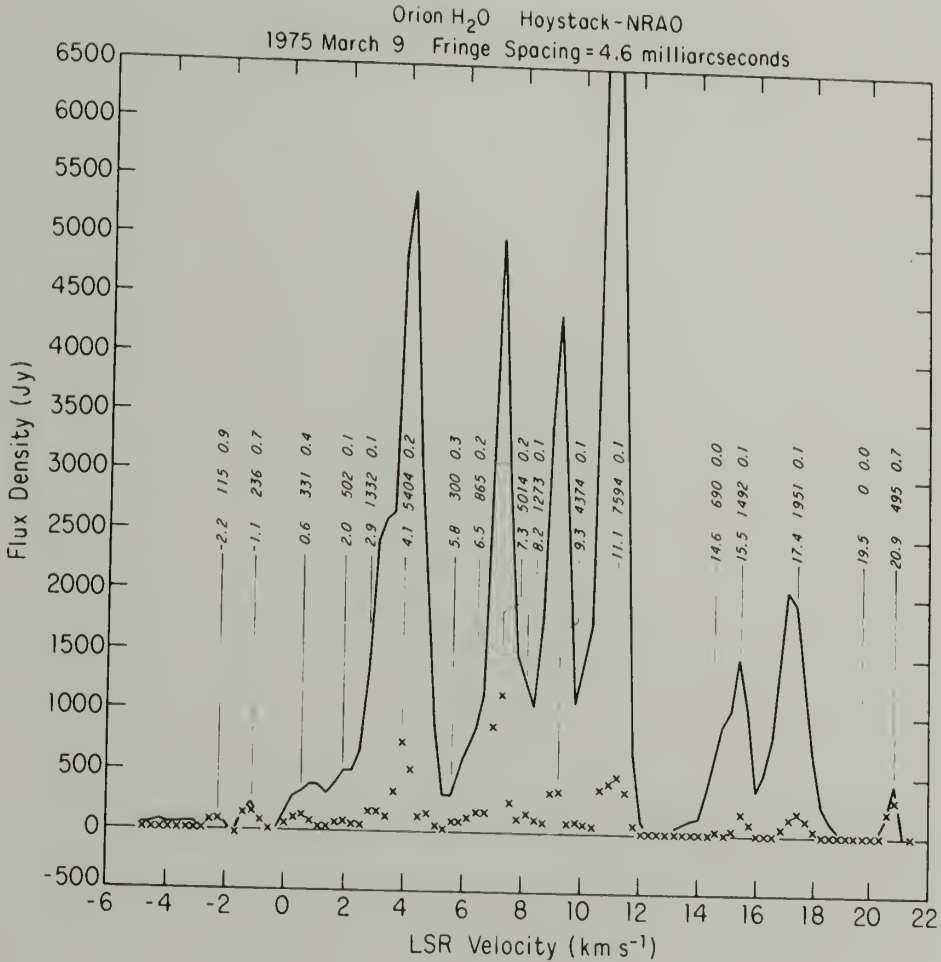
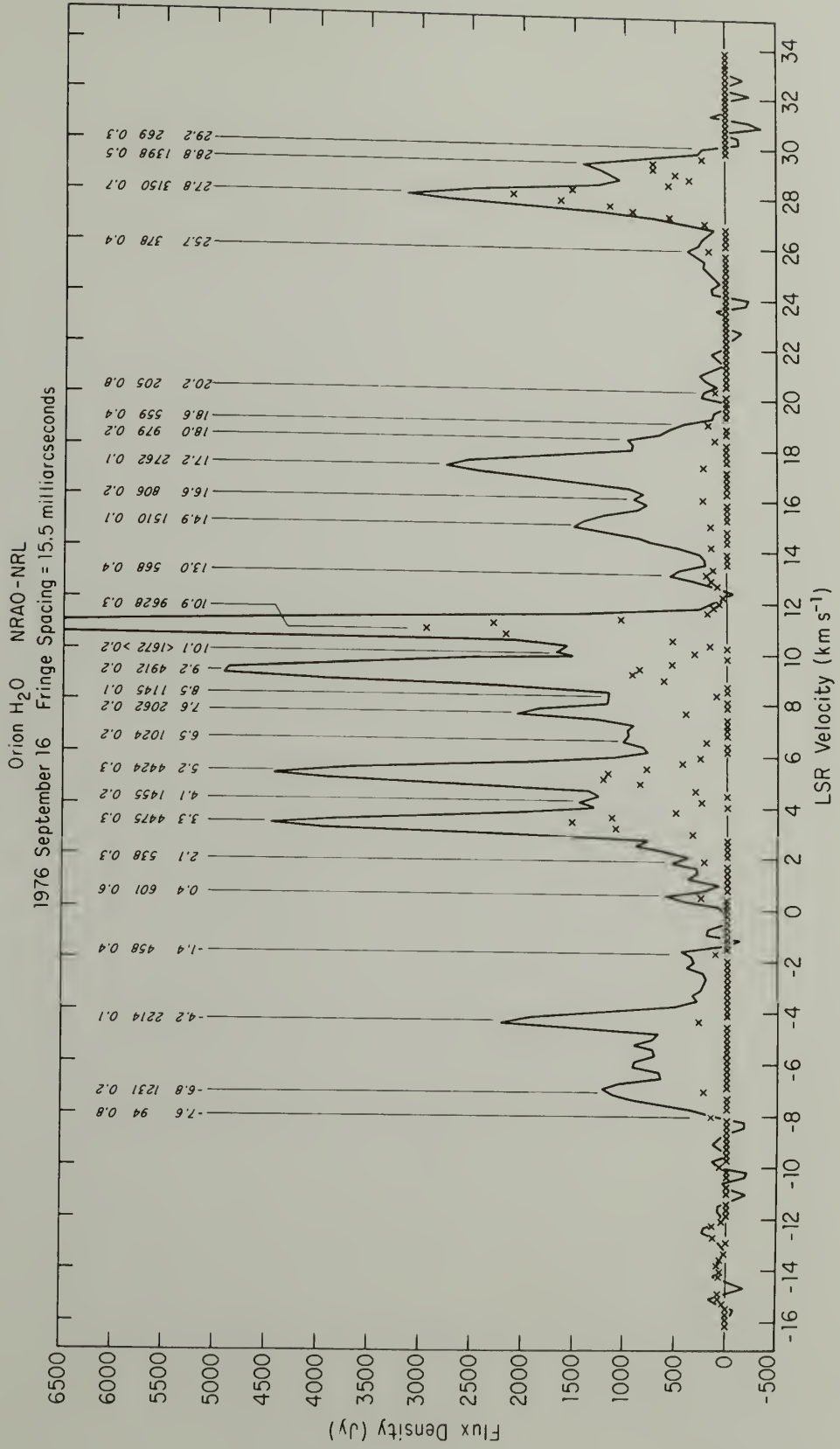


Fig. 31. A water vapor spectrum for Orion A. The solid line is the total power spectrum while the x's are the cross power spectrum, i.e., the amplitude of the strongest peak in the fringe rate spectrum for each velocity channel (see Chapter II.) The fringe spacing at which the cross power spectrum was taken is given above the spectrum. Because most strong masers in Orion A are resolved, the cross correlated power is usually for the largest fringe spacing available. The numbers above the features are the velocity (km s⁻¹), total power (Jy), and visibility of the feature at this spacing. Other parameters of the spectral features are given in Tables 5 - 10.

Fig. 32. A water vapor spectrum for Orion A. The solid line is the total power spectrum while the x's are the cross power spectrum, i.e., the amplitude of the strongest peak in the fringe rate spectrum for each velocity channel (see Chapter II). The fringe spacing at which the cross power spectrum was taken is given above the spectrum. Because most strong masers in Orion A are resolved, the cross correlated power is usually for the largest fringe spacing available. The numbers above the features are the velocity (km s^{-1}), total power (Jy), and visibility of the feature at this spacing. Other parameters of the spectral features are given in Tables 5 - 10.



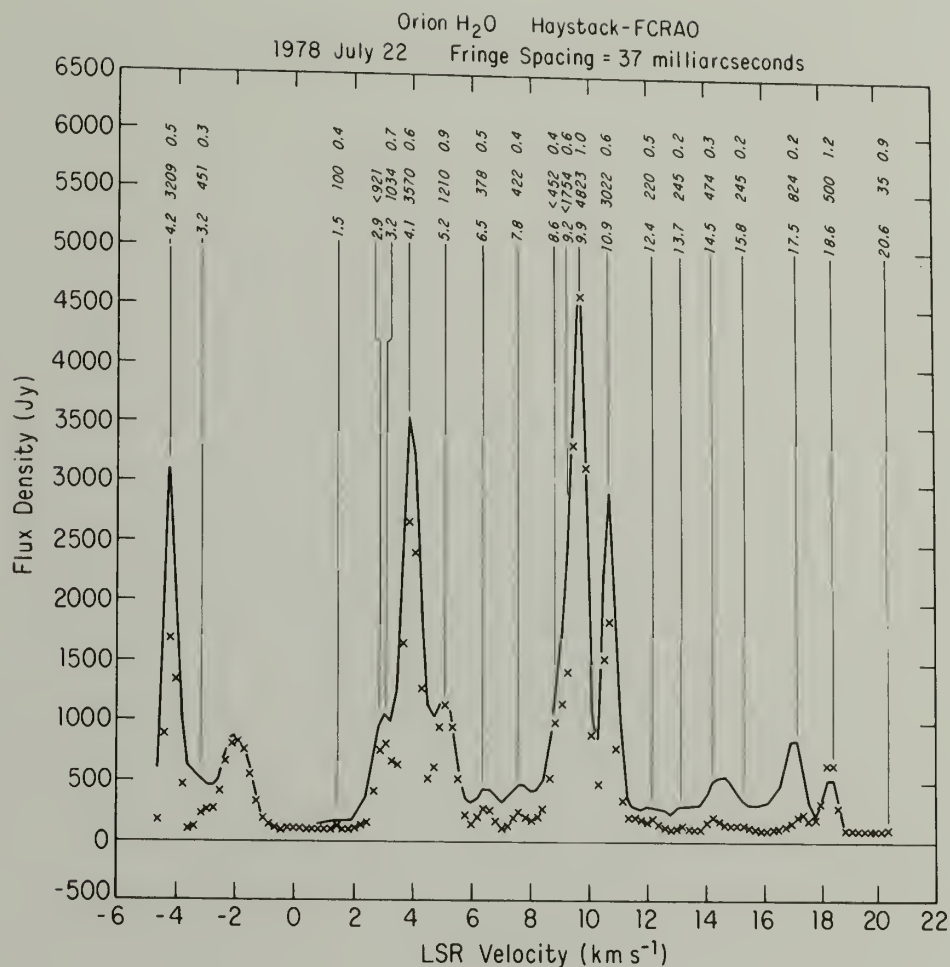
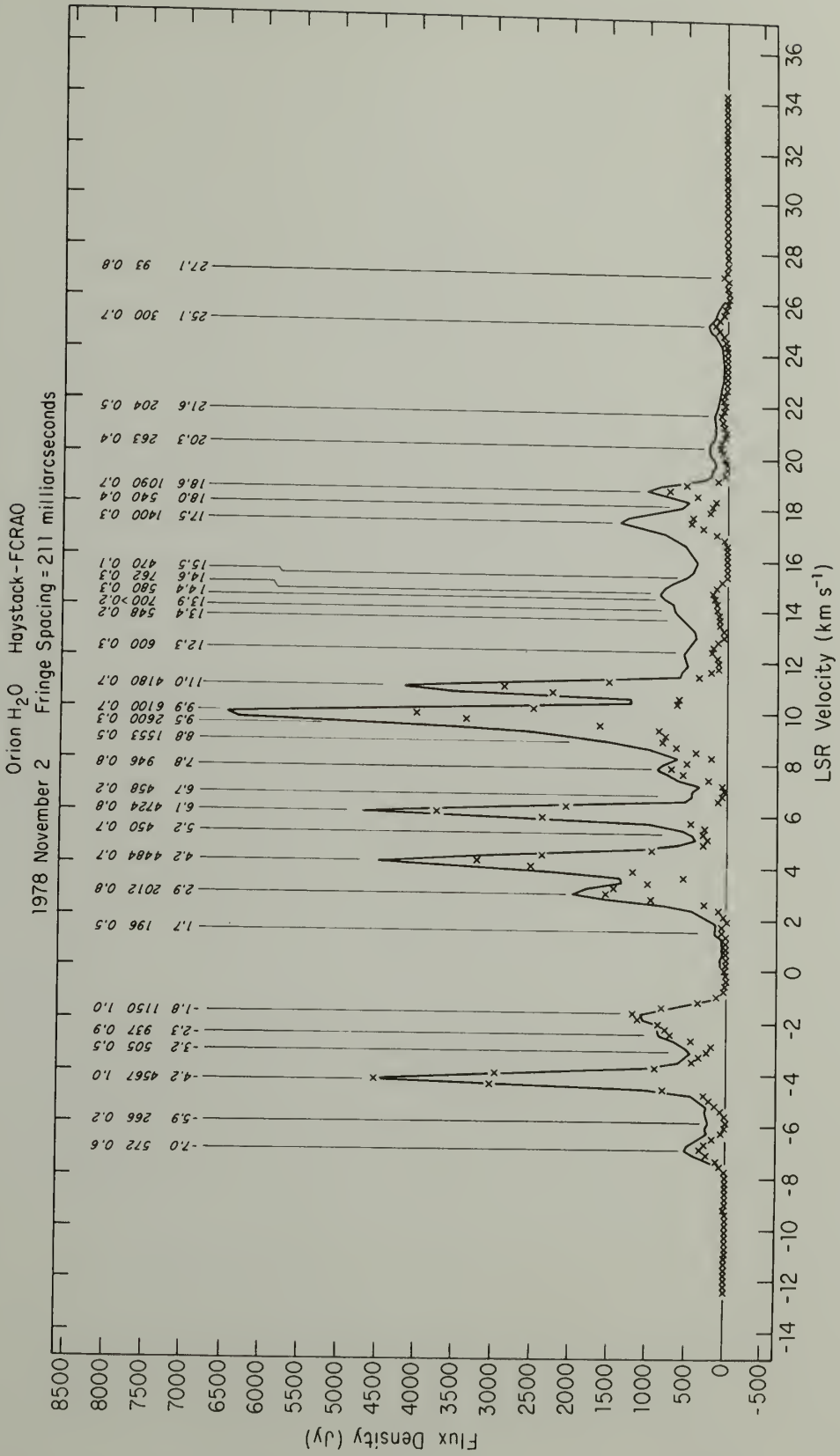


Fig. 33. A water vapor spectrum for Orion A. The solid line is the total power spectrum while the x's are the cross power spectrum, i.e., the amplitude of the strongest peak in the fringe rate spectrum for each velocity channel (see Chapter II). The fringe spacing at which the cross power spectrum was taken is given above the spectrum. Because most strong masers in Orion A are resolved, the cross correlated power is usually for the largest fringe spacing available. The numbers above the features are the velocity (km s⁻¹), total power (Jy), and visibility of the feature at this spacing. Other parameters of the spectral features are given in Tables 5 - 10.

Fig. 34. A water vapor spectrum for Orion A. The solid line is the total power spectrum while the x's are the cross power spectrum, i.e., the amplitude of the strongest peak in the fringe rate spectrum for each velocity channel (see Chapter II). The fringe spacing at which the cross power spectrum was taken is given above the spectrum. Because most strong masers in Orion A are resolved, the cross correlated power is usually for the largest fringe spacing available. The numbers above the features are the velocity (km s^{-1}), total power (Jy), and visibility of the feature at this spacing. Other parameters of the spectral features are given in Tables 5 - 10.



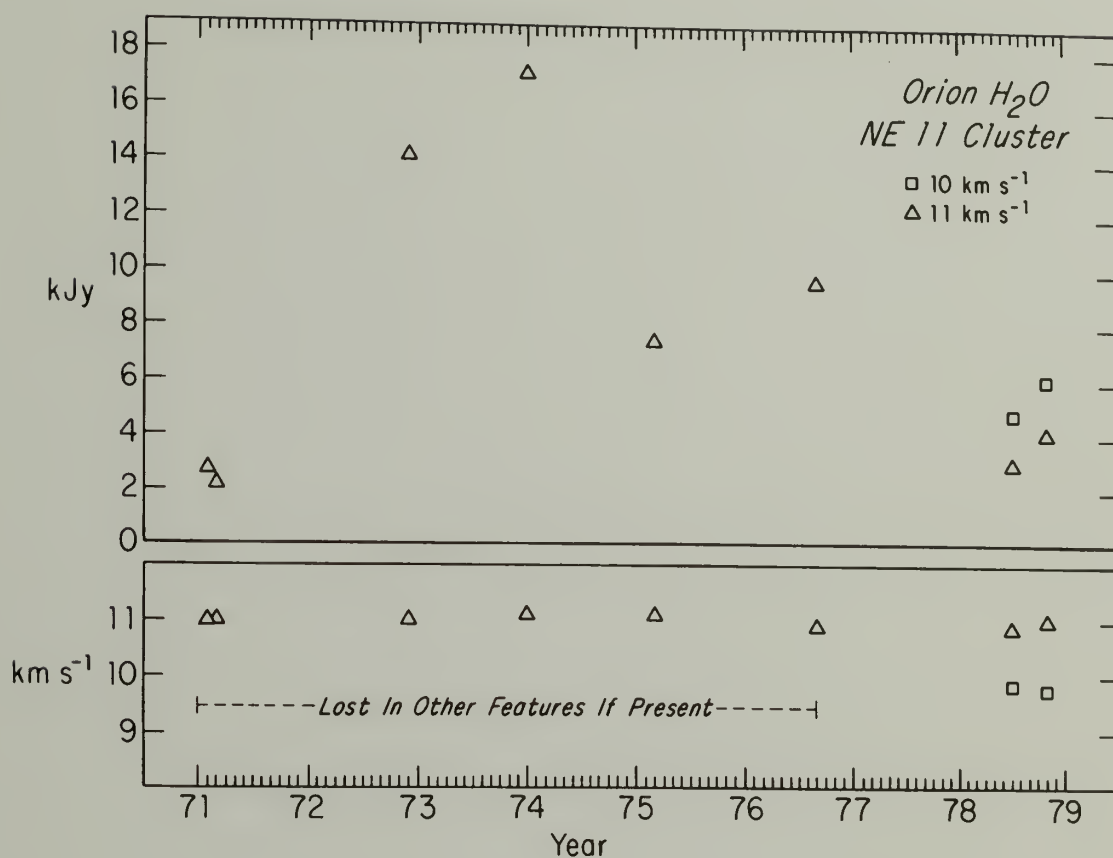


Fig. 35. The intensities and velocities of the 10 and 11 km s⁻¹ features in the NE11 cluster at each VLBI epoch. Similar graphs were produced for each cluster, but since no correlation was seen only one sample is given.

Orion. A cluster is named by the subsection of the map in which it appears and the velocity of its most distinguished component. The clusters in the northeast are NE11 and NE4. The central section of the map is named the "central" region. The H₂O, OH and SiO spectral features from this cluster probably arise in an expanding shell of gas about a star. The map becomes more complicated to the southwest. Genzel and Downes (1977a) combine several clusters into "sources" which they designate "A" and "B". I name a cluster with this "source" letter and velocity. Thus a cluster is denoted by x# for the # km s⁻¹ feature in the "x" group. If several features appear in a cluster, the velocity of the longest lasting one or the one which is not seen at any other position is used. Thus, the cluster containing the 15 km s⁻¹ feature in source "A" is A15.

For each cluster I have prepared a chart showing the intensity and velocity of the features arising from it. A sample is shown in Figure 35. These charts show no correlated intensity or velocity variations. In the following section I will discuss each cluster (but not each velocity feature) as if it were independent. In Section 3.3, I will discuss possible groupings of the clusters.

3.2.1 NE11. The most constant feature in Orion is the 11 (10.8 to 11.1) km s⁻¹ feature in the northeast corner of the maser region. Moran et al. (1973) first determined the feature position in 1971 March. They did not show a position for this feature in the 1971 February map, although it had the same intensity in that spectra as it did in the 1971 March spectra. In 1970 June its intensity was

less than 200 Jy. Sullivan (1971) found this feature to be constant and unpolarized with a total flux of 2000 Jy between 1969 January and 1970 March. Little, White, and Riley (1977) observed this feature increase from 15 000 Jy in 1974 August to 30 000 Jy in 1976 February. There was no noticeable line narrowing during the increase. The feature was constant in velocity and linewidth as Sullivan (1971) found it in 1969. At 30 000 Jy, it was the strongest maser ever seen in Orion.

The 1978 maps also show a 9.8 km s^{-1} feature in this location. It was the strongest feature in the spectra in 1978 July and 1978 November. The 9.8 km s^{-1} maser is offset from the 11.0 km s^{-1} maser by about 100 a.u. ($0''.2$).

3.2.2 NE4. A second distinct cluster on the Orion maps lies five seconds west of the 11 km s^{-1} feature. It is constant in position and contains velocity features ranging from 3.3 to 5.2 km s^{-1} . This cluster often has two features separated by 1 km s^{-1} in velocity. They are coincident to within the error bars (5 to 50 a.u.). The features have varied from undetectable to 5000 Jy. There has been a feature of at least 4000 Jy in this position at each epoch.

3.2.3 NE6. This is a new, strong feature in a new position with a flux density of 4700 Jy. It first appeared in 1978 November. A careful reexamination of the 1978 July data revealed no hint of it to the level of 200 Jy. Genzel and Downes (1977a) found a weak feature at -92.8 km s^{-1} whose error bars ($\pm 2''$) covered this position.

3.2.4 NW3. This cluster was seen only in the earliest (1970-1971) maps (Moran et al. 1973). It had strong features at 2.4 km s^{-1} (700 Jy) and 3.7 km s^{-1} (3400 to 1500 Jy). My maps show no features near this position in any of the six epochs. In 1979, Genzel (private communication) found a weak feature at 1.0 km s^{-1} within $1''$ of this cluster.

3.2.5 The Central Region. The central region is sometimes called the "shell" region because the H_2O , OH and SiO spectra from this position display a pattern expected from an expanding shell of gas about an evolved(?) star. The central region is located $15''$ southwest of the 11 km s^{-1} feature. Its masers may be generically different from the other masers. The masers of the central region are spread over an area 1000 a.u. ($2''$) in diameter. Emission in the velocity range -7.5 to -3.2 km s^{-1} , 13.2 to 15.0 km s^{-1} , and 17.2 to 18.0 km s^{-1} comes from this region. The typical flux densities are less than 1000 Jy .

It was only with the 1978 November 2 VLBI observations between Haystack and FCRAO which included the largest fringe spacing (0.2 or 100 a.u.) ever obtained in an H_2O VLBI experiment that these shell features were not highly resolved. I determined the diameter of the -4.2 km s^{-1} feature to be $10 \pm 10 \text{ a.u.}$, the diameter of the -7.0 km s^{-1} feature to be between 15 and 40 a.u. , and the diameters of the 14.6 and 17.4 km s^{-1} features to be between 10 and 60 a.u. The large uncertainty in the size is the result of the difficulty in determining what fraction of the total power to attribute to a resolved source at

the central position, and what fraction to attribute to emission from other positions. This problem was discussed in Chapter II "Data Analysis". In an attempt to overcome this problem, I coherently integrated the cross correlated data for a long period of time at the central position and at the B18 position. The B18 cluster contained several features at the same velocity as the shell features. I removed the correlated flux of the features at B18 from the total flux before calculating the visibility for the central features. It did not make a great deal of difference. Hence, the shell features are truly resolved unless there is weak emission from other positions at these velocities. The same correction process was applied to the visibilities of the B18 features.

Relatively constant intensity was a common property of the shell features. The dramatic increase of the -4.2 km s^{-1} feature from 2200 Jy in 1976 to 4600 Jy in 1978 has changed that. The VLBI coverage of the -4 to -8 km s^{-1} region of the spectrum only began in 1976 September with the taking of frequency switched data. The -4.2 km s^{-1} feature lies at the edge of a 2 MHz bandpass centered at 8 km s^{-1} .

3.2.6 A-2. The low velocity shell features were originally placed in this cluster because the true shell features were resolved. The flux densities were 1000 Jy or less.

3.2.7 A3. This cluster shows emission from 2.4 to 3.7 km s^{-1} . In 1978 it also showed emission at 1.5 km s^{-1} . Its features, which are typically 1000 to 2000 Jy, are often masked by emission from the NE4 cluster.

The 1976 September H_2O map shows a 7.6 km s^{-1} feature of 2100 Jy with a 3.3 km s^{-1} feature of 4500 Jy displaced from it by $(-0''.1, +0''.7)$. The OH map of 1976 May showed a 3.8 km s^{-1} feature displaced from the 7.1 and 8.6 km s^{-1} features by $(-0''.1, +0''.8)$ (see Section 4.1). The errors in the H_2O positions allow for the differences. The absolute positions agree to within $1''$, but the one sigma error bar in declination for the OH absolute position was $5''$. The three OH features had recently increased in intensity. This may be the first precise coincidence of OH and H_2O masers. Future observation with the VLA will conform or disprove this.

3.2.8 A6. The masers in this cluster are the best candidates to study in the search for transverse motion. The features between 6 and 8 km s^{-1} have flux densities of a few thousand Janskys. The 7.7 km s^{-1} feature reached 12 000 Jy in 1974. However, in this region of the spectrum many lines blend together and features less than 1000 Jy would be lost in other features. The features in this cluster at other velocities have typical flux densities of a few hundred Janskys. The cluster has had two features in the velocity range from 6.5 to 7.8 km s^{-1} from 1972 to 1978. The 6.5 km s^{-1} feature has shown steady motion toward the northeast. The declination uncertainties from one epoch to the next overlapped. The right ascension error bars from one epoch to the next also overlapped except between 1974 and 1975 when the feature shifted $0''.5$ to the east. The projected shift in position between 1972 and 1978 was 600 a.u., which requires an average velocity of 500 km s^{-1} . This would be the highest velocity

ever observed for a water vapor maser. An alternative explanation is that a feature at the first position was replaced by another 600 a.u. away between 1974 January and 1975 March. Because water vapor masers change on a time scale of a few months while the observations were separated by 14 months, this is a plausible argument. It is, in fact, more plausible than a 500 km s^{-1} maser. The 7.4 km s^{-1} feature had even more erratic position shifts. In 1975 and 1976 emission near 7.4 km s^{-1} was dominated by stronger features in other clusters. In the epochs when the 7.4 km s^{-1} maser was seen in the A6 cluster, its position had large error bars caused by blending with other features. For these reasons, it is difficult to attribute the apparent shift of the 7.4 km s^{-1} maser to transverse motion. If the shift were due to transverse motion, the velocity would be 500 km s^{-1} . In future experiments more attention should be given to this cluster.

3.2.9 A15. Over the years this position has shown emission at 0.0, 2.1, 4.2, 7.3, 15.0 to 15.6, 27.1, 27.9, and 28.8 km s^{-1} . The most constant feature is at 15 km s^{-1} . However, it is highly resolved. Most of the emission at this velocity probably comes from the central cluster, and the component that is mapped in this cluster is a weak unresolved maser. Thus, the flux density cannot be measured. There was a strong source of 5000 Jy at 7 km s^{-1} in this cluster in 1975 March (the strongest in the cross power spectra). However, in 1974 and 1976 the emission at 7 km s^{-1} came from different clusters. The features at 27 and 28 km s^{-1} with a flux density of 3200 Jy and 1400 Jy are from this cluster. Their velocity changed by 0.7 km s^{-1}

in six months but they remain separated by 1 km s^{-1} .

3.2.10 A18. This cluster has had several features of 1000 Jy or less since 1976. It has features at 8.7 , 18.6 and 25 km s^{-1} . The 18.6 km s^{-1} emission is polarized. The 8 and 18 km s^{-1} emission is blended with radiation from other positions. At other epochs there has been emission within a few seconds of this position (outside the error bars) between 7.5 and 8.1 km s^{-1} and at 18.7 km s^{-1} . The 25 km s^{-1} emission was not in the observed VLBI bandpass before 1976.

3.2.11 B8. This is a simple cluster. It has shown only one feature in four epochs. It had emission around 9.5 km s^{-1} in 1972 (5700 Jy) and 1974 (8100 Jy) (and possibly in 1971) and around 8.4 km s^{-1} in 1975 (1300 Jy) and 1976 (1100 Jy). This is the clearest case of a feature at one velocity being replaced by another 1 km s^{-1} from it at the same position. In 1978 there was no emission from this cluster.

3.2.12 B9. Emission from 9.2 to 9.5 km s^{-1} with flux density between 1000 and 6000 Jy has come from this region in most epochs. However, the positions have varied by hundreds of astronomical units, probably because of blending. Emission at 9 km s^{-1} has dominated the spectra at three different epochs. Each time it has had a different position. This velocity is near the general cloud velocity of 8 km s^{-1} and one might expect 9 km s^{-1} to be a commonly occurring velocity.

3.2.13 B18. Emission has been seen from 14.4 to 20.9 km s^{-1} from this cluster at different epochs. Some feature has been seen in this

cluster in each map since 1972. The peak flux density was always less than 1000 Jy.

3.2.14 Nondetections. It is interesting to note that no masers have been detected within 3000 a.u. of the Becklin-Neugebauer object. There are no water vapor masers coincident with IRC3, IRS2, or the peaks of H₂ emission at 2.12 μ m.

3.3 Discussion

Several important conclusions can be drawn from my observations of the water vapor masers. The first deals with the spatial relationship among the individual velocity features. The most basic spatial grouping is a "cluster". A cluster consists of one or more velocity features which are often not coincident but are within 1000 a.u. (2") of one another. The position of a velocity feature is constant over years to 50 a.u. Since it cannot be said with certainty that a cluster has appeared and disappeared, the lifetime of a cluster is probably longer than the ten years over which H₂O masers have been observed. One cluster has disappeared (NW3), and at least one new one has appeared (NE6). The appearance of other new clusters might be attributed to wider velocity coverage, improved sensitivity, or changes in the relative intensity of blended features. The individual velocity features also last several years, although they show intensity variations on a time scale of weeks.

The intensity and variability of a water vapor maser are functions of its location. The northeast masers are strong, long lasting,

and occur in isolated clusters. The southwest masers are more variable, less intense, and occur in clusters which almost blend into one another. The individual velocity features of the southwest clusters come and go, but the clusters themselves remain. The masers in the central cluster are not very intense, and they change slowly. They are, as noted before, larger than the other masers. In addition to the masers which occur in clusters, weak emission is seen from random positions in the maser field. Table 11 shows the number of masers as a function of intensity and position. All the masers at different epochs were counted as separate masers. This technique, which counts long lasting masers several times, gives an indication of the duration of a feature. The most significant point to note from the table is that although only 17% of the masers were in the northeast, 57% of the masers with flux densities over 5000 Jy were in the northeast. The southwest clusters, which had 60% of all the masers observed, had the remaining 43% of the masers over 5000 Jy. Alternatively, 40% of all the masers in the northeast were over 5000 Jy while only 8% of the masers in the southwest were over 5000 Jy. None of the central cluster masers or the field masers were over 5000 Jy. Thus, there seems to be a strong correlation of intensity with position. Later, I will associate these four classes of masers (and a fifth class, the high velocity masers) with different evolutionary stages of a star.

The most likely velocity separation between features in a cluster is 1 km s^{-1} , but separations as large as 27 km s^{-1} have been seen. The histogram in Figure 36(a) shows the number of pairs of velocity

TABLE 11

The Number of H₂O Masers in Orion as a Function
of Flux Density and Position

Flux Density (kJy)	Northeast Clusters	Southwest Clusters	Central Cluster	Field Masers	Total
0 - 1	2	37	9	13	61
1 - 2	2	16	1	1	20
2 - 3	0	8	0	2	10
3 - 4	3	1	1	0	5
4 - 5	5	3	1	0	9
> 5	8	6	0	0	14
Total	20	71	12	16	119

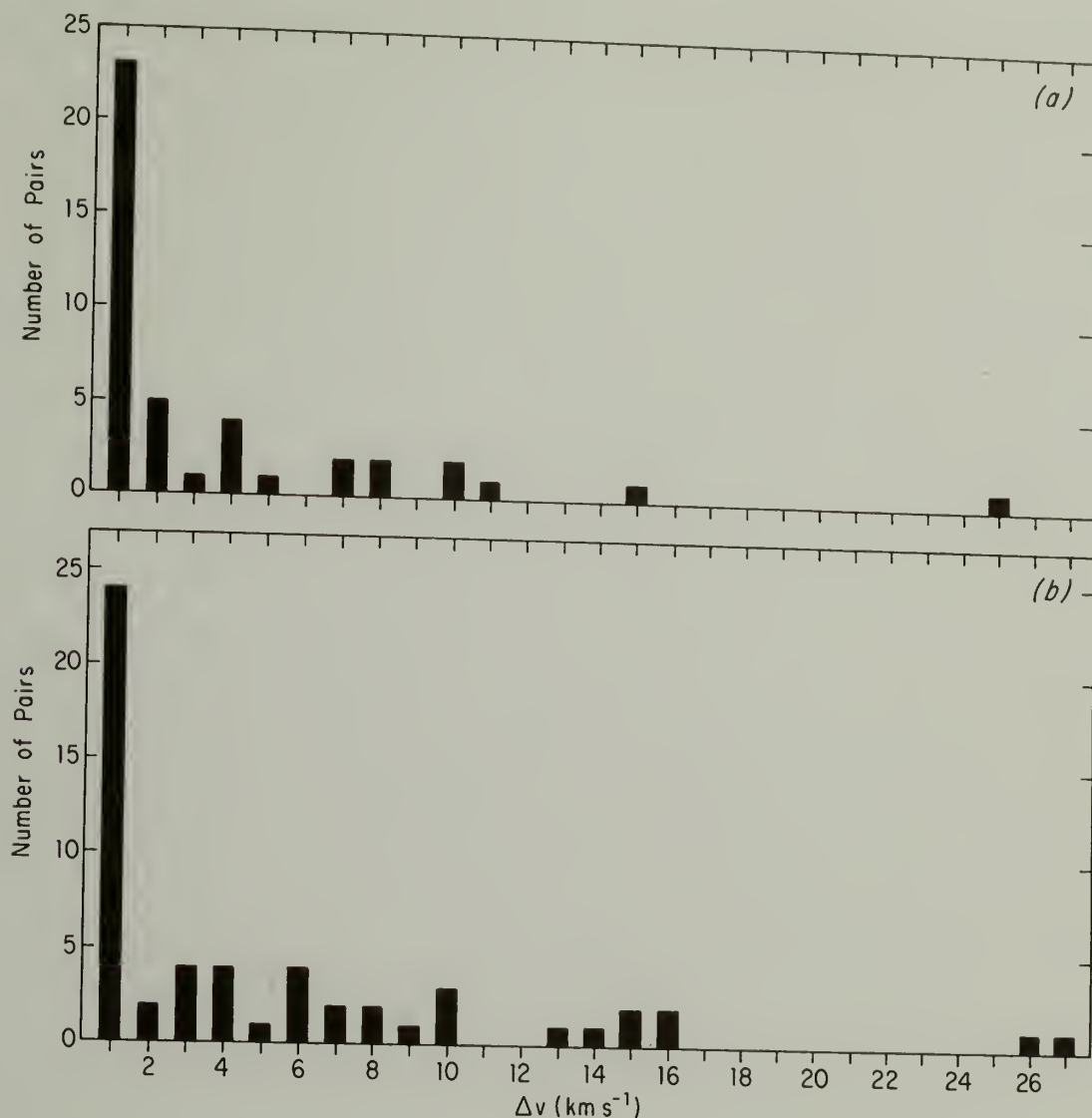


Fig. 36. (a) The number of pairs of H₂O maser velocity features as a function of their velocity separation. The velocities at all epochs were used, but only features in the same cluster were paired. The intervals on the velocity axis span 1 km s⁻¹ centered on the given velocity. Thus, the count at 1 km s⁻¹ includes all separations between 0.5 and 1.5 km s⁻¹. Features at the same epoch in the same cluster whose velocity separation was less than 0.5 km s⁻¹ would not have been resolved. Features at different epochs with a velocity separation of less than 0.5 km s⁻¹ were considered to be the same feature which had drifted in velocity.

(b) Only features in the same cluster at the same epoch were paired, but all combinations of velocity separations between such features were counted.

features within a cluster as a function of their velocity separation. The features of the central cluster were omitted because they were heavily blended and would have given excessive weight to velocity separations around 1 and 20 km s^{-1} (the velocity separation of the shell features). I associated the features at different epochs and counted a pair only once even if the pair was observed at several epochs. If a feature at one velocity was replaced by another at a different epoch, that was also counted as a pair. For example, the B8 cluster produced one pair with a velocity separation of 1 km s^{-1} . At any particular epoch, only differences between a feature and its next closest velocity neighbor were counted. Between epochs, only the smallest velocity changes were counted although a change of less than 0.5 km s^{-1} between epochs was interpreted as a velocity drift of a single feature. Within a single epoch, features in the same cluster separated by less than 0.5 km s^{-1} would have been interpreted as a single feature. There were 21 features whose velocity differences fell between 0.5 and 1.5 km s^{-1} , five whose velocity differences fell between 1.5 and 2.5 km s^{-1} , and 14 whose velocity differences fell between 2.5 and 25 km s^{-1} .

As an alternative analysis, I considered each cluster at each epoch as a single sample (Figure 36(b)). I calculated the velocity difference between each feature in a cluster and every other feature in that cluster. For example, in 1972 the A15 cluster had features at 0.0, 15.0, and 15.6 km s^{-1} . This gave differences of 15.0, 15.6 and 0.6 km s^{-1} . As can be seen by the example, this technique emphasizes

the larger velocity separations which were missed by the first analysis where only the differences between adjacent velocity features were counted. No velocity differences between epochs were considered. Thus, the B8 cluster was not counted at all. Even this analysis, which favors larger velocity separations, shows 24 pairs with velocity separations between 0.5 and 1.5 km s^{-1} , two pairs with velocity separations between 1.5 and 2.5 km s^{-1} , four pairs with velocity separations from 3.5 to 4.5 km s^{-1} , and 20 pairs with velocity separations from 4.5 to 27 km s^{-1} . From both analyses I conclude that the velocity separation of 1 km s^{-1} is a fundamental characteristic of water vapor masers. The cause is not well understood. In the following paragraphs I will discuss several non-kinematic causes of the 1 km s^{-1} separation.

The $6_{16} - 5_{23}$ transition of the water vapor molecule has six hyperfine components with velocity separations of 0.4, 0.6, 1.8, 0.6, and 2.4 km s^{-1} for a total spread of 5.8 km s^{-1} (Figure 14). However, the first three lines, i.e., those with velocity separations of 0.4 and 0.6 (and 1.0) km s^{-1} , are 40 times stronger than the other three lines. While the hyperfine splittings are in general agreement with the velocity separations, there is enough variation that a second cause for the 1 km s^{-1} velocity separation must be found.

For Zeeman splitting to produce the 1 km s^{-1} separation of the velocity features, the H_2O masers must have a magnetic field of a kilogauss (Genzel et al. 1979a). This is far greater than the 10 - 100 milligauss field expected in a cloud with a typical maser density of

10^9 cm^{-3} . For the resonant Stark effect, i.e., the interaction of the molecule with the electric field of the intense maser radiation, to produce the 1 km s^{-1} separation, the radiation temperature must be $10^{18} \text{ }^\circ\text{K}$ which is 10^4 times greater than that measured in strong masers (Genzel et al. 1979a). Hence, neither the Zeeman effect nor the resonant Stark effect can explain the 1 km s^{-1} line separation.

Another possible cause of the velocity separation is turbulence within a cluster. Turbulence would produce more features with small velocity separations. The maser velocity pairs with approximately 1 km s^{-1} velocity differences may be hyperfine components whose frequency has been slightly shifted by turbulence. It is more difficult, but not impossible, for turbulence to explain the larger velocity differences because of the large energy dissipation. Perhaps the features with large velocity separations occur in different parts of an expanding shell of gas about a protostar. I will discuss expanding shells of gas about protostars later in this section.

The velocity widths (Tables 5 through 10) determined from the fringe rates indicate that most strong features are accompanied by weak emission over several km s^{-1} from the same cluster. This may be the H_2O equivalent of the SiO pedestals of Snyder et al. (1978).

The only evidence for a correlated velocity shift is that of the two features near 28 km s^{-1} which changed by 0.7 km s^{-1} in velocity but maintained a separation of 1 km s^{-1} . The phenomena has not been reported before. It suggests that the lines are hyperfine components of a single cloud moving at 20 km s^{-1} relative to the average

maser velocity. The cloud is being slowed by the ambient medium. It would be most interesting to find other such pairs of features, compare their separation to the hyperfine splitting, and see if the clouds are always being decelerated, or if acceleration also occurs.

My observations aid in answering the question, "How many stars are forming in the Kleinmann-Low nebula?" For water vapor data, the question is equivalent to asking how the masers are grouped. If each velocity feature is a separate protostar, then approximately 30 stars are forming in the Kleinmann-Low nebula. If Orion is a typical star formation site, extrapolation of its 30 protostars to the entire galaxy indicates that more stars are forming than are observed. Therefore, the smallest grouping which may correspond to an individual protostar is probably a cluster. If each cluster is pumped by its own protostar, then at least 13 stars are forming in the Kleinmann-Low nebula. If the IR sources are included, the minimum number rises to 15. This is slightly larger than the average number of stars in a subgroup of an OB association (Blaauw 1964).

There is no observational evidence, other than spatial proximity, that any of the clusters are related. Some investigators have grouped a few of the clusters together. Genzel and Downes (1977a), having produced a single telescope map of Orion (Figure 19), grouped the maser in the southwest into two centers of activity, A and B. My VLBI observations have shown that the shell features, which they include in source A, are actually associated with IRC2. However, my composite VLBI map (Figures 27 and 28) shows that the southwest masers could be

grouped into two rings near the positions of source A and B. Figure 28 shows more detail, but the rings are more apparent in the southwest box in Figure 27. The diameter of the A ring is about 2000 a.u., and the diameter of the B ring is about 1000 a.u. Although the southwest masers could be divided into two centers of activity, I find it as reasonable to group them all into one center of activity 5000 a.u. in diameter. This is the size predicted for a dust cocoon about a B0 ($12 M_{\odot}$) star. If the various clusters in the southwest are in a shell about a single star, then the velocity of the individual masers in a cluster must be due to turbulence. The energy which would be dissipated in turbulence in a cluster is at the limit of the energy which could be supplied by the wind and radiation from a B star at the center of the southwest masers. The northeast clusters, NE11, NE4, and NE6, are within 5000 a.u. of one another and could also be associated with a single B0 protostar. The diameter of the entire maser region, i.e., 20 000 a.u., is about the size predicted for a dust cocoon about an O8 ($20 M_{\odot}$) star (Yorke and Krugel 1977).

I propose that Orion A shows four types of H_2O masers which are associated with star formation. The first type is the strong isolated feature seen in the northeast (NE11, NE4, NE6 and perhaps NW3). The second type of maser is the more variable and not too intense maser found in the southwest. Although the individual features in the second type of cluster come and go, the clusters themselves remain. The third type of maser is the high velocity feature. These three maser types are related by the following evolutionary pattern. (See, for example,

Mezger 1978 and Yorke and Krugel 1977.) A $20 M_{\odot}$ protostellar cloud with a radius of 60 000 a.u. initially contracts smoothly. A central core develops and forms a main sequence B0 ($12 M_{\odot}$) star while the surrounding gas continues to fall onto it. A dust bound ionization front forms within 2 a.u. of the core. All the grains inside the front are destroyed. The dust cocoon outside the ionized region will absorb all the stellar radiation and reemit the energy in the infrared. Radiation pressure acts on the grains, and at 3000 a.u. this pressure will stop the infall of the grains. This determines the final mass of the star. The density in the outer dust cocoon may reach 10^7 cm^{-3} , while the density inside it will range from 10^9 cm^{-3} a few astronomical units from the star to 10^5 cm^{-3} just before the second dust cocoon. The temperature throughout the region could be as high as 1000°K . At some positions in the shell, conditions will be suitable for H_2O masers. Velocity gradients in the gas flow will be small allowing long gain paths for maser amplification. The paths would be long-lasting because the gas flow is smooth. Such conditions would produce the strong, long-lasting masers of the first type.

About 10^6 years after the B0 star has formed, the compact HII region begins to expand into the dust shell. The ionization front of the expanding HII region is preceded by a shock front. Between the shock and ionization fronts conditions are again suitable for H_2O masers. However, one can envision how the interaction of the shock with high density inhomogeneities in the cloud would create a chaotic pattern in the gas flow. The path length for maser amplification would be short, and the flux of the masers, small. Furthermore, the

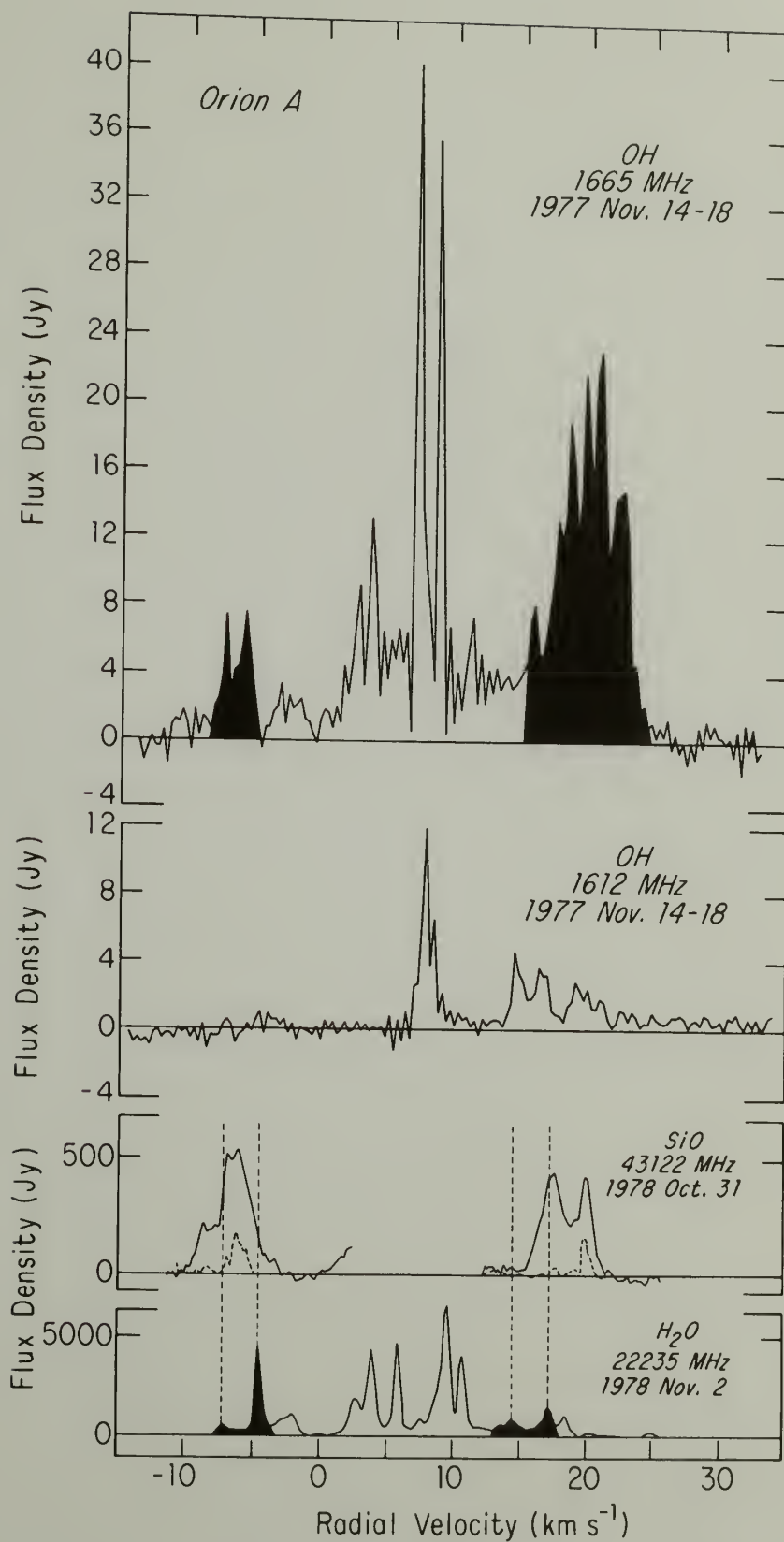
path lengths would change in short periods of time causing the masers to vary rapidly. Masers in such a region would belong to the class of less intense, rapidly varying masers. After another 30 000 years the ionization front will reach the edge of the protostellar cloud creating an optical HII region. The low velocity masers will disappear, but a stellar wind from the newly formed star may accelerate dense neutral clumps from the original cloud to large velocities to create the high velocity H₂O masers. The BN object is possibly such a newly formed star. It has a super compact HII region (Hall et al. 1978) and no masers within several thousand astronomical units of it. It is centered on the high velocity H₂O masers (Genzel et al. 1977a) and is as likely a source for them as any other object in the field.

The fourth type of H₂O maser is the "field" maser. The entire region approximately 1' in size has an inverted water vapor population. The cause of the inversion is the infrared emission from the Kleinmann-Low nebula. Where the projected velocity gradient is small, one sees weak maser emission. Examples of this are the 20 km s⁻¹ emission in the southeast corner, the 13 and 15 km s⁻¹ emission to the far north, the 0.6 km s⁻¹ feature in the west, and the occasional features which appear between the shell and the northeast masers. It is not clear if the missing 2.4 and 3.7 km s⁻¹ masers of Moran et al. (1973) were "field" masers or a third concentration similar to the northeast and southwest concentrations. The field masers may blend into the weak high velocity features which lie farther from the strong masers. A base of emission formed by weak field masers may underlie the entire H₂O spectrum.

In addition to the four classes of H_2O masers associated with star formation, I find a fifth class of H_2O maser in Orion. This class is composed of the "shell" features, which have velocities from -7 to -3 km s^{-1} and from $+15$ to $+18 \text{ km s}^{-1}$. While the diameter of the star formation masers is one a.u., the diameter of the shell features is 10 to 60 a.u. Furthermore, the shell masers vary much less rapidly in intensity than the other masers. Finally, each shell spectral peak consists of many features spread over approximately 3 km s^{-1} . All the features of both peaks are within 1000 a.u. of one another.

The discovery that the masers near -5 and $+17 \text{ km s}^{-1}$ are larger and more stable than the other H_2O masers in Orion is very exciting because it is these features which one would like to associate with a shell of gas about a star. There are similar features near these velocities in the OH and SiO spectra (Figure 37). The two sigma error bars for the 1665 MHz OH shell features from 17.6 to 23.7 km s^{-1} (Raimond and Eliasson 1969) cover the position of the H_2O shell features. My observations (see Chapter IV) show that the OH features from -8 to -5 and $+15$ to $+23 \text{ km s}^{-1}$ are larger, less variable in intensity, and less polarized than the other OH masers seen at 1665 MHz. All the Orion SiO masers are at the shell feature velocities. The SiO maser positions (Moran et al. 1977) are within $2''$ of the H_2O masers, and our 1978 November VLBI experiment (Genzel et al. 1979b) showed that the two SiO spectral peaks were coincident. The compact infrared source, IRC2 (Rieke, Low, and Kleinmann 1973), is coincident with the shell masers and may be the pump.

Fig. 37. The shell features in the spectra of H_2O , OH, and SiO for Orion A. The shaded H_2O features are from the shell position. The shaded OH features were so large that they were not detected in my 1976 VLBI experiment.



The spatial and velocity agreement between shell H_2O , OH and SiO masers leads one to associate them. The most reasonable explanation is that they come from an expanding shell of gas about a star. This shell structure in the spectrum is more typical of an evolved star than a protostar. (Protostars usually have a large number of narrow H_2O features spaced randomly over a 30 km s^{-1} velocity range.) More significantly, the SiO masers in Orion are the only ones not clearly associated with an evolved star. Genzel *et al.* (1980), in a very sensitive search for SiO masers in 27 regions of star formation (e.g., W3(OH), W49N, W51N), found nothing. In 21 of these sources they could have detected emission as strong as the Orion SiO emission. Thus, my observations of the H_2O masers, OH masers, and SiO masers, when coupled with other observations, make a very compelling case for an evolved star in the Kleinmann-Low nebula.

An evolved star in the Kleinmann-Low nebula would be most unusual. Even the optical nebula contains no evolved stars. Furthermore, the characteristics of the Orion object do not exactly match those of other evolved stars. The 22 km s^{-1} separation of the SiO peaks is the widest known. The OH peaks are also widely ($>20 \text{ km s}^{-1}$) spaced. The similar velocity separation for the H_2O , OH and SiO spectral peaks is not expected in a gas whose velocity increases with radius. However, the SiO emission arises close to the star where the velocity of the gas may be controlled by shocks (e.g., Wilson and Hill 1979). No long term variability in the IR like that associated with Mira variables has been seen. None of these objections are so

strong that one can rule out a Mira variable however. The six known supergiants with OH/H₂O masers differ markedly from the Kleinmann-Low source. The supergiants do not have a symmetrical SiO spectrum but they do have strong, unpolarized 1612 MHz OH emission with peaks separated by 50 km s⁻¹. All these arguments against associating the shell features with an evolved star are only quantitative while nothing even qualitatively like the shell source is seen in other regions of star formation. I conclude that the shell features in Orion are associated with an evolved star or some unique object which is not found in other regions of star formation. This is the same conclusion reached by Genzel et al. (1980).

On the basis of my VLBI observations, little can be said about the time variations of the Orion A masers. The transverse motion which I set out to find was not definitely observed. There was some evidence for it in the A6 cluster. Hence, the transverse velocities of the masers are probably less than or equal to the radial velocity dispersion of the masers, a not unexpected result. A more restrictive limit on the transverse motion would require that the maser conditions exist at a particular point in space and that the radial velocity is caused by gas flow at that position. Detection of transverse motion would imply that the maser is a cloud of gas in translational motion. The failure to detect very high transverse motion assures us that the features are not high velocity features with most of their velocity across the line of sight, but a large amplification path along the line of sight. No clear correlations were seen in the amplitude

variations of the maser features. The time variations given in Section 3.2 are a collection of curiosities.

The data in this chapter reveals some interesting hints into the nature of maser regions. However, to better understand the time variability of water vapor masers in Orion we must know their positions to a few milliarcseconds in right ascension and declination. At the distance of the Orion nebula, 10 milliarcseconds corresponds to 5 a.u., the approximate size of a water vapor maser. Ten milliarcsecond accuracy is possible with relative phase mapping if we can (1) overcome the problems of multiple sources in a velocity channel, (2) determine the clock errors at the stations to 50 nanoseconds, and (3) remove the 2π ambiguities in the phase. The telescopes should have an east-west and north-south spacing of 20 to 1000 km. To distinguish transverse motion of a maser from the random appearance and disappearance of separate masers, several observations must be made during the few months time scale over which masers vary. Thus, Orion should be observed once a month for two years. There is still much work to do before the water vapor masers in Orion are understood.

C H A P T E R I V

THE HYDROXYL MASERS

4.1 VLBI Observations

THE HYDROXYL MASERS IN THE ORION NEBULA

S. S. HANSEN

National Radio Astronomy Observatory,* Charlottesville, Virginia; and University of Massachusetts, Amherst

J. M. MORAN AND M. J. REID

Center for Astrophysics, Harvard College Observatory and Smithsonian Astrophysical Observatory

K. J. JOHNSTON AND J. H. SPENCER

E. O. Hulburt Center for Space Research, Naval Research Laboratory, Washington

AND

R. C. WALKER

Department of Physics and Research Laboratory of Electronics, Massachusetts Institute of Technology

Received 1977 August 15; accepted 1977 September 13

ABSTRACT

The 1665 MHz hydroxyl maser emission from the Orion Nebula was observed with very long baseline interferometers sensitive to structure between $0''.5$ and $0''.005$. Most of the maser components were resolved on all baselines and had apparent angular sizes larger than $0''.2$. Maser components at 3.8, 7.1, and 8.6 km s⁻¹ were detected near the position $\alpha = 05^{\text{h}}32^{\text{m}}46^{\text{s}}.85 \pm 0''.1$ and $\delta = -5^{\circ}24'29'' \pm 5''$. These masers were approximately 12'' south of the Becklin-Neugebauer IR object and in the vicinity of the southern water and methanol masers. They were clustered within 1'' of each other and had apparent sizes of about $0''.05$. The 8.6 and 7.1 km s⁻¹ features were spatially coincident and were circularly polarized in opposite senses, suggesting that they may be Zeeman components.

Subject headings: interferometry — masers — interstellar: molecules — nebulae: Orion Nebula — Zeeman effect

I. INTRODUCTION

The Orion Nebula contains the most thoroughly studied molecular cloud in the Galaxy. It is about 500 pc from the Sun and contains most known interstellar molecules. However, by galactic standards its hydroxyl (OH) maser emission is weak, and had not been observed previously with very long baseline interferometers (VLBI). We report the results of a VLBI experiment in which we observed the maser emission in the $F = 1 \rightarrow 1$ transition of the ground state of OH at 1665.401 MHz. The observations are described in § II; and the positions, sizes, and polarizations of the maser components are given in § III. In § IV we discuss the relationship of the OH masers to the other molecular masers and infrared sources in Ori A.

II. OBSERVATIONS AND DATA REDUCTION

The observations were conducted on 1976 May 27 as part of an eight-station VLBI network experiment. The five telescopes from which data were used were the 43 m telescope of the National Radio Astronomy Observatory (NRAO) in Green Bank, West Virginia; the 26 m telescope of the Naval Research Laboratory (NRL) at Maryland Point, Maryland; the 40 m telescope of the California Institute of Technology (OVRO) at Big

Pine; the 26 m telescope of the University of California in Hat Creek; and the 26 m telescope of the Harvard Radio Astronomy Station (HRAS) at Fort Davis, Texas. Other stations in the network were not used either because their sensitivity was too low or because the baselines they formed were too long.

The minimum fringe spacings of the interferometer pairs were $0''.16$ for NRAO-NRL, $0''.077$ for OVRO-Hat Creek, $0''.024$ for OVRO-HRAS, and $0''.011$ for OVRO-NRAO. The shortest projected baseline was achieved with the NRAO-NRL interferometer giving a fringe spacing of $0''.33$. All interferometer observations were made in linear polarization with the E -field vector aligned north-south. The 1665 MHz OH emission from Ori A shows little, if any, linear polarization (Palmer and Zuckerman 1967). The data on Ori A were taken with a 250 kHz bandwidth which covered LSR velocities from -14 to 31 km s⁻¹. For calibration 3C 120, 3C 84, and other continuum sources were observed with a 2 MHz bandwidth. The local oscillators were held constant at all stations and the data were later shifted in frequency to compensate for the motion of the Earth. All stations except Hat Creek had hydrogen maser frequency standards. Observations were alternated with 15 minutes on Ori A and 5 minutes on 3C 120. The data were recorded with the Mark II VLBI system (Clark 1973).

The data were correlated with the NRAO Mark II VLBI processor in Charlottesville, Virginia. The

* The National Radio Astronomy Observatory is operated by Associated Universities, Inc., under contract with the National Science Foundation.

resulting 144-point total-power and cross-power spectra were uniformly weighted, yielding spectral resolution of 2.1 kHz (0.4 km s^{-1}). The fringe amplitudes, rates, and phases for each spectral channel were analyzed to yield positions and fringe visibilities for the individual maser features (Moran 1973).

On 1977 April 2, Ori A was observed with the NRAO 43 m telescope to determine the circular polarization of the maser components detected in the VLBI experiment. The velocity resolution for these observations was 0.35 km s^{-1} .

III. RESULTS

a) Structure

The total power spectra for Ori A in right and left circular polarization from 1977 April 2 are shown in Figure 1. We detected fringes during the VLBI experiment from the features at 3.8, 7.1, and 8.6 km s^{-1} on the NRAO-NRL and OVRO-Hat Creek baselines and on the shorter projections of the OVRO-HRAS baseline. These features were resolved on the OVRO-NRAO baseline. All other features were completely resolved on all baselines, including the $0''.33$ projection the NRAO-NRL baseline. The minimum detectable (3σ) flux density was about 1 Jy ($T_A = 0.25 \text{ K}$ for an unpolarized feature in the scale of Fig. 1). In Table 1 we list the lower limits for the apparent sizes of those maser components not detected, assuming a circular Gaussian brightness distribution.

The fringe visibility of the 8.6 km s^{-1} component decreases as the projected baseline length increases.

TABLE 1
SIZES, FLUX DENSITIES, AND POLARIZATION OF FEATURES IN THE
1665 MHz OH SPECTRUM OF ORION A

Velocity* (km s^{-1})	$\Delta\alpha^\dagger$ (arcsec)	$\Delta\delta^\ddagger$ (arcsec)	Diameter ‡ (AU)	S(1977) (Jy)	Pol. § (percent)
-7.0			>70	7	+30
-5.7			>90	8	+20
+3.8	-0.063 ± 0.002	0.848 ± 0.003	13	16	+40
+7.1	-0.054 ± 0.001	-0.017 ± 0.001	25	44	+60
+7.9				9	-20
+8.6	0	0	25	38	-80
+11.1			>30	8	-30
+15.7			>70	9	-20
+17.8			>70	12	+20
+18.9			>70	19	-20
+19.9			>70	22	0
+20.9			>70	24	+20
+22.6			>70	15	0

* With respect to the LSR and a rest frequency of 1665.401 MHz.

† With respect to the reference position of $\alpha = 05^h32^m46.85^s \delta = -5^\circ24'29''$ (1950). Errors are formal 1σ values.

‡ 1 AU corresponds to $0''.002$ or $1.5 \times 10^{13} \text{ cm}$.

§ Percent circular polarization (+, right; -, left).
Core component.

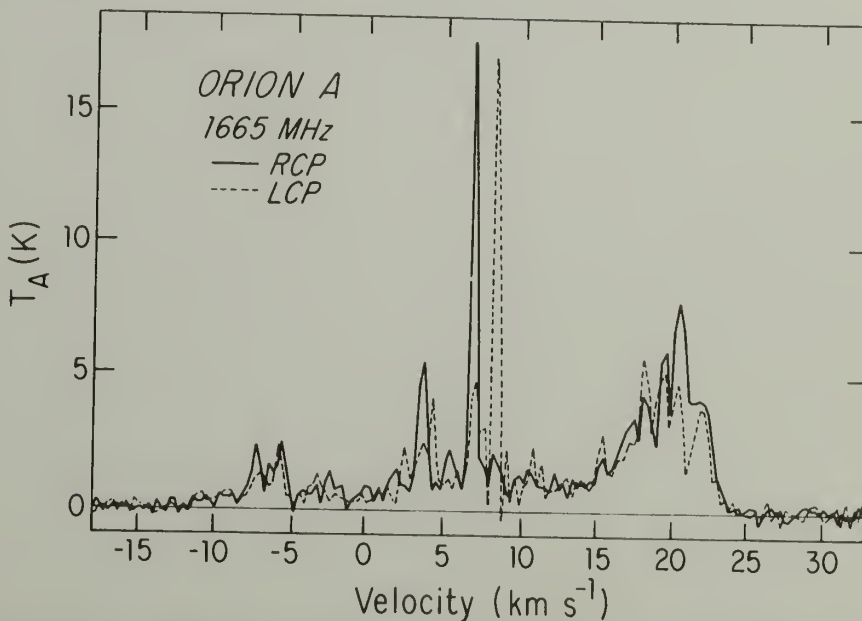


FIG. 1.—Spectra of the $F = 1 \rightarrow 1$ transition in the ground state of OH toward Orion A. The velocity axis refers to the local standard of rest and a transition frequency of 1665.401 MHz. The resolution is 0.35 km s^{-1} . The total flux density in janskys is 1.9 times the sum of the antenna temperature in right circular polarization (solid line) and left circular polarization (dashed line). These uniformly weighted spectra were obtained on 1977 April 2 on the 43 m NRAO antenna and are very similar to those obtained during the VLBI observations.

This component can be modeled as a circular Gaussian with a full width at half-maximum (FWHM) of $0''.045$ (3.5×10^{14} cm or 25 AU). The fringe visibility of the 7.1 km s^{-1} component is more complex; it either has two (or more) components or is elongated. In either case, the major axis of the source has a position angle of 30° (east of north), and the size along this axis is about $0''.05$. The 3.8 km s^{-1} component has a fringe visibility of 0.5 which remained nearly constant on the OVRO-Hat Creek, NRAO-NRL, and OVRO-HRAS baselines. It was not detected on the NRAO-OVRO baseline. This suggests that half of the flux density from these features comes from a component larger than $0''.5$ and half from a component of diameter $\sim 0''.025$.

b) Positions

The absolute position of the 8.6 km s^{-1} maser component was determined by analyzing the fringe rate residuals of this feature and the calibration sources with the NRAO-NRL and OVRO-Hat Creek interferometers. Twenty observations of Orion, 20 of 3C 120, 27 of 3C 84, and 25 of other calibrators on each baseline were used. A model of the density profile of the ionosphere was made from monthly mean ionosonde data obtained at Wallops Island, Virginia. A simple exponential model was used for the wet and dry components of the troposphere. The *a priori* coordinates were accurate to about 2 m on the NRAO-NRL baseline and 5 m on the OVRO-Hat Creek baseline. The positions for the calibrators, accurate to $0''.1$, were taken from Rogers *et al.* (1973). Several least-mean-square analyses were performed. In the simplest, the fringe rate of 3C 120 was subtracted from that of Orion and the position of the maser found from a two-parameter fit. Because of the angular proximity of the two sources, the effects of errors in the atmospheric model and in the baseline were reduced. Also, any drifts in the frequency standards were removed. More complex analyses, using all the available data on the NRAO-NRL baseline, were performed to estimate up to six parameters (two source coordinates of Orion, two equatorial baseline components, a zenith propagation path length, and a local oscillator frequency offset). The formal errors in right ascension and declination were typically $0''.5$ and $3''$, respectively, and the mean baseline coordinates were found to be $B_x = 223750 \pm 1$ and $B_y = -40574 \pm 1$ m. These solutions allowed us to make a critical evaluation of systematic effects in the data and led to a more conservative estimate of the source coordinate errors. The best position for the 8.6 km s^{-1} feature is

$$\begin{aligned}\alpha &= 05^{\text{h}}32^{\text{m}}46^{\text{s}}85 \pm 0^{\text{s}}1, \\ \delta &= -5^{\circ}24'29'' \pm 5'' \quad (1950.0).\end{aligned}$$

The errors are 1σ values which include an allowance for systematic effects. The larger error in declination is due largely to the poorer sensitivity of the fringe rate data on low declination sources. This position is slightly different from the preliminary results reported at the 150th meeting of the AAS (Hansen *et al.* 1977).

The OH masers we detected are approximately $12''$ south of the Becklin-Neugebauer infrared source, and in the vicinity of the infrared source IRC 4 and the southern H_2O and CH_3OH masers (see Fig. 2). They are significantly displaced from the OH maser components in the velocity ranges of 4.0 to 4.5 and 17.6 to 23.7 km s^{-1} but close to those in the range 6.8 to 7.9 km s^{-1} detected by Raimond and Eliasson (1969). Raimond and Eliasson used the Owens Valley interferometer with a baseline of 1600 feet (500 m) and detected those maser components which we have completely resolved. Thus it appears that there are at least two regions of OH maser activity in Ori A.

The relative positions of the 3.8 , 7.1 , and 8.6 km s^{-1} maser components were determined by examining their relative fringe phases. Relative positions determined in this manner are not sensitive to instabilities in frequency standards, atmospheric propagation effects, or baseline errors (cf. Reid *et al.* 1977). The displacements of the 7.1 and 3.8 km s^{-1} components are given in Table 1.

c) Time Variations

Spectra of the OH maser in Orion for the period from 1965 to 1975 have been published by Palmer and Zuckerman (1967), Menon (1967), Weaver, Dieter, and Williams (1968), Manchester, Robinson, and Goss (1970), Chaisson and Beichman (1975), and others. With the exception of the 3.8 , 7.1 , and 8.6 km s^{-1} features, the OH spectrum we observed in 1976 and 1977 (Fig. 1) is very similar to the previous spectra. Thus there appear to be no dramatic changes in the maser features which we completely resolved with our interferometers. However, the three components which were compact enough to be detected in our VLBI experiment are difficult to identify in OH spectra before 1973. Hence these components appear to be new maser features.

IV. CONCLUSIONS

The features at 3.8 , 7.1 , and 8.6 km s^{-1} are the smallest, most polarized, and most variable of all OH maser components in Ori A. These components are not associated with the Becklin-Neugebauer object or with the northern OH maser components detected by Raimond and Eliasson (1969). They appear to be associated with the southern H_2O and CH_3OH masers and possibly with one of the infrared sources in the Kleinmann-Low nebula. The position is about $3''$ southeast of the $\text{H}_2\text{O}/\text{SiO}$ source with features at -6 and $+16 \text{ km s}^{-1}$ identified by Moran *et al.* (1977) and Genzel and Downes (1977), and the OH masers are possibly part of this object.

It is interesting to note that the cluster of three components we have observed has a projected diameter of only 400 AU. Thus the possibility that they originate in the infalling envelope of a newly forming $4 M_\odot$ star cannot be ruled out.

The Zeeman pattern expected for the 1665 MHz OH transition for a longitudinal magnetic field consists of a pair of components of equal line strength, having opposite senses of circular polarization, and sepa-

rated by $0.59 \text{ km s}^{-1} \text{ milligauss}^{-1}$. Beichman and Chaisson (1974) and Chaisson and Beichman (1975) suggested that the 8.6 and 7.1 km s^{-1} features could be such a Zeeman pair. This suggestion was based in part upon their identification of the more complex Zeeman pattern for the 1612 MHz OH transition centered at nearly the same velocity in Orion. Our observations show that the 8.6 and 7.1 km s^{-1} components are separated in the sky by a distance of about $0''.06$, which is about equal to their apparent angular diameters. Since the true sizes of maser clouds are

generally thought to be much larger than their apparent sizes, it seems quite reasonable that we are seeing the two Zeeman components coming from a cloud having a velocity of 7.9 km s^{-1} and longitudinal magnetic field of 2.5 milligauss . Small velocity and magnetic field gradients could account for the slight separation of the images we observed.

We thank D. C. Backer, J. Romney, and P. Crane for help with the data acquisition at Hat Creek, Owens Valley, and NRAO, respectively.

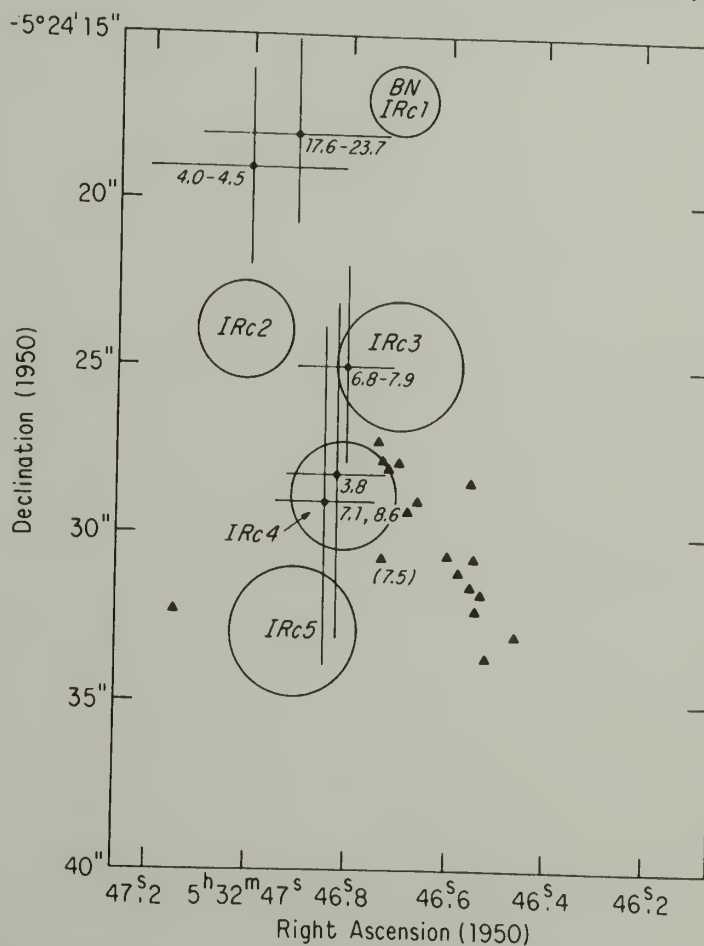


FIG. 2.—The OH masers (filled circles) and some of the H_2O masers (filled triangles) as measured by Genzel and Downes (1977) in the vicinity of the Becklin-Neugebauer (BN) object and the other infrared sources (IRc 2–5) of the Kleinmann-Low nebula (Reike, Low, and Kleinmann 1973). There are additional H_2O masers outside the area of this map. The OH features at 17.6 – 23.7 , 4.0 – 4.5 , and 6.8 – 7.9 km s^{-1} are from Raimond and Eliasson (1969); the 3.8 , 7.1 , and 8.6 positions are from this paper. The error bars on the OH positions are 1σ values; the 1σ errors on the H_2O positions are about $2''$.

REFERENCES

- Beichman, C. A., and Chaisson, E. J. 1974, *Ap. J. (Letters)*, **190**, L21.
 Chaisson, E. J., and Beichman, C. A. 1975, *Ap. J. (Letters)*, **199**, L39.
 Clark, B. G. 1973, *Proc. IEEE*, **61**, 1242.
 Genzel, R., and Downes, D. 1977, *Astr. Ap.*, in press.
 Hansen, S. S., Moran, J. M., Reid, M. J., Johnston, K. J., Spencer, J. H., and Walker, R. C. 1977, *Bull. AAS*, **9**, 303.

No. 2, 1977

HYDROXYL MASERS IN ORION

L69

- Manchester, R. N., Robinson, B. J., and Goss, W. M. 1970, *Australian J. Phys.*, **23**, 751.
- Menon, T. K. 1967, *Ap. J. (Letters)*, **150**, L167.
- Moran, J. M. 1973, *Proc. IEEE*, **61**, 1236.
- Moran, J. M., Johnston, K. J., Spencer, J. H., and Schwartz, P. R. 1977, *Ap. J.*, **217**, 420.
- Palmer, P., and Zuckerman, B. 1967, *Ap. J.*, **148**, 727.
- Raimond, E., and Eliasson, B. 1969, *Ap. J.*, **155**, 817.
- Reid, M. J., Muhleman, D. O., Moran, J. M., Johnston, K. J., and Schwartz, P. R. 1977, *Ap. J.*, **214**, 60.
- Reike, G. H., Low, F. J., and Kleinmann, D. E. 1973, *Ap. J. (Letters)*, **186**, L7.
- Rogers, A. E. E., Counselman, C. C., Hinteregger, H. F., Knight, C. A., Robertson, D. S., Shapiro, I. I., Whitney, A. R., and Clark, T. A. 1973, *Ap. J.*, **186**, 801.
- Weaver, H., Dieter, N. H., and Williams, D. R. W. 1968, *Ap. J. Suppl.*, **16**, 219.

- S. S. HANSEN and M. J. REID: National Radio Astronomy Observatory, Edgemont Road, Charlottesville, VA 22901
- K. J. JOHNSTON and J. H. SPENCER: Naval Research Laboratory, Code 7132, Washington, DC 20375
- J. M. MORAN: Center for Astrophysics, 60 Garden Street, Cambridge, MA 02138
- R. C. WALKER: Owens Valley Radio Observatory, California Institute of Technology, Pasadena, CA 91125

4.2 The Magnetic Fields

THE MAGNETIC FIELDS IN ORION A AS DERIVED FROM HYDROXYL MASER RADIATION

S. S. Hansen

University of Massachusetts, Amherst

and

National Radio Astronomy Observatory, Charlottesville, Virginia

ABSTRACT

Orion A was observed in the four hyperfine transitions of OH in the ${}^2\Pi_{3/2}$ $J = 3/2$ state. The circularly polarized radiation at 1612 MHz exhibits a Zeeman pattern centered at 8.02 km s^{-1} . The frequency separation of the four observed lines, i.e., the $\sigma^{\pm 1}$ and $\sigma^{\pm 2}$ lines, is in excellent agreement with the Zeeman splitting produced by a four milligauss field. The amplitude ratio of the four lines is within a factor of two of that predicted for a partially saturated maser. The $\sigma^{\pm 3}$ circularly polarized Zeeman components are suppressed by the $\sigma^{\mp 1}$ components.

4.2.1 Introduction

Magnetic fields have a major role in star formation (e.g., Mouschovias 1976). The strength of these fields is the subject of much discussion. The magnetic field in the interstellar medium determined from the rotation of the plane of polarization of pulsar radiation is typically 2 microgauss (Manchester and Taylor 1977). In maser sources the field can be determined by the Zeeman splitting of

the OH spectrum. That field is typically 3 milligauss. I will review in some detail the spectrum of the OH molecule following Herzberg (1950). The OH radical has one unpaired electron. The projection, Λ , of the electronic orbital angular momentum, L , onto the internuclear axis, is represented by Σ, Π, Δ , etc., for $\Lambda = 0, 1, 2$, etc. The ground state is a Π state. The spin of the electron, S , has a projection along the internuclear axis of Σ . The sum of Σ and Λ is represented by Ω . The rotation of the molecule is denoted by N and total angular momentum by $J = N + \Omega$. The ground state of the molecule is denoted by

$${}^2\Pi_{3/2} \quad J = 3/2$$

where the superscript is $2S + 1$ and the subscript is Ω . Note that in the ground state of OH, $\Omega = 3/2$ rather than $\Omega = 1/2$.

The energy states for positive and negative values of Λ would normally be degenerate. However, interactions between the electron angular momentum and the rotation of the molecule split the energy levels. This phenomena is known as Λ doubling. Each of these two Λ levels has two hyperfine levels, $F = J \pm 1/2$, due to the interaction of the total angular momentum with the spin of the hydrogen nucleus. The four states and the frequencies of the transitions between them are shown in Figure 38(a).

If the molecule is in a magnetic field, then each projection of F onto the field will have a slightly different energy. The projection is denoted by m_F and may have integer values from $-F$ to $+F$. The

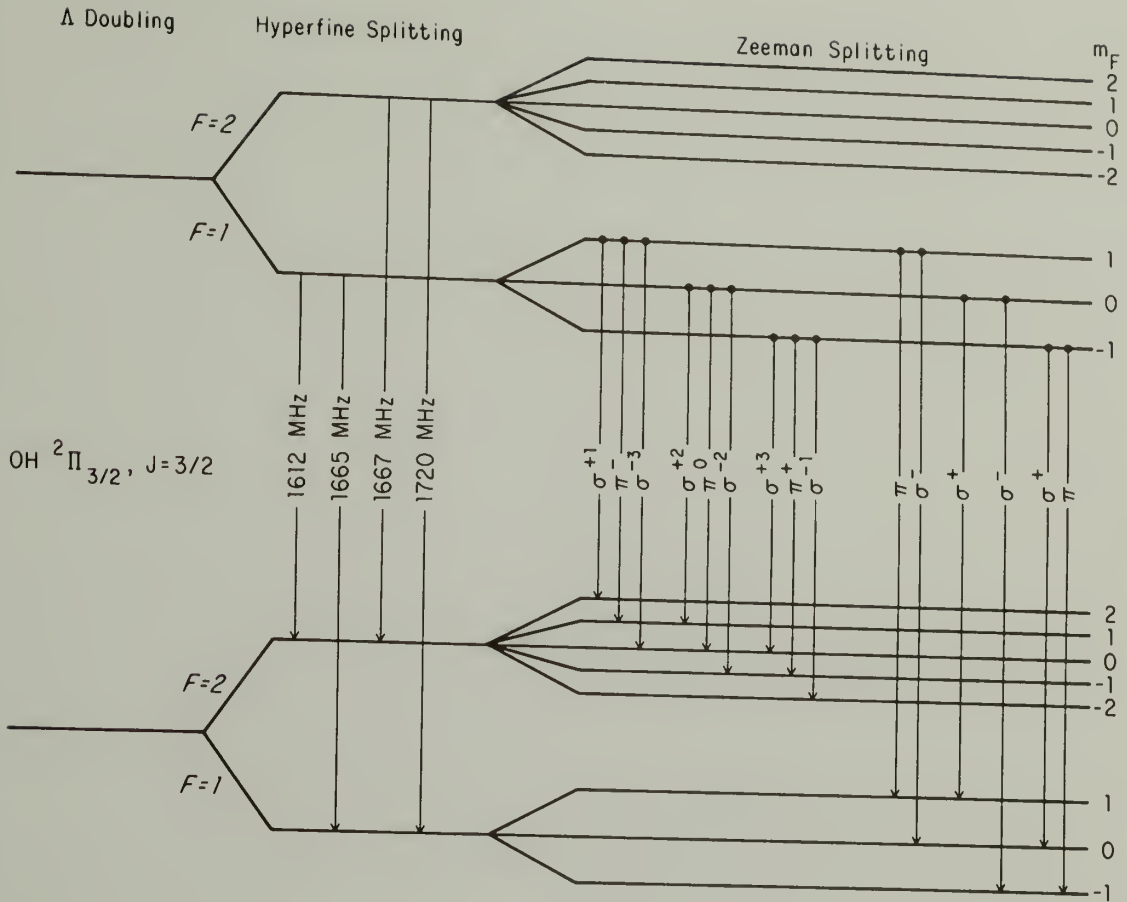


Fig. 38. (a) The energy levels of the hydroxyl radical in its ground state. In the absence of a magnetic field there are four hyperfine transitions at 1612, 1665, 1667 and 1720 MHz with relative intensities of 1:5:9:1 in thermodynamic equilibrium. The permitted Zeeman transitions at 1612 and 1665 MHz are indicated. If the field is parallel to the line of sight, the σ^+ components ($\Delta m_F = m_{F\text{lower}} - m_{F\text{upper}} = +1$) are left circularly polarized, and the σ^- components ($\Delta m_F = -1$) are right circularly polarized. Note that by IEEE convention right circular polarization denotes clockwise rotation of the electric vector when viewed along the direction of propagation. No π components ($\Delta m_F = 0$) are emitted parallel to the field. If the magnetic field is perpendicular to the line of sight, the σ components are linearly polarized perpendicular to the field, and the π components are linearly polarized parallel to the field.

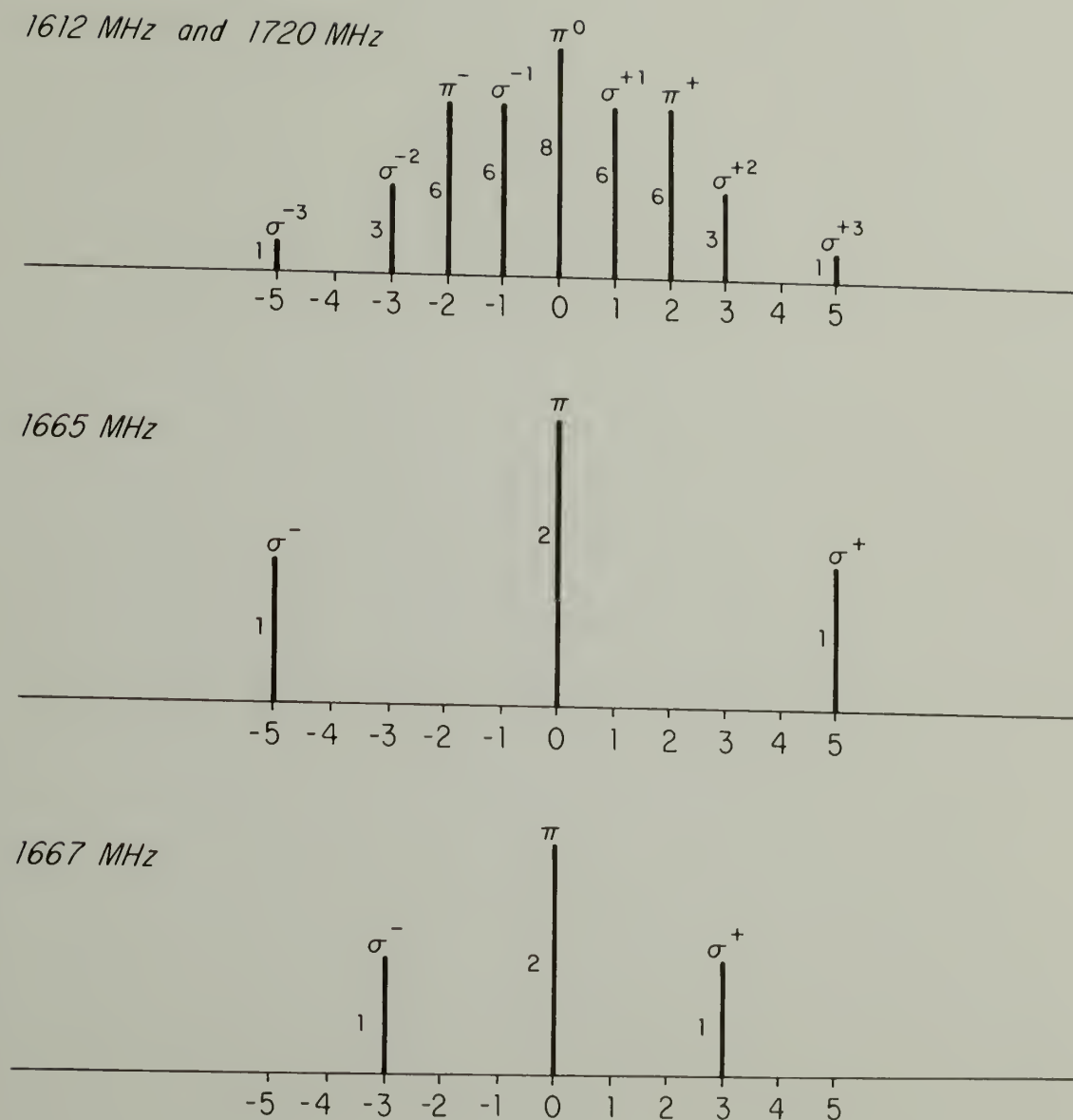


Fig. 38. (b) The Zeeman patterns of the hyperfine transitions of the ground state of OH. The number by each Zeeman component is its relative intensity in that hyperfine transition. The units on the horizontal axis are -652 Hz per milligauss, which is 0.121 km s $^{-1}$ per milligauss at 1612 MHz, 0.117 km s $^{-1}$ per milligauss at 1665 and 1667 MHz, and 0.114 km s $^{-1}$ per milligauss at 1720 MHz.

splitting of the energy levels by a magnetic field, i.e., the Zeeman splitting, is shown on the left side of Figure 38(a). Only transitions with $\Delta m_F = 0, \pm 1$ are permitted, except that ΔF , m_F and Δm_F cannot all be zero. The transitions for the Zeeman components at 1612 and 1665 MHz are indicated in Figure 38(a), and the frequency and relative intensity of these transitions in Figure 38(b).

Chaisson and Beichman (1975) explain two OH lines at 1665 MHz and six at 1612 MHz in Orion A as the Zeeman pattern of a source moving at 8 km s^{-1} LSR in a 4 milligauss field. They felt it highly improbable that the six lines at 1612 MHz were mere coincidence with the Zeeman σ transition, particularly since the ratio of the intensity of the left and right circularly polarized emission at 1612 MHz was the same as the ratio of the intensity of the Zeeman pair at 1665 MHz. Because the right circularly polarized and left circularly polarized patterns required slightly different field strengths, and because the patterns overlapped, Chaisson and Beichman had to postulate the existence of two clouds whose velocity and field gradients selected only one mode of polarization (Cook 1966). Hansen et al. (1977) found convincing evidence favoring the Zeeman interpretation by showing that the Zeeman pair at 1665 MHz was spatially coincident. Their observations also showed that the amplitude of both lines of the pair at 1665 MHz had increases from 1975 to 1977 and were of equal intensity. If the 1665 MHz Zeeman pair did indeed correspond to the 1612 MHz sextet, then the intensities of the left and right circularly polarized emission at 1612 MHz should be equal and stronger than Chaisson

and Beichman found them in 1975. The spectra had changed but not as anticipated.

4.2.2 Observations. Orion A was observed on the nights of 1977 November 14-18 with the National Radio Astronomy Observatory's 43 m telescope in Green Bank, WV. An IF polarimeter was used with two cooled paramps to simultaneously obtain left and right circularly polarized spectra. Each mode of circular polarization rejected the opposite mode to better than 20 dB. All four transitions were observed with a 312 kHz bandwidth. The 1612 MHz and 1665 MHz transitions were also observed with a 39 kHz bandwidth. The 312 kHz spectra were uniformly weighted for a resolution of 2 kHz (0.35 km s^{-1}). The 39 kHz data were Hanning weighted for a resolution of 400 Hz (0.07 km s^{-1}). The system temperature on cold sky was 60°K , but the continuum radiation from the Orion nebula raised the system temperature to 150°K . An unlocked crystal in the local oscillator chain shifted the spectral lines in the B receiver 700 Hz (0.13 km s^{-1}) higher than in the A receiver. This was corrected in the postprocessing software. The observations were frequency switched at a rate of 1 Hz. Frequency switching held the system temperature constant for the on and off spectra. Because the reference band was only 150 kHz from the signal band and because the bandwidths were narrow, only a constant baseline was removed from the spectra. The errors quoted on the data are theoretical $1 \sigma_{T_{\text{sys}}}$ values and were determined from the formula

$$\sigma_{T_{\text{sys}}} = \frac{\pi T_{\text{sys}}}{\sqrt{\tau \Delta f}}$$

4.1

where T_{sys} is the system temperature, τ is the integration time, Δf is the frequency bandwidth of a channel, and the factor π is the product of: $\pi/2$ from one bit digitation in the correlator (VanVleck and Middleton 1966), $\sqrt{2}$ from spending only half time on the source, and $\sqrt{2}$ from differencing the signals.

The 312 kHz bandwidth total power spectra of the four transitions are shown in Figure 39. The flux density scale was determined by multiplying the antenna temperature by $k A^{-1} = 2 \text{ Jy } ^\circ\text{K}^{-1}$. Observations of 3C 161 determined the conversion factor. The 1667 MHz spectrum is fit well by a broad Gaussian absorption feature and a narrow emission feature; the 1720 MHz spectrum, by a broad, shallow absorption feature. Table 12 gives the values of the parameters of Gaussian line profiles fit to the data. The absence of strong maser emission at 1667 MHz and 1720 MHz was not unexpected because 1667 MHz emission is more often associated with evolved stars than protostars, and 1720 MHz maser emission is seldom observed.

4.2.2.1 1665 MHz. The high resolution spectra for 1665 MHz are shown in Figure 40. Several of the features were not single Gaussians. In these cases two Gaussians were fit to the data to arrive at the values shown in Table 12. Although two Gaussians produce an excellent fit, it is quite possible that expansion, collapse, or rotation of the gas has distorted a single Gaussian line profile. The zero baseline

Fig. 39. The total power spectra of the four hyperfine transitions of the ground state of OH. The velocity axis refers to the local standard of rest. The spectra were uniformly weighted for a velocity resolution of 0.35 km s^{-1} . The flux density was determined by multiplying the antenna temperature for each polarization by $2.0 \text{ Jy } ^\circ\text{K}^{-1}$. The one sigma deviation in flux was 0.35 Jy for 1612 MHz , 0.55 Jy for 1665 MHz , 0.51 Jy for 1667 MHz , and 0.55 Jy for 1720 MHz . The spectra were obtained with the NRAO 43 m telescope on 1977 November 14-18.

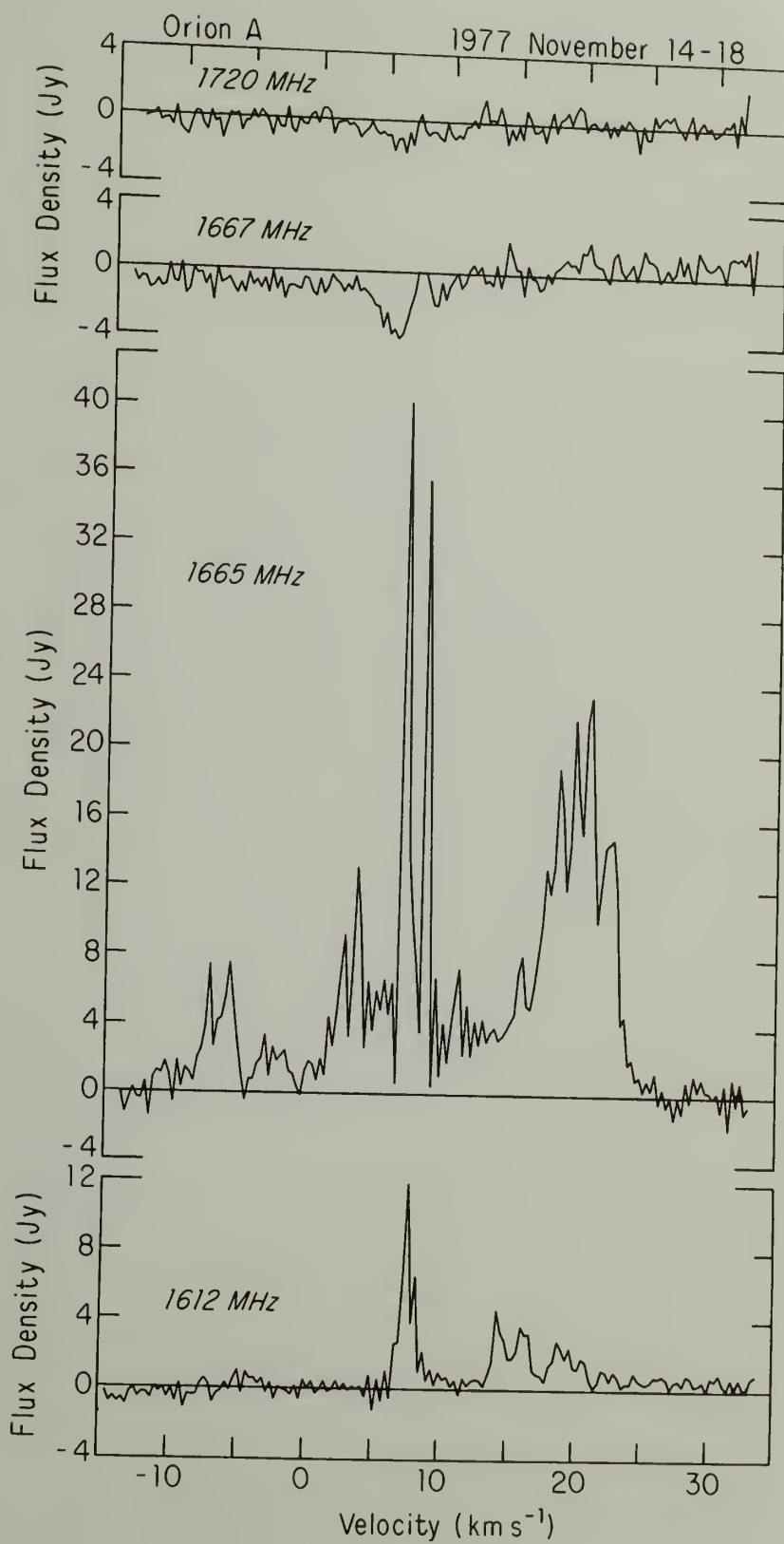


TABLE 12

Orion OH Features 1977 November 14-18

Velocity		Flux		FWHM		Polarization*	
1977	1975-1976	1977	1975-1976	1977	1975-1976	1977	1976
(km s ⁻¹)		(Jy)		(km s ⁻¹)		(%)	
$\Delta v = 0.073 \text{ km s}^{-1}$		1612 MHz $\sigma = 0.22 \text{ Jy}^\dagger$		Time = 46500 s			
	(6.91)	0.0	(0.8)		(0.2)		
7.10	(not given)	1.0	(1.0) [†]	0.44		- 8	
7.28	(7.28)	2.5	(3.0)	0.34		+51	
7.65	(7.64)	4.9	(6.8)	0.32		+24	
7.75	(7.76)	10.1	(4.0)	0.31		+44	
8.25	(8.20)	6.5	(3.8)	0.30		-85	
8.42		0.9		0.30		-55	
8.72	(8.80)	1.0	(1.6)	0.74	(0.3)	-77	
† estimated from published spectra							
$\Delta v = 0.073 \text{ km s}^{-1}$		1665 MHz $\sigma = 0.56 \text{ Jy}^\dagger$		Time = 7200 s			
2.46		7.9		0.66		-100 ?	
3.61	(3.8)	7.2	(16)	0.36		+ 96	(+40)
3.91	(see 3.61)	6.7		0.30		+ 85	
4.46		2.4		0.33		- 82	
	(6.93)		(21.6)		(0.3)		
7.13	(7.1)	34.8	(44)	0.24		+ 73	(+60)
7.21		6.7		0.37		+ 70	
7.24	(see 7.13)	10.0		0.71		+ 66	
7.69	(7.9)	4.3	(9)	0.51		- 13	(-20)
	(8.44)		(36.8)		(0.3)		
8.60	(8.6)	13.8	(38)	0.33		- 86	(-80)
8.71	(see 8.60)	29.5		0.22		- 89	
$\Delta v = 0.35 \text{ km s}^{-1}$		1667 MHz $\sigma = 0.51 \text{ Jy}^\dagger$		Time = 8400 s			
6.3		-3.7		4.81		0	
7.5		+3.1		1.30		0	

Table 12, continued

Velocity		1977	Flux		FWHM		Polarization	
1977	1975-1976		1975-1976	(Jy)	1977	1975-1976	1977	1976
(km s ⁻¹)						(km s ⁻¹)		(%)
$\Delta v = 0.35 \text{ km s}^{-1}$		1720 MHz						Time = 7200 s
		$\sigma = 0.55 \text{ Jy}^\dagger$						
6.1		-0.9			5.75			0

* The polarization is defined as $(\text{RCP}-\text{LCP})/(\text{RCP}+\text{LCP})$. The values are for the channel closest to the velocity of the peak of the fit Gaussian.

† The flux density σ and the integration time for the 1612 MHz and 1665 MHz data are for each polarization. The values for the 1667 MHz and the 1720 MHz data are for the sum of the polarizations.

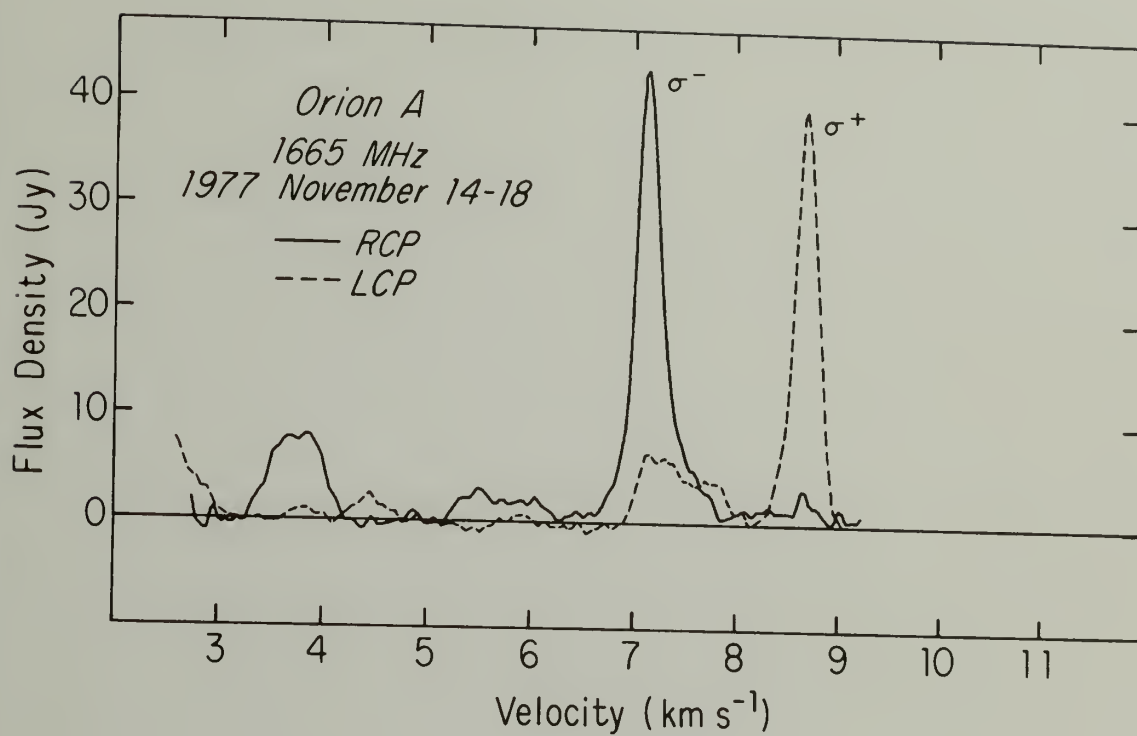


Fig. 40. Right (solid line) and left (dashed line) circularly polarized spectra for the 1665 MHz transition. The data were Hanning weighted for a velocity resolution of 0.073 km s^{-1} . The standard deviation in the flux density is 0.56 Jy.

in the high resolution spectra actually corresponds to an OH polarized flux of about 2 Jy in the 312 kHz bandwidth spectra.

The values in parentheses in the 1665 MHz section of Table 12 are for data taken on 1977 April 2 by Hansen *et al.* (1977) (Section 4.1) with the exception of the 6.93 km s^{-1} and 8.44 km s^{-1} values which came from Chaisson and Beichman (1975). None of the features seen from 1975 through 1977 have changed significantly. Even the three features seen in the VLBI maps (Hansen *et al.* 1977) (3.8 , 7.1 , 8.6 km s^{-1}), which were not detected before 1973, showed only slight variation. The left circularly polarized 4.4 km s^{-1} feature has continued to decline.

The most noticeable change is the new 100% left circularly polarized feature at 2.5 km s^{-1} . It is tempting to claim that this line is a Zeeman companion to the 3.8 km s^{-1} feature. The spacing between the two lines (1.2 km s^{-1}) implies a field of 2 milligauss. The field is in the opposite direction of the 2.5 milligauss field required by the $7.1/8.6 \text{ km s}^{-1}$ pair (Section 4.1). The 3.8 km s^{-1} feature is less than $1''$ (500 a.u. projected) from the $7.1/8.6 \text{ km s}^{-1}$ pair.

4.2.2.2 1612 MHz. The high resolution spectra for 1612 MHz are shown in Figure 41. The values in parentheses in the 1612 MHz section of Table 12 are from 1975 January (Chaisson and Beichman 1975). The intensities of the strongest left and right circularly polarized lines have approximately doubled since 1975. The other lines have decreased slightly in intensity. A Zeeman pattern is not immediately obvious.

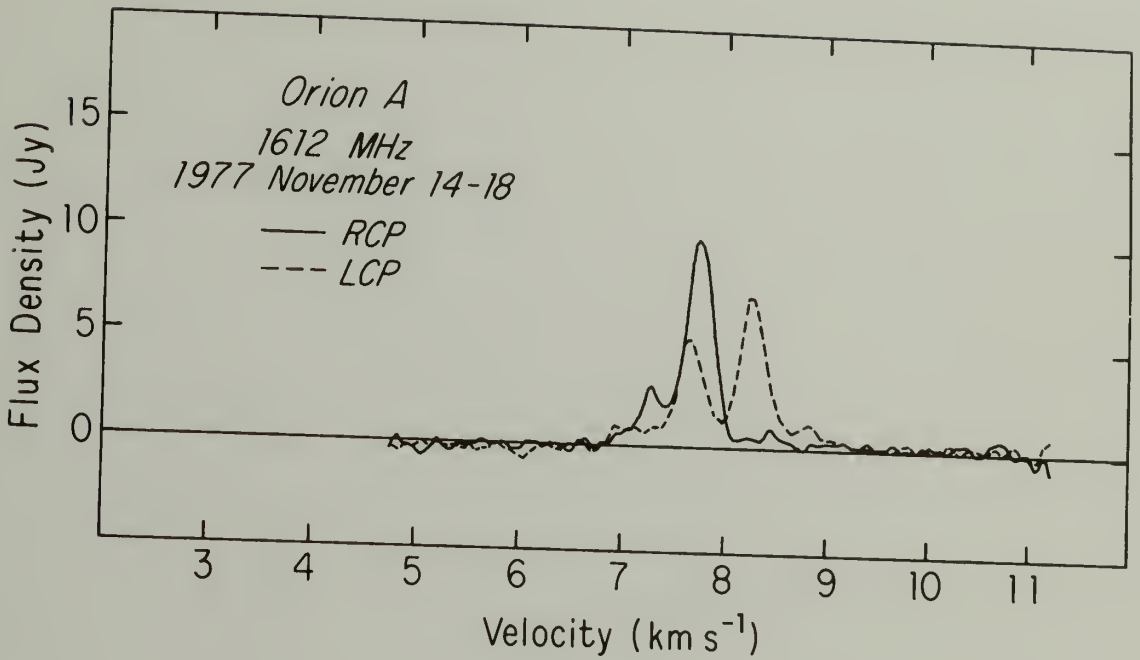


Fig. 41. Right (solid line) and left (dashed line) circularly polarized spectra for the 1612 MHz transition. The data were Hanning weighted for a velocity resolution of 0.073 km s^{-1} . The standard deviation in the flux density is 0.22 Jy .

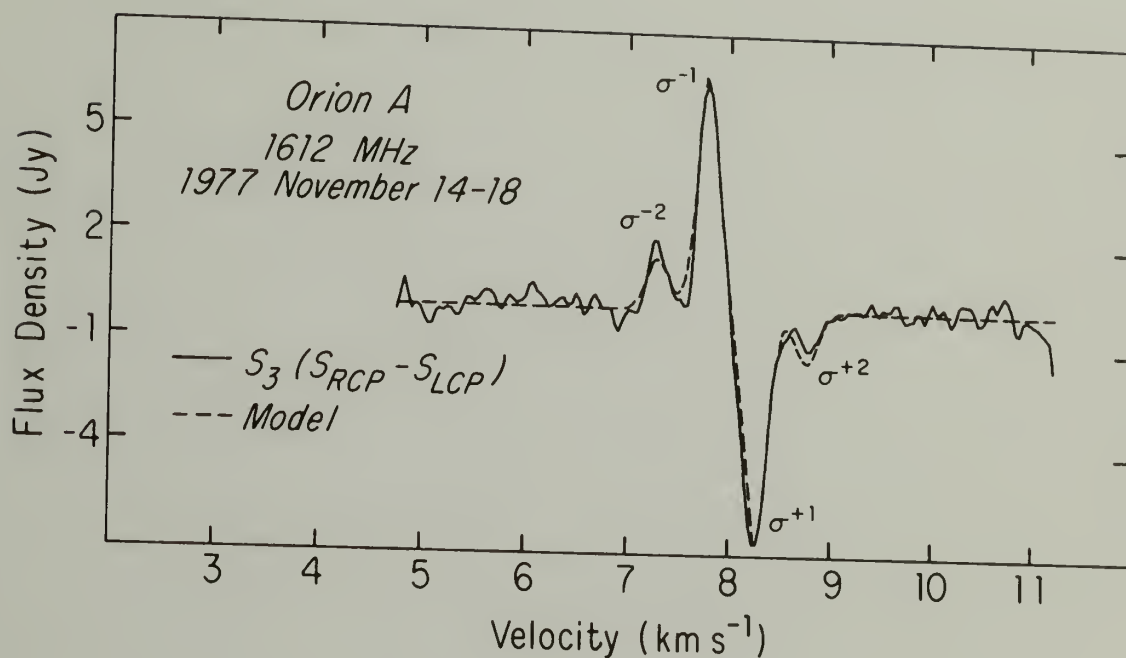


Fig. 42. The $S_3 (S_{RCP} - S_{LCP})$ spectra for the 1612 MHz transition. A model spectra (dashed line) for a Zeeman pattern from a cloud with $v_{LSR} = 8.02 \text{ km s}^{-1}$, $B = 4.0$ milligauss, and a FWHM of 0.26 km s^{-1} is superimposed on the data (solid line). The intensities of the σ^2 components of the model are only 0.44 as strong as expected in a Zeeman pattern from a partially saturated maser. The intensities of the σ^3 lines are zero in the model.

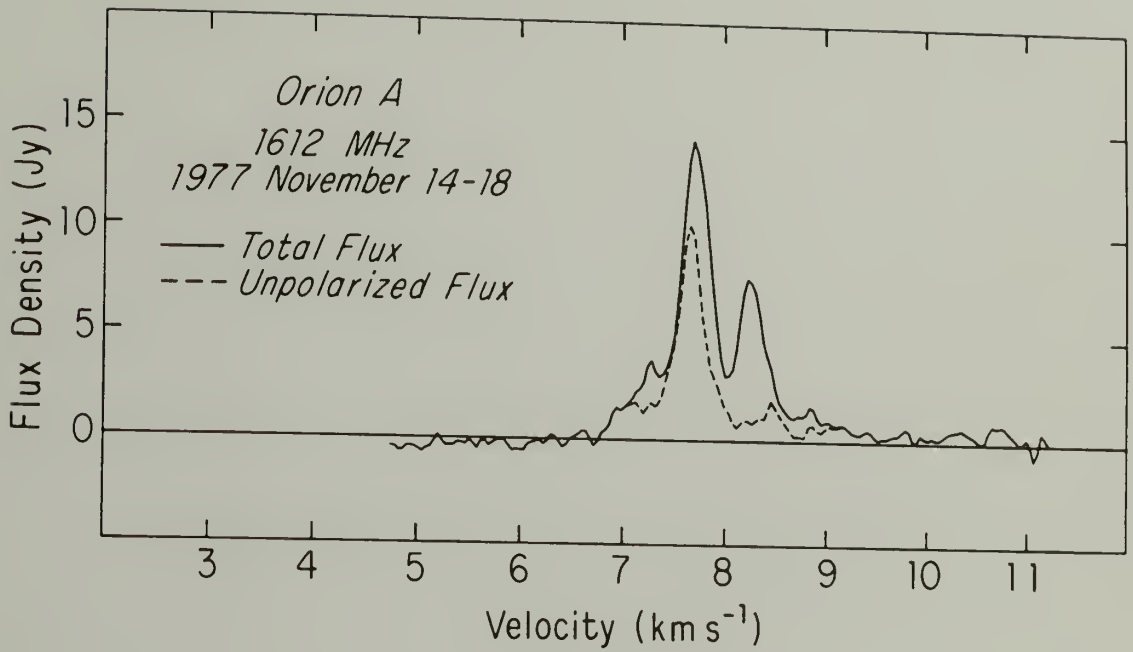


Fig. 43. The total power spectrum (solid line) for the 1612 MHz transition. The dashed line shows the flux density remaining after the circularly polarized emission was removed.

TABLE 13

The Right and Left Circularly Polarized and Unpolarized Features
in the 1612 MHz Spectrum of Orion

Velocity		Flux		FWHM	Polarization
Spectrum	Model*	Spectrum	Model*		
(km s ⁻¹)		(Jy)		(km s ⁻¹)	(%)
	(6.81)	<0.1	(0)		
7.11		1.8		0.42	0
7.28	(7.28)	2.0	(3.4)	0.20	100
7.66		9.6		0.34	0
7.79	(7.77)	6.8	(6.8)	0.23	100
8.25	(8.26)	6.8	(6.8)	0.28	-100
8.42		1.6		0.46	0
8.77	(8.76)	1.0	(3.4)	0.30	-100
	(9.23)	<0.1	(0)		

* The model has a center velocity of 8.02 km s⁻¹, a magnetic field of 4.0 milligauss and is partially saturated with a $\sigma^{\pm 1}$ flux density of 6.8 Jy.

The S3 ($S_{\text{RCP}} - S_{\text{LCP}}$) spectrum is shown in Figure 42. This spectrum rejects all the unpolarized or linearly polarized radiation. Observations with linear feeds showed no linear polarization. This is not unexpected since most Type 1 OH masers show little linear polarization. Faraday rotation or infrared line trapping could suppress the amplification of linearly polarized radiation (Goldreich, Keeley, and Kwan 1973). Gaussian profiles were fit to four circularly polarized features. The four modeled features of the S3 spectrum were subtracted from the total power spectrum to obtain an entirely unpolarized spectrum (Figure 43). Three more Gaussians were then fit to this unpolarized spectrum. The parameters of the seven Gaussian profiles determined by this analysis are presented in Table 13.

The striking pattern in the S3 spectrum (Figure 42) compels one to consider a Zeeman interpretation. Superimposed on this S3 data is the modeled spectrum of a cloud with a 4.0 milligauss field moving at 8.02 km s^{-1} . The full width at half maximum (FWHM) for each line in the model was 0.26 km s^{-1} . The flux density was set to 6.8 Jy for the σ^1 components, and to 1.5 Jy for the σ^2 components. The agreement between the observed and calculated velocity is excellent. The intensities of the σ^1 lines should be equal, as should the intensities of the σ^2 lines. In a partially saturated maser, the sum of the intensities of the σ^2 components should equal the intensity of one of the σ^1 lines. The slight difference in the intensity between the

model and the observations is explained in the next section as is the absence of the σ^3 lines. It should be emphasized that a five parameter model, i.e., center velocity, field strength, FWHM, and two intensities, explain the 12 parameter observations, i.e., four lines each with velocity, FWHM, and intensity. It also accounts for the missing σ^3 lines.

4.2.3 Maser Models. Any model for the Orion OH masers must explain the following observational results:

- the 1612 MHz σ^1 flux is 6.8 Jy,
- the 1612 MHz σ^2 flux is 1.5 Jy,
- the 1612 MHz σ^3 flux is less than 0.1 Jy,
- the 1665 MHz σ^1 flux is 40 Jy,
- the 1665 MHz apparent diameter is 25 a.u. (4×10^{14} cm).

A maser model predicts the flux and apparent diameter as a function of (1) the physical diameter and shape, e.g., sphere or tube, (2) the efficiency of the pump in inverting the population, (3) the density of OH molecules in the maser levels, (4) the collision rates, and (5) the input radiation (often set to zero). These physical parameters are assumed to be the same for all the 1612 MHz Zeeman transitions and 1665 MHz Zeeman transitions, leaving only the Einstein coefficients to explain the intensity differences.

A conceptually simple model of a one dimensional maser is developed in the appendix to this Chapter from the formalism of Moran (1976a). It illustrates many important maser effects. However, for this simple model to produce the measured 1612 MHz flux with the

1665 MHz diameter, either (1) the intensive physical parameters must assume extreme values, or (2) or the maser must be very short. A better model was clearly needed.

Goldreich and Keeley (1972) developed models for spherical and cylindrical masers. For both geometries, they determined the maximum brightness temperature and apparent size for unsaturated, partially saturated, and totally saturated conditions. A most interesting conclusion can be drawn from their formulae. In a partially saturated or a totally saturated maser, the flux does not depend on the Einstein coefficient. Thus, if the diameter, the density, the pump efficiency, and the collision rate are the same for the two transitions and the maser is saturated, the fluxes (in photons) for the transitions will be equal. Slight variations are expected for the reasons which follow. To calculate the flux of a spherical maser from the brightness temperature, one must use the apparent size rather than the true size. The apparent radius (in units of gain length) of a spherical maser is the square root of the true radius for an unsaturated maser, the square root of the radius of the unsaturated core for a partially saturated maser, and 0.7 the radius of the nonamplifying core for a totally saturated maser. These relations are only approximate so one would not expect observed intensities to be exactly equal. The brightness temperature of a cylindrical maser depends on the angle between the line of sight and the axis of the cylinder. In a partially saturated cylindrical maser, the transition with the smaller Einstein coefficient has a higher brightness temperature but a narrower beam. If the

maser is seen exactly on axis, the flux of the two transitions will be equal. As the observer moves off axis, the flux of the transition with the smaller Einstein coefficient falls more quickly.

If the maser transitions are not independent, competition between the lines for molecules in the same upper state will control the relative intensities of the lines. The σ^{+1} and σ^{-3} lines originate in the $m_F = +1$ magnetic substate of the upper level (Figure 38). Each line will grow exponentially during unsaturated growth but the gain for the σ^{+1} line is six times that for the σ^{-3} line. When the stronger line becomes saturated, it will be orders of magnitude greater than the weaker line. It will stimulate most molecules in the $m_F = +1$ upper state to radiate at its frequency. Few molecules will be left for the weaker line. This mechanism by itself would explain the absence of the σ^3 lines. The σ^{+2} and the σ^{-2} lines share the $m_F = 0$ upper level. After saturation they will compete with one another for the $m_F = 0$ molecules. The σ^2 lines should be equal since they have the same gain. Thus, one expects all the $m_F = +1$ molecules to radiate into the σ^{-1} line, all the $m_F = -1$ molecules to radiate into the σ^{+1} line, and the $m_F = 0$ state to divide its radiation between the σ^{+2} and σ^{-2} transitions. If the substates are equally populated, one would expect $I_{\sigma^{+1}} = I_{\sigma^{-1}} = I_{\sigma^{+2}} + I_{\sigma^{-2}}$. This is within a factor of two of what is observed.

Unfortunately, the 1612 MHz and 1665 MHz lines originate in the same upper state. The competition phenomena which so nicely explains the 1612 MHz spectra by itself predicts that the 1665 MHz transitions

should suppress the 1612 MHz emission. The $m_F = +1$ magnetic sublevel is the upper state of the 1612 MHz σ^{+1} and σ^{-3} lines, a 1665 MHz σ^- line, and a π component at both 1612 MHz and 1665 MHz. The $m_F = 0$ sublevel contributes to each of the 1612 MHz σ^2 lines, the 1612 MHz π^0 line, and both 1665 MHz σ lines. The $m_F = -1$ sublevel is similar to the $m_F = +1$ level. After one line saturates, all the lines with that upper magnetic substate compete for molecules in that substate. The 1665 MHz σ transitions, being stronger, determine the saturation geometry of the maser, i.e., the size of the unsaturated core. Within this core, all transitions undergo exponential amplification, and the 1665 MHz line soon dominates. In the saturated shell, it will stimulate most of the molecules to radiate at 1665 MHz.

Considering all the above effects, we find the intensities of the four 1612 MHz Zeeman components are within a factor of two of what is expected in a partially saturated maser. The difference between the observed intensity ratio of the lines and the theoretical ratio may be caused by different levels of saturation, the approximation for the apparent size of a spherical maser, or the alignment of a cylindrical maser. The absence of the third Zeeman component is explained by (1) a lower gain factor if the σ^1 components are unsaturated, or (2) suppression by the σ^1 lines if the σ^1 lines are saturated.

Remembering all the caveats just discussed, one may model the maser with the equations of Goldreich and Keeley (1972). The observed flux and apparent size of the 1665 MHz OH maser can be

produced by a partially saturated spherical maser with a physical diameter of $1.7 \cdot 10^{15}$ cm, an OH density of 50 cm^{-3} , a pump rate of 0.005 s^{-1} , a pump efficiency of 0.005, and a collision rate of 0.05 s^{-1} . In such a maser the 1612 MHz lines would be unsaturated, and the flux would be a few 10^{-6} Jy. Because the 1665 MHz radiation would suppress the 1612 MHz emission, it seems unlikely that the 1612 MHz masers and the 1665 MHz masers are coincident. Since the sizes of the 1612 MHz masers are unknown, it is even easier to model their flux. Parameters within an order of magnitude of those for the 1665 MHz masers could reproduce the 1612 MHz flux.

To summarize, the 1612 MHz spectrum of OH from Orion A provides an excellent example of Zeeman splitting. The center velocity is that of the molecular cloud, and the field strength is four milligauss. The intensity ratios of the 1612 MHz lines are within a factor of two of that expected for a partially saturated maser.

4.2.4 Appendix to Chapter IV: One Dimensional Maser Models. The radiation intensity from a one dimensional maser amplifying three Zeeman components is modeled in terms of L , the length of the maser, α , the absorption coefficient of the gas for the transition being amplified, and I_s , the saturation intensity, i.e., the intensity above which stimulated emission is the dominant path of deexcitation of the molecule. If a maser amplifies exponentially throughout, it is unsaturated. If parts of it are saturated, then it is partially saturated. If it is saturated throughout because radiation is going through it in both direction and the saturated parts of each direction

overlap, then it is totally saturated. Each Zeeman component, σ , has its own α and I_s . The absorption coefficient and I_s are determined by atomic parameters and physical conditions in the maser which, except for the Einstein coefficients, are assumed to be the same for all transitions. The transitions do not interact. In the first section of this Appendix I will solve for L , α , and I_s using the equations of transfer for one set of three circularly polarized components of the OH Zeeman pattern. The results are determined by the measured intensity of the three lines and an assumed background temperature, T_0 . For this simple model spontaneous emission is ignored. If spontaneous emission is the source of input radiation, and if the magnetic sublevels have different excitation temperatures, then the model could exactly fit the data. In the second section I will use these determined values of L , α , and I_s to estimate the physical properties of the gas.

4.2.4.1 The transfer equation. A schematic diagram for a one dimensional maser amplifying three 1612 MHz OH Zeeman components is shown in Figure 44(a). The intensity of each beam as a function of position is shown in Figure 44(b). The transfer equation for the unsaturated maser is $dI = (\alpha I + S) dx$ where α is positive for a maser. Spontaneous emission, S , will be ignored, and the maser will amplify input radiation, I_0 , coming from only one direction. The intensity of the radiation grows exponentially at first and is given by

$$I(x) = I_0 e^{\alpha x} \quad 4.2$$

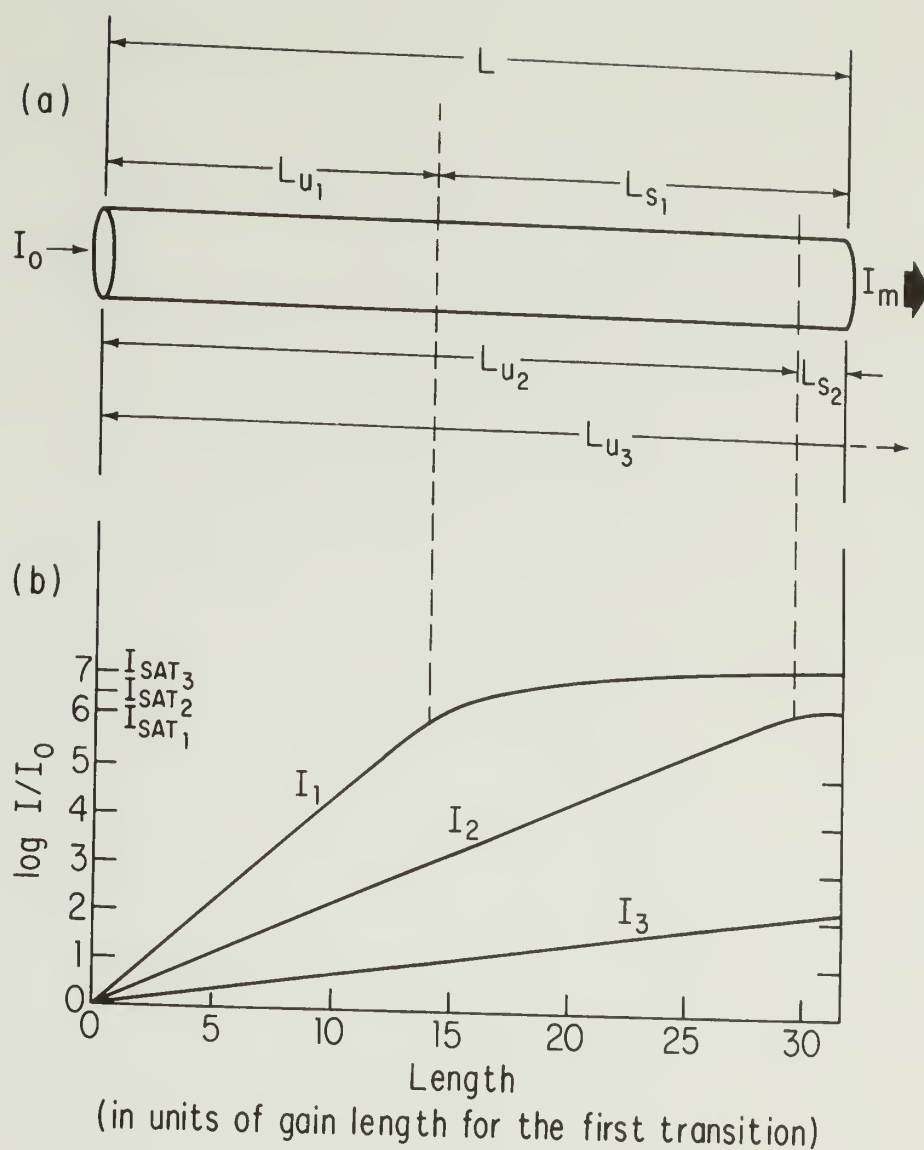


Fig. 44. (a) A schematic diagram of a one dimensional maser amplifying three independent transitions. I_0 is the intensity of the input radiation, and I_m is the intensity of the measured (emerging) radiation. L_u and L_s are the length for unsaturated and saturated growth of the radiation intensity. (b) The intensity, I , of the radiation for each transition as a function of distance into the maser. The horizontal axis is in units of gain length for the first transition. I_{sat} is the intensity at which a transition becomes saturated. The intensity difference between lines with different Einstein coefficients increases until the strongest line saturates. The strongest line then grows slowly while the weaker lines continue their exponential growth. Eventually, the intensities will be comparable again. In this diagram the first two transitions are partially saturated, and the third is unsaturated.

where x is the distance along the tube. After a certain distance the intensity is so strong that the gas cannot supply enough photons to the beam for exponential growth to continue. At this point the maser saturates; the intensity is I_s ; the distance at which it occurs is L_u , the total length of unsaturated growth; and

$$I_s = I_0 e^{\alpha L_u} . \quad 4.3$$

From this point on, the beam will stimulate almost every molecule in the upper level to radiate into the beam. The transfer equation becomes $dI = \alpha I_s dx$. The intensity grows linearly with distance at the rate with which it grew when it saturated. The intensity from this point on is

$$I(y) = I_s \alpha y \quad 4.4$$

where y is the distance from the point of saturation. This growth continues until the beam leaves the maser. The length for saturated growth, L_s , is $L - L_u$. I_m (intensity measured) is the intensity of the emerging beam which is proportional to the flux measured at the telescope.

$$I_m = I_s + \alpha L_s I_s . \quad 4.5$$

The α 's are proportional to the Einstein coefficients and the I_s 's are inversely proportional to the Einstein coefficients for this simple model (see Equations 4.16 and 4.17). For 1612 MHz OH emission the ratio of the Einstein coefficients for the three circularly polarized Zeeman lines is 6:3:1. Hence,

$$6 I_{s_1} = 3 I_{s_2} = I_{s_3} \quad 4.6$$

and from Equation 4.3,

$$2 I_{s_1} = 2 I_o e^{\alpha_1 L_{u_1}} = I_o e^{1/2 \alpha_1 L_{u_2}} = I_{s_2}. \quad 4.7$$

From $L = L_{u_1} + L_{s_1} = L_{u_2} + L_{s_2}$ and $\alpha_1 = 2 \alpha_2$, we find

$$\alpha_1 L_{u_2} = 2 \alpha_1 L_{u_1} + 2 \ln 2. \quad 4.8$$

I_{m_1} and I_{m_2} (Equation 4.5) may be expressed in terms of $\alpha_1 L_{u_1}$. Taking the difference between Equation 4.5 for the two lines yields

$$\begin{aligned} I_{m_1} - I_{m_2} &= I_o e^{\alpha_1 L_{u_1}} \left[\alpha_1 L_{u_1} - \frac{1}{2} + \ln \frac{1}{2} \right] \\ &= I_o e^{\alpha_1 L_{u_1}} \left[\alpha_1 L_{u_1} - 0.193 \right]. \quad 4.9 \end{aligned}$$

$\alpha_1 L_{u_1}$ is calculated from Equation 4.9 for the measured intensity of the two lines and an assumed value of I_o . I_s is determined by Equation 4.3. From Equation 4.5

$$\alpha_1 L_{s_1} = \frac{I_{m_1}}{I_{s_1}} - 1, \quad 4.10$$

and

$$\alpha_1 L = \alpha_1 L_{u_1} + \alpha_1 L_{s_1} = \ln \frac{I_{s_1}}{I_o} + \frac{I_{m_1}}{I_{s_1}} - 1. \quad 4.11$$

To convert the measured flux density to a specific intensity, one must divide by the solid angle of the source, i.e., $\pi/4 \phi^2 = \pi D^2$ distance⁻². Since the size of the 1612 MHz masers has not been measured, the size of the 1665 MHz masers will be used. Hansen *et al.* (1977) determined the diameter to be $4 \cdot 10^{14}$ cm. From the modeled flux density for the S3 spectrum (Table 13), the specific intensity of each Zeeman component is

$$I_{m_1} = 12.1 \cdot 10^{13} \text{ Jy sterad}^{-1}$$

$$I_{m_2} = 2.7 \cdot 10^{13} \text{ Jy sterad}^{-1}$$

$$I_{m_3} < 0.2 \cdot 10^{13} \text{ Jy sterad}^{-1}.$$

A similar set of equations (4.7 through 4.11) could be produced from the σ^1 and σ^3 lines. A measured flux for the σ^3 components would make it possible to eliminate I_o . Since the third line is undetected, I_o is assumed to be the thermal radiation from the gas and dust at 100°K. The Rayleigh-Jeans' approximation gives

$$\begin{aligned} I_o &= k \frac{f^2}{c^2} T_o \\ &= 40\,000 T_o \text{ Jy sterad}^{-1} \text{ for } 1612 \text{ MHz} \end{aligned} \tag{4.12}$$

for each polarization where

k is the Boltzmann constant,

c is the speed of light,

f is the frequency (1612 MHz), and

T_o is the kinetic temperature.

Table 14 gives the values of αL and I_s for a range of temperatures. Over a range of physically believable temperatures, the optical depth changes by only a factor of 2 and the saturation intensity by a factor of 3. The errors introduced into the physical parameters by assuming that $T_o = 1 - 10\,000^\circ\text{K}$ will be smaller than the order of magnitude accuracy we are trying to obtain. The upper limit (0.1 Jy) on the flux density of the third line is not very restrictive. The solution obtained from the first two lines implies the third line is unsaturated. I_{m_3} would be 10^9 Jy sterad $^{-1}$, which is a factor of 10 000 less than I_{m_1} .

The preceding analysis assumed that the first two Zeeman lines arose in a partially saturated maser. If the first or second line were unsaturated, then I_o must be within a few orders of magnitude of I_m . For example, if both lines were unsaturated

$$I_{m_1} = I_o e^{\alpha_1 L} \quad 4.13$$

and

$$I_{m_2} = I_o e^{1/2 \alpha_1 L} \quad 4.14$$

Removing $\alpha_1 L$ one has

$$I_o = \frac{I_{m_2}}{I_{m_1}} I_{m_2}, \quad 4.15$$

which requires $T_o = 10^8$ °K. If I_{m_2} had just become saturated, $T_o = 5 \cdot 10^5$ °K. An unsaturated maser therefore requires an unreasonably high input temperature.

TABLE 14
 Model Optical Depths and Saturated Intensities
 for the 1612 MHz OH Masers

	Temperature ($^{\circ}$ K)					
	1	10	100	1000	10000	
$\alpha_1 L_{u_1}$	18.4	16.2	14.1	12.0	9.9	
$\alpha_1 L_{u_2}$	38.2	33.8	29.6	25.4	19.2	
$\alpha_1 L_{u_3}$	121.2	108.0	95.4	82.8	70.2	
$\alpha_1 L_{s_1}$	23.8	21.3	17.2	13.9	11.2	
$\alpha_1 L$	42.2	37.5	31.3	25.9	21.1	
I_{s_1}	2.9	4.3	5.3	6.5	8.0	10^{12} Jy sterad $^{-1}$
I_{s_2}	5.8	8.6	10.6	13.0	16.0	10^{12} Jy sterad $^{-1}$
I_{s_3}	17.4	25.8	31.8	39.0	48.0	10^{12} Jy sterad $^{-1}$

$\alpha_1 L_{u_1}$ is from Equation 4.9.

$\alpha_1 L_{u_2}$ and $\alpha_1 L_{u_3}$ are from Equation 4.8.

$\alpha_1 L_{s_1}$ is from Equation 4.10.

$\alpha_1 L$ is from Equation 4.11.

In summary, I have assumed that (1) the three Zeeman components originate in the same one dimensional maser, (2) that all the physical parameters of the maser, e.g., length, density, and pump rate, are identical except for the Einstein coefficients, and (3) that the transitions do not influence one another. From the analysis of the amplitudes of the three lines, I conclude that the first two transitions are partially saturated, and that the third is unsaturated. Assuming $T_0 = 1000^\circ\text{K}$, the maser parameters are $\alpha_1 L = 31.3$ and $I_{s1} = 5 \cdot 10^{12}$ Jy sterad⁻¹.

4.2.4.2 The physical parameters. Using the values of T_0 , αL , and I_s just determined in Section 4.2.4.1, and the observed values of frequency, f , line width, Δf , and solid angle, Ω , subtended by the maser, I will estimate the length, L , the OH density, n_{OH} , the collision deexcitation rate, C , the pump rate, P , and the pump efficiency, η_p , of the maser. Moran (1976a) has expressed α and I_s in terms of atomic values and local cloud parameters.

$$\alpha = \frac{h f B}{4\pi\Delta f} \frac{n_{\text{OH}} \eta_p}{1 + \frac{2C}{P}} \quad 4.16$$

and

$$I_s = \frac{1 + \frac{2C}{P}}{\frac{B\Omega}{2\pi P}} \quad 4.17$$

where h is Planck's constant. An Einstein B may be calculated from an Einstein A by

$$B = g \frac{c^2}{h f^3} A. \quad 4.18$$

Note that there is no factor of 2 in the denominator since the molecule responds to only one mode of polarization. The statistical weight, g , is 1 because the magnetic field removes all degeneracy. The Einstein coefficients for the Zeeman transitions are calculated from the total Einstein coefficient for the 1612 MHz transition (Turner 1966) and the ratio for the Zeeman components (Rogers 1967). These values were calculated from Condon and Shortley (1957) and Townes and Schawlow (1955). The Einstein coefficient for all 1612 MHz transitions is the sum of the individual Zeeman transition Einstein coefficients divided by the statistical weight of the upper level. Thus

$$A_{\pi 0} = 7.746 \cdot 10^{-12} \text{ s}^{-1} \text{ (1 transition),}$$

$$A_{\pi \pm 1, \sigma \pm 1} = 5.811 \cdot 10^{-12} \text{ s}^{-1} \text{ (4 transitions),}$$

$$A_{\sigma \pm 2} = 2.904 \cdot 10^{-12} \text{ s}^{-1} \text{ (2 transitions),}$$

$$A_{\sigma \pm 3} = 0.969 \cdot 10^{-12} \text{ s}^{-1} \text{ (2 transitions),}$$

and

$$A_{1612} = 12.91 \cdot 10^{-12} \text{ s}^{-1} .$$

The line width, Δf , is 3 kHz which is the Doppler width for $T = 100^\circ\text{K}$. The measured width is half this value as might be expected for a partially saturated maser. The solid angle of the stimulating radiation seen by the molecule is $\Omega = \pi (D/2)^2 / (L/2)^2$ where $(L/2 = L_u)$.

The point of saturation for the first line is about one-half L . Since the sizes of the 1612 MHz masers have not been measured, D is assumed to be the diameter of a 1665 MHz maser. Since the different transitions have different L_u , they will also have different Ω . This effect is ignored in this model.

Putting the constants and the assumed values of Δf and Ω into Equations 4.16 and 4.17, I find for the $\sigma^{\pm 1}$ transitions that

$$\alpha = 5 \cdot 10^{-14} \eta_P n_{OH} (1 + 2C/P)^{-1} \text{ cm}^{-1} \quad 4.19$$

and

$$I_s = 1 \cdot 10^{15} P(1 + 2C/P) (L/D)^2 \text{ Jy sterad}^{-1} \quad 4.20$$

for P and C in s^{-1} , L in cm , and n_{OH} in particles cm^{-3} . Multiplying Equation 4.19 by L , dividing that by Equation 4.20, and using the values of α and I_s obtained in the first section of this Appendix for the σ^1 line at 100°K ,

$$L = \frac{1.2 \cdot 10^{12} \eta_P n_{OH}}{P(1 + 2C/P)^2} . \quad 4.21$$

Unfortunately, η_P , n_{OH} , C , and P are not observable. If I assume that values of Goldreich and Keeley (1972), i.e.,

$$\begin{aligned} \eta_P &= 0.01 \\ n_{OH} &= 100 \text{ cm}^{-3} \quad \text{with 10\% in the maser state} \\ C &= 0.1 \text{ s}^{-1} \\ P &= 0.01 \text{ s}^{-1} , \end{aligned}$$

then I obtain $L = 3 \cdot 10^{10}$ cm. This length compared with the observed diameter implies that the maser is a very thin sheet. It is certainly not the tube originally assumed. To create a tube with $L = 20 D$ would require that the parameters be varied by a factor of 10^5 . This seems unrealistic.

The following plausible, self-consistent parameters do satisfy Equation 4.21:

$$\begin{aligned} L &= D = 4 \cdot 10^{14} \text{ cm} \\ \eta_P &= 0.1 \\ n_{\text{OH}} &= 100 \text{ cm}^{-3} \\ C &= 0.001 \text{ s}^{-1} \\ P &= 0.001 \text{ s}^{-1}. \end{aligned}$$

Since the length of the maser is equal to its diameter, the maser is essentially a sphere. Unfortunately, the one dimensional model from which Equation 4.21 was derived does not change smoothly into a spherical model because the effects of radiation not directed toward the observer have been ignored in determining the saturation of the maser. A more detailed model should be used. In Section 4.2.3, I use the spherical maser model of Goldreich and Keeley (1972) to determine reasonable values for the physical parameters of the masers.

The choice of physical parameters in which to model the maser is arbitrary. For example, the OH density could be expressed as a fraction of the H_2 density. The collision rate could be expressed as

$$C = 10.5 \cdot 10^{-12} \sqrt{T} \exp(-230^\circ\text{K}/T) n_{\text{H}_2} \text{ s}^{-1}$$

for an OH - H₂ collisional cross-section of $6 \cdot 10^{-16} \text{ cm}^{-2}$ (Gwinn et al. 1973). For $T = 100^\circ\text{K}$ and $n_{\text{H}_2} = 10^8 \text{ cm}^{-3}$, $C = 0.001 \text{ s}^{-1}$, which agrees with the value stated in the previous paragraph.

CHAPTER V

CONCLUSIONS

In this dissertation I have discussed the water vapor masers and the hydroxyl masers toward Orion A. To gain a better understanding of the spatial structure and time variations of the water vapor masers, I observed Orion A at 22 GHz at six epochs from 1972 to 1978. From these observations I produced six maps with relative positional accuracy of 0".01 in right ascension and 0".1 in declination along with six total power and cross power spectra.

The water vapor masers define the spatial extent and grouping of the maser region. They cover an area with a diameter of 30" centered on the Kleinmann-Low nebula. Approximately 30 strong, low velocity features lie within 20 km s^{-1} of the molecular cloud velocity. The intensity varies with a time scale of weeks to years, and flux density has been as great as 30 000 Jy. The full width at half maximum (FWHM) of an individual velocity feature is typically 1 km s^{-1} . Most of the individual masers are only a few a.u. in diameter.

The most fundamental spatial grouping of the masers is a "cluster". The diameter of a cluster is less than 1000 a.u. (2"). Within a cluster are one or more velocity features which are often not coincident. The position of a velocity feature is constant over years to 50 a.u. The lifetime of a cluster is longer than the ten years over which H_2O masers have been observed. The individual velocity features also last for years, but they show intensity variations on a time scale of weeks or months. The most likely velocity separation between features in a

cluster is 1 km s^{-1} , but separations larger than 20 km s^{-1} have been observed. Although the lines have a full width at half maximum of only 1 km s^{-1} , most strong features are accompanied by weak emission over several km s^{-1} from the same cluster.

Intensity variations of the individual velocity features or the "clusters" do not show a correlation which would suggest a common pump. Although it seems likely that the velocities are due to expansion, contraction, or rotation, observations of the masers do not prove this.

The transverse velocities of the masers are less than or equal to the radial velocity dispersion of the masers. The failure to detect very high transverse motion assures us that the features are not high velocity features with most of their velocity across the line of sight, but a large amplification path along the line of sight.

I propose that Orion A shows four types of H_2O masers which are associated with star formation. The first type is strong, slowly varying, and occurs in isolated clusters (i.e., the northeast clusters). The second type is more variable and not too intense, i.e., the southwest clusters. The third type is the high velocity maser. These three types of masers are related by the following evolutionary sequence. The first type of maser occurs in a smoothly contracting cloud. When the star halts collapse, an unstable cocoon forms, and the second type of maser appears. As a star evolves further, a compact HII region forms, the cocoon is destroyed and the low velocity masers disappear. However, a stellar wind from the newly formed star may create the high velocity masers. The fourth type of H_2O maser is the

"field" maser which occurs at random positions over the maser region. The field masers are rather weak and may blend into the high velocity features which lie farther from the strong masers. A base of emission formed by the weak field masers may underlie the entire H_2O spectrum.

In addition to the H_2O masers associated with star formation, I find in Orion a fifth type of H_2O maser. These masers have velocities from -7 to -3 km s^{-1} and from $+15$ to $+18 \text{ km s}^{-1}$. The diameter of these masers is 10 to 60 a.u. Furthermore, these masers vary much less rapidly in intensity than the others. All these H_2O masers of this fifth type lie within 1000 a.u. of one another. The 1665 MHz OH masers with similar velocities are less variable and less polarized than the other OH masers. Since these large OH masers were resolved in the VLBI experiment, their positions are poorly known. Their diameters must exceed 100 a.u. The strong SiO masers are seen only at these velocities and their positions coincide with the H_2O maser positions to within the one sigma errors. The evidence strongly suggests that all these masers exist in expanding shells of gas about an evolved star.

The three OH masers which were detected in the VLBI experiment had apparent diameters of 10 - 30 a.u. The two strongest of these were coincident, and the third was within 500 a.u. of them. The coincidence features were circularly polarized in opposite senses, suggesting that they may be Zeeman components of a 3 milligauss magnetic field. Single telescope observations of the 1612 MHz hydroxyl masers show a readily identifiable Zeeman pattern corresponding to a 4 milligauss field.

Although many questions about masers have been answered, more research needs to be done. The hydroxyl maser model developed in Section 4.2 could be further constrained by determining the size of the 1612 MHz OH masers. That model also predicts that the 1612 MHz and 1665 MHz masers should not be coincident. It is most important to determine if the OH masers with the shell structure velocity pattern are coincident with the H_2O and SiO masers at that velocity. I have submitted a proposal to use the Very Large Array to make these observations.

Answering questions about the water vapor masers will be more difficult. Some questions, such as how long does a cluster last, will be answered only with the passage of time. As we see clusters appear and disappear we may gain a better understanding of what they are. However, there is no apparent order to the behavior of the individual water vapor features, and I feel that any advances in that area will be statistical.

Although more observations will not yield quick answers to the problems of star formation, I hope to continue to monitor the Orion region because of the unusual phenomena found there. The methanol masers are unique. The SiO masers and the shell pattern in the H_2O and OH spectra are suggestive of an evolved star. The high velocity gas requires a large amount of energy from an unseen source. And the BN object seems to be a star at birth. Perhaps all these phenomena are associated with some unexpected and short-lived phase of star formation. Thus the Orion nebula and molecular cloud will continue to be the most exciting and best observed region of star formation.

B I B L I O G R A P H Y

- Allen, C. W. 1973, Astrophysical Quantities (London: Athlone Press), p. 261.
- Appenzeller, I., and Tscharnuter, W. 1974, *Astron. and Astrophys.*, 30, 423.
- Balick, B., Gammon, R. H., and Hjellming, R. M. 1974, *Pub. astron. Soc. Pacific*, 86, 616.
- Barrett, A. H., Ho, P., and Martin, R. N. 1975, *Ap. J.*, 198, L119.
- Barrett, A. H., Ho, P.T.P., and Myers, P. C. 1977, *Ap. J.*, 211, L39.
- Barrett, A. H., Schwartz, P. R., and Waters, J. W. 1971, *Ap. J.* (Letters), 168, L101.
- Becklin, E. E., Beckwith, S., Gatley, I., Mathews, K., Neugebauer, G., Sarazin, C., and Werner, M. W. 1976, *Ap. J.*, 207, 770.
- Becklin, E. E., and Neugebauer, G. 1967, *Ap. J.*, 147, 799.
- Beckwith, S., Persson, S. E., Neugebauer, G., and Becklin, E. E. 1978, *Ap. J.*, 223, 464.
- Blaauw, A. 1964, *Ann. Rev. Astron. Astrophys.*, 2, 213.
- Bologna, J. M., Johnston, K. J., Knowles, S. H., Mango, S. A., and Sloanaker, R. M. 1975, *Ap. J.*, 199, 86.
- Buhl, D., Snyder, L. E., Lovas, F. J., and Johnson, D. R. 1974, *Ap. J.* (Letters), 192, L97.
- Buhl, D., Snyder, L. E., Schwartz, P. R., and Barrett, A. H. 1969, *Ap. J.* (Letters), 158, L97.

- Burdjuzha, V. V., Ruzmaikina, T. V., and Barshalovich, D. A. 1975, in HII Regions and Related Topics, eds. T. L. Wilson and D. Downes (Berlin: Springer), p. 195.
- Burke, B. F., Papa, D. C., Papadopoulos, G. D., Schwartz, P. R., Knowles, S. H., Sullivan, W. T., Meeks, M. L., and Moran, J. M. 1970, *Ap. J.*, 160, L63.
- Buxton, R. B., Barrett, A. H., Ho, P.T.P., and Schneps, M. H. 1977, *A. J.*, 82, 985.
- Cannell, W. D., and Ianna, P. A. 1977, *A. J.*, 82, 360.
- Chaisson, E. J., and Beichman, C. A. 1975, *Ap. J. (Letters)*, 199, L39.
- Chelli, A., Lena, P., and Sibille, F. 1979, *Nature*, 278, 143.
- Cheung, A. C., Rank, D. M., Townes, C. H., Thornton, D. D., and Welch, J. W. 1969, *Nature*, 221, 626.
- Clark, B. G. 1973, *Proc. IEEE*, 61, 1242.
- Cockran, W. D., and Ostriker, J. P. 1977, *Ap. J.*, 211, 393.
- Condon, E. U., and Shortley, G. H. 1955, The Theory of Atomic Spectra, (2d ed.; Cambridge: Cambridge University Press).
- Cook, A. H. 1966, *Nature*, 211, 503.
- Davis, J. H., Blair, G. N., Van Till, H., and Thaddeus, P. 1974, *Ap. J. (Letters)*, 190, L117.
- Davis, J. H., and Vanden Bout, P. 1973, *Ap. Letters*, 15, 43.
- Dopita, M. A., Isobe, S., and Meaburn, J. 1975, *Astrophys. Space Sci.*, 34, 91.
- Downes, D., Genzel, R., Moran, J. M., Johnston, K. J., Matveyenko, L. I., Kogan, L. R., Kostenko, V. I., and Romang, B. 1979, *Astron. Astrophys.*, 79, 233.

- Elmegreen, B. G., and Lada, C. J. 1977, *Ap. J.*, 214, 725.
- Evans, N. J., II, Plambeck, R. L., and Davis, J. H. 1979, *Ap. J.* (Letters), 227, L25.
- Forster, J. R., Welch, W. J., Wright, M.C.H., and Braudy, A. 1978, *Ap. J.*, 221, 137.
- Gatley, I., Becklin, E. E., Matthews, K., Neugebauer, G., Penston, M. V., and Scoville, N. 1974, *Ap. J.* (Letters), 191, L121.
- Gehrz, R. D., Hackwell, J. A., and Smith, J. R. 1975, *Ap. J.*, 202, L33.
- Genzel, R., and Downes, D. 1977a, *Astron. Astrophys.*, 61, 117.
- Genzel, R., and Downes, D. 1977b, *Astron. Astrophys. Suppl.*, 30, 145.
- Genzel, R., and Downes, D. 1979, *Astron. Astrophys.*, 72, 234.
- Genzel, R., Downes, D., Moran, J. M., Johnston, K. J., Spencer, J. H., Matveyenko, L. I., Kogan, L. R., Kostenko, V. I., Ronnang, B., Haschick, A. D., Reid, M. J., Walker, R. C., Giuffrida, T. S., Burke, B. F., and Moiseev, I. G. 1979a. *Astron. Astrophys.*, 78, 239.
- Genzel, R., Downes, D., Moran, J. M., Johnston, K. J., Spencer, J. H., Walker, R. C., Haschick, A., Matveyenko, L. I., Kogan, L. R., Kostenko, V. I., Ronnang, B., Rydbeck, O.E.H., and Moiseev, I. G. 1978, *Astron. Astrophys.*, 66, 13.
- Genzel, R., Downes, D., Schwartz, P. R., Spencer, J. H., Pankonin, V., and Baars, J.W.M. 1980, *Ap. J.*, in press.
- Genzel, R., Moran, J. M., Lane, A. P., Predmore, C. R., Ho, P.T.P., Hansen, S. S., and Reid, M. J. 1979b, *Ap. J.* (Letters), 231, L73.

- Gilmore, W. S. 1978, 'Radio Continuum Interferometry of Dark Clouds: A Search for Newly Formed HII Regions', University of Maryland (unpublished Ph.D. Thesis).
- Goldreich, P., and Keeley, D. A. 1972, *Ap. J.*, 174, 517.
- Goldreich, P., Keeley, D. A., and Kwan, J. Y. 1973, *Ap. J.*, 182, 55.
- Gottlieb, C. A., Ball, J. A., Gottlieb, E. W., and Dickinson, D. F. 1979, *Ap. J.*, 227, 422.
- Grasdalen, G. L. 1974, *Ap. J.*, 193, 373.
- Gwinn, W. D., Turner, B. E., Goss, W. M., and Blackman, G. L. 1973, *Ap. J.*, 179, 789.
- Hall, D.N.B., Kleinmann, S. G., Ridgway, S. T., and Gillett, F. C. 1978, *Ap. J. (Letters)*, 223, L47.
- Hansen, S. S. 1977, The Mark II 576 Channel, Three Station VLBI Processor, NRAO User's Manual Series #26.
- Hansen, S. S., Moran, J. M., Reid, M. J., Johnston, K. J., Spencer, J. H., and Walker, R. C. 1977, *Ap. J. (Letters)*, 218, L65.
- Herbig, G. H. 1960, *Ap. J. Suppl.*, 4, 337.
- Herzberg, G. 1950, *Spectra of Diatomic Molecules*, (Princeton, New Jersey: D. Van Nostrand).
- Hills, R., Pankonin, V., and Landecker, T. L. 1975, *Astron. Astrophys.*, 39, 149.
- Ho, P.T.P., and Barrett, A. H. 1978, *Ap. J. (Letters)*, 224, L23.
- Horner, S., von 1975, in *HII Regions and Related Topics*, eds. T. L. Wilson and D. Downes (Berlin: Springer-Verlag), p. 53.
- Hoyle, F. 1953, *Ap. J.*, 118, 513.

- Isobe, S. 1973, in Interstellar Dust and Related Topics, IAU Symposium No. 52, eds. J. M. Greenberg and H. C. van de Hulst (Dordrecht: Reidel), p. 433.
- Jaffe, D., and Pankonin, V. 1978, Ap. J., 226, 869.
- Johnson, H. M. 1965, Ap. J., 142, 964.
- Johnston, K. J., Knowles, S. H., Sullivan, W. T., III, Moran, J. M., Burke, B. F., Lo, K. Y., Papa, D. C., Papadopoulos, G. D., Schwartz, P. R., Knight, C. A., Shapiro, I. I., and Welch, W. J. 1971, Ap. J. (Letters), 166, L21.
- Joyce, R. R., Gezari, D. Y., Scoville, N. Z., and Furenlid, I. 1978, Ap. J., 219, L29.
- Kleinmann, D. E., and Low, F. J. 1967, Ap. J. (Letters), 149, L1.
- Knowles, S. H., and Batchelor, R. A. 1978, M.N.R.A.S., 184, 107.
- Knowles, S. H., Caswell, J. L., and Goss, W. M. 1976, M.N.R.A.S., 157, 537.
- Knowles, S. H., Mayer, C. H., Cheung, A. C., Rank, D. M., and Townes, C. H. 1969a, Science, 163, 1055.
- Knowles, S. H., Mayer, C. H., Sullivan, W. T., and Cheung, A. C. 1969b, Science, 166, 221.
- Kukolich, S. G. 1969, J. Chem. Phys., 50, 3751.
- Kutner, M. L., Evans, N. J., II, and Tucker, K. D. 1976, Ap. J., 209, 452.
- Kutner, M. L., Thaddeus, P., Penzias, A. A., Wilson, R. W., and Jefferts, K. B. 1973, Ap. J., 183, L27.
- Kutner, M. L., Tucker, K. D., Chin, G., and Thaddeus, P. 1977, Ap. J., 215, 521.

- Kwan, W., and Scoville, N. 1976, Ap. J. (Letters), 210, L39.
- Lada, C. J. 1980, in Giant Molecular Clouds in the Galaxy, eds. P. Solomon and M. G. Edmunds (New York: Pergamon Press), in press.
- Larson, R. B. 1969, M.N.R.A.S., 145, 271.
- Larson, R. B. 1973, Fund. Cosmic Phys., 1, 1.
- Larson, R. B. 1977, in Star Formation, IAU Symposium No. 75, eds. T. de Jong and A. Maeder (Dordrecht: Reidel), p. 249.
- Lees, R. M. 1973, Ap. J., 184, 763.
- Liszt, H. S., Wilson, R. W., Penzias, A. A., Jefferts, K. B., Wannier, P. G., and Solomon, P. M. 1974, Ap. J., 190, 557.
- Little, L. T., White, G. J., and Riley, P. W. 1977, M.N.R.A.S., 180, 639.
- Mader, G. L., Johnston, K. J., and Moran, J. M. 1978, Ap. J., 224, 115.
- Mader, G. L., Johnston, K. J., Moran, J. M., Knowles, S. H., Mango, S.A., Schwartz, P. R., and Waltman, W. B. 1975, Ap. J. (Letters), 200, L111.
- Manchester, R. N., and Taylor, J. H. 1977, Pulsars, (San Francisco: W. H. Freeman).
- Martin, A.H.M., and Gull, S. F. 1976, M.N.R.A.S., 175, 235.
- Matsakis, D. N., Cheung, A. C., Wright, M.C.H., Askne, J. A., Townes, C. H., and Welch, W. J. 1980, Ap. J., in press.
- Meeks, M. L., Carter, J. C., Barrett, A. H., Schwartz, P. R., Waters, J. W., and Brown, W. E., III 1969, Science, 165, 180.
- Mestel, L. 1971, Quart. J. R.A.S., 12, 402.

- Mezger, P. G. 1978, Infrared Astronomy, eds. G. Setti and G. G. Fazio (Dordrecht, Holland: D. Reidel), p. 1.
- Mezger, P. G., and Smith, L. F. 1977, in Star Formation, IAU Symposium No. 75, eds. T. de Jong and A. Maeder (Dordrecht: Reidel), p. 133.
- Moran, J. M. 1973, Proc. IEEE, 61, 1236.
- Moran, J. M. 1976a, in Frontiers of Astrophysics, ed. Eugene H. Avrett (Cambridge: Harvard University Press), p. 385.
- Moran, J. M. 1976b, in Methods of Experimental Physics, Vol. 12, Part C, ed. M. L. Meeks (New York: Academic Press), p. 228.
- Moran, J. M., Johnston, K. J., Spencer, J. H., and Schwartz, P. R. 1977, Ap. J., 217, 434.
- Moran, J. M., Papadopoulos, G. D., Burke, B. F., Lo, K. Y., Schwartz, P. R., Thacker, D. L., Johnston, K. J., Knowles, S. H., Reisz, A. C., and Shapiro, I. I. 1973, Ap. J., 185, 535.
- Mouschovias, Telemachos Ch. 1976, Ap. J., 207, 141.
- Munch, G., and Wilson. O. C. 1962, Z. Astrophys., 56, 127.
- Osterbrock, D., and Flather, E. 1959, Ap. J., 129, 26.
- Pankonin, V., Walmsley, C. M., and Harwit, M. 1979, Astron. Astrophys., 75, 34.
- Phillips, T. G., Huggins, P. J., Neugebauer, G., and Werner, M. W. 1977, Ap. J., 217, L161.
- Raimond, E., and Eliasson, B. 1969, Ap. J., 155, 817.
- Rickard, L. J, Zuckerman, B., and Palmer, P. 1975, Ap. J., 200, 6.
- Rieke, G. M., Low, F. J., and Kleinmann, D. E. 1973, Ap. J., 186, L7.
- Rishbeth, H. 1958, Australian J. Phys., 11, 550.

- Roberts, M. S. 1957, *Pub. astron. Soc. Pacific*, 69, 59.
- Rogers, A.E.E. 1967, 'Emission and Absorption of Microwave Radiation by Interstellar OH', Massachusetts Institute of Technology (unpublished Ph.D. Thesis).
- Salpeter, E. E. 1955, *Ap. J.*, 121, 161.
- Schiffer, F. H., III, and Mathis, J. S. 1974, *Ap. J.*, 194, 597.
- Schraml, J., and Mezger, P. G. 1969, *Ap. J.*, 156, 269.
- Scoville, N. Z. 1980, in Giant Molecular Clouds in the Galaxy, eds. P. Solomon and M. G. Edmunds (New York: Pergamon Press), in press.
- Silk, J. 1977, *Ap. J.*, 214, 718.
- Snyder, L. E., and Buhl, D. 1974, *Ap. J. (Letters)*, 189, L31.
- Snyder, L. E., and Buhl, D. 1975, *Ap. J.*, 197, 329.
- Snyder, L. E., Dickinson, D. F., Brown, L. W., and Buhl, D. 1978, *Ap. J.*, 224, 512.
- Strel'nitskii, V. S. 1974, *Soviet Phys. Uspekhi*, 17, 507.
- Sullivan, W. T. 1971, *Ap. J.*, 166, 321.
- Sullivan, W. T. 1973, *Ap. J. Suppl.*, 25, 393.
- Thaddeus, P., Mather, J., Davis, J. H., and Blair, G. N. 1974, *Ap. J. (Letters)*, 192, L33.
- Townes, C. H., and Schawlow, A. L. 1955, Microwave Spectroscopy, (New York: McGraw-Hill).
- Tucker and Kutner (private communication to Barrett, Ho, and Martin, 1975).
- Turner, B. E. 1966, *Nature*, 212, 184.

- VanVleck, J. H., and Middleton, D. 1966, Proc. IEEE, 54, 2.
- Werner, M. W., Gatley, I., Harper, D. A., Becklin, E. E., Loewenstein, R. F., Telesco, C. M., and Thronson, H. A. 1976, Ap. J., 204, 420.
- Wilson, L. A., and Hill, S. J. 1979, Ap. J., 228, 854.
- Wilson, T. L., Downes, D., and Bieging, J. 1979, Astron. Astrophys., 71, 275.
- Wynn-William, C. G., and Becklin, E. E. 1974, Pub. astron. Soc. Pacific, 86, 5.
- Yorke, H. W., and Krugel, E. 1977, Astron. Astrophys., 54, 183.
- Zuckerman, B. 1973, Ap. J., 183, 863.
- Zuckerman, B. 1979, Ap. J., 230, 442.
- Zuckerman, B., Kuiper, T.B.H., and Rodriguez Kuiper, E. N. 1976, Ap. J. (Letters), 209, L137.
- Zuckerman, B., and Palmer, P. 1974, Ann. Rev. Astron. Astrophys., 12, 279.
- Zuckerman, B., and Palmer, P. 1975, Ap. J. (Letters), 199, L35.

A P P E N D I X

DETAILED MODELS FOR THE WATER VAPOR OBSERVATIONS

Several authors, e.g., Genzel and Downes (1977a,b), and Genzel et al. (1978), using positional data and the statistics of many observations of H_2O maser regions, developed the models presented in this appendix. One model was reviewed briefly at the end of Section 1.1, and is reviewed in more detail later in this appendix. The observations leading to these models follow. These observations come from several regions of star formation, particularly Orion A, W3, and W49. W49 is at least 1000 times stronger in H_2O radiation and is at least ten times more massive than Orion A. Otherwise, they are similar.

A.1 Observations of Water Vapor Maser Regions

A.1.1 Spectra. An H_2O spectrum for a region of star formation shows many features. The luminosity in a single line 100 kHz wide may be $10^{-4} L_{\odot}$. The spectral lines are classified as high or low velocity features.

A.1.1.1 The low velocity features. The low velocity features are within 20 km s^{-1} of the velocity of the molecular cloud or HII region with which the masers are associated.

Genzel and Downes (1977b) find about half the H_2O sources have double or triple peaks in their spectra. The gas motion creating these patterns is the subject of Appendix Section A.2.2.1. The major peaks in most sources contain several lines. These peaks are not

hyperfine components but are probably due to some kinematic characteristic of the gas. The rapid time variation of H_2O masers makes it difficult to classify a source on the basis of one spectrum. However, sources such as Orion A and W51 show that the general appearance of the spectra persists at least ten years. The luminosity of a source at 22 GHz increases with its spectral complexity. Orion is classified as a triple consisting of the shell features at -5 km s^{-1} and $+15 \text{ km s}^{-1}$ and a third set of lines filling in the middle.

Genzel and Downes (1977b) found a pattern in the intensity variations which they called mode switching or mode drifting. In several sources, the intensity of two lines within 2 km s^{-1} of one another vary inversely over a period of a few months, while the total intensity remained more nearly constant. Although the frequency separation of two such lines is often similar to the hyperfine splitting, it is not exactly consistent. Furthermore, in Orion, the similar splitting of the H_2O and SiO maser lines implies a kinematic cause.

A.1.1.2 The high velocity features. High velocity masers have velocities more than 20 km s^{-1} from the ambient cloud velocity. The velocity difference in Orion is greater than 100 km s^{-1} , and, in some sources, the difference is greater than 250 km s^{-1} . The intensity of the high velocity features is 0.1 to 0.001 that of the low velocity features. About half the strong H_2O sources have known high velocity emission. It is probable that high velocity features could be detected in all strong sources with sufficient sensitivity. High velocity features are not associated with shell structure sources (Downes *et al.* 1979).

A.1.2 Association with Other Sources.

A.1.2.1. The water vapor masers. Burke et al. (1970) and Johnston et al. (1971) showed that the individual masers were extremely small (1 - 10 a.u.). Moran et al. (1973), using VLBI, determined the size and position of several features (Figures 15, 16, and 17). The individual maser features form small groups a few hundred astronomical units in size which I call "clusters". I developed this concept further in Section 3.3. Genzel and Downes (1977a) believe that the masers group into centers of activity 1000 a.u. in diameter. The centers of activity occur in groups 20 000 a.u. in size with an average projected separation between the centers of 3000 a.u. This distance is similar to the separation between compact IR sources. The high velocity features are scattered over an area 30 000 a.u. in diameter roughly centered on the low velocity features.

A.1.2.2 The hydroxyl masers. Mader et al. (1975, 1978), by frequency switching between OH and H₂O frequencies at one second intervals during a VLBI experiment, discovered that the 1665 MHz OH masers, the 1667 MHz OH masers, and the 22 GHz H₂O masers were all spatially separate in W3(OH), W49N, and W51.

A.1.2.3 Infrared sources. There are usually IR sources within 10 000 a.u. of the H₂O masers. However, only in Orion A and CRL2591 are the IR sources and the H₂O masers coincident. The IR luminosity is 10⁸ to 10⁹ greater than the total luminosity in the H₂O lines. Although increased sensitivity would probably reveal IR radiation associated with each H₂O group, the intensity of the IR radiation would

not correlate with the H_2O intensity. In Orion A, the line of IR sources is perpendicular to the line of H_2O masers, although, with increased sensitivity, that H_2O line is not as distinct as it was in the earlier observations.

IR sources may be divided into two classes (Genzel and Downes (1977a) from Wynn-Williams and Becklin 1974). The IR emission from hot dust in or around an HII region is not associated with H_2O masers. IR emission from cold dust which shows silicate absorption at $10\ \mu\text{m}$ is coincident ($<0.1\ \text{pc}$) with the H_2O masers and is probably a dust envelope about a star.

A.1.2.4 HII regions. Although the H_2O masers are within 200 000 a.u. (1 parsec) of an HII region, Genzel and Downes (1977b) found only 10% to 20% of the H_2O masers are coincident ($<0.1\ \text{pc}$) with compact HII regions. Therefore, the star creating the HII region is not supplying the energy for the maser. However, there may be super-compact HII regions too weak to be seen in the radio continuum near H_2O masers. Gilmore (1978), using the Green Bank interferometer, found no compact HII regions stronger than 10 mJy hidden in dark clouds near IR sources, CO emission, CO self-absorption, or Type I OH masers. Since all massive stars (massive stars are required to explain the IR luminosity and the high maser velocities) must form HII regions in the later stages of star formation, the masers and IR sources must correspond to an earlier stage of star formation. The correlation between compact HII regions and OH masers might be highest for massive stars, because massive stars form in less dense clouds suitable for

OH masers and because their compact HII regions become visible sooner. The H₂O masers found near HII regions show only a few low velocity features and some high velocity features.

A.2 Interpretation of the Observations

A.2.1 The Basic Model. Genzel *et al.* (1978) present two general models to explain the maser regions.

A.2.1.1 The maximum gain model. The H₂O is homogeneous and has some ordered motion (e.g., expansion or collapse with velocity a function of radius, uniform rotation, or Keplerian rotation). If the masers are unsaturated, the strongest emission will be from those paths over which the velocity gradient is smallest. The spectral pattern and position of the maser should make it possible to determine the motion of the gas. The high velocity features are gas blown out at the poles, or gas streaming through tunnels in the shell. If this model is correct, the type of ordered motion in the shell must vary considerably from source to source to account for the differences in maps and spectra.

A.2.1.2 The planetary model. The masers are dense globs of matter in a shell around the star. The high velocity features are those globs with the highest velocity. They are few and small. One would not expect much symmetry in the spectra. Furthermore, the clumps would not be gravitationally bound, and would disperse in 1000 years.

The actual situation is probably a combination of both models. The large scale motion of the gas determines the long term characteristics of the map and spectra, and condensations create the individual features.

A.2.2 The Low Velocity Features.

A.2.2.1 The gas motion. Genzel and Downes (1977b) classify the spectra of the low velocity features as singles, doubles or triples. The single line sources are the weakest and may be a separate population associated with lower mass stars (e.g., T Tauri stars).

The double and triple peak spectra may be attributed to expansion, contraction, or rotation of the gas. For expansion, the blue shifted peak comes from the gas which is flowing out from the star in our direction. The other peak is from the far side of the shell which is moving away. A central peak would be caused by gas at the projected edge of the shell whose velocity is perpendicular to the line of sight. In a thin shell, the gas at the edge would have the longest path length for amplification. A contracting gas cloud has a similar geometry with the redshifted lines from gas between us and the star which is falling onto the star. In rotation, the double spectral peaks come from the edge of the disk which is approaching us and the edge moving away from us. The central peak is from gas on the line of sight to the star. Its motion is entirely across the line of sight, and since the radial velocity is zero all along that line, the path length for maser amplification is the diameter of the disk.

If the velocity structure is due to gas in gravitational free-fall, the central mass must be large (at least $60 M_{\odot}$ for Orion). If the contraction is slower than free fall, and it usually is, then the mass must be even larger. If the velocity is due to rotation, the central mass required is twice as large as that needed for free-fall contraction. Since there are 100 or so H_2O maser regions like Orion in the galaxy, this requires a heretofore undetected population of massive stars. Hence, expansion is the most likely ordered motion.

Downes et al. (1979) propose a third model for the triple peak spectra sources. There is an inner hot gas ($T = 1000^{\circ}K$) where all the dust has evaporated and the expansion velocity is low. Maser emission from all over that region creates the spectral lines seen in the central part of the spectrum. In the cooler gas ($T = 100^{\circ}K$) further from the star, dust has formed and the radiation driven expansion is faster. The blue and red lines of the triple spectrum come from the approaching and receding sides of the shell. Some mechanism suppresses emission from the shell limb. My observations (i.e., the shell features are larger and vary less rapidly in intensity than the other masers) support the model in which the shell lines and the central lines are different types of masers. However, it is not clear why H_2O survives in the hot, low velocity gas while SiO cannot.

A.2.2.2 The driving force. The type of object driving the expanding gas must now be determined. It could be a low mass ($<3 M_{\odot}$) pre-main sequence star, an intermediate mass (3 to $10 M_{\odot}$) pre-main sequence star, a massive (10 to $30 M_{\odot}$) zero age main sequence star,

or an evolved star. A massive zero age main sequence star seems most likely for the following reasons (Genzel and Downes 1977a).

The temperature of the gas must be greater than 200°K to excite the H_2O . The density must be greater than 10^7 cm^{-3} to pump the H_2O , but less than 10^{11} cm^{-3} to avoid thermalizing the H_2O . The material must be flowing at 10 to 20 km s^{-1} . It seems impossible to satisfy these observations in the purely accretion phase of a protostar. Therefore, the energy source is probably a star. A low mass ($<3 M_\odot$) pre-main sequence star is unlikely because no H_2O masers as strong as, as complicated as, or with as wide a frequency separation as Orion have been associated with low mass stars, Herbig-Haro objects of T Tauri stars.

A 3 to $10 M_\odot$ pre-main sequence star might create the conditions suitable for the masers. After the formation of the hydrostatic core, a shock would exist as the infalling matter hits this boundary. Such a shock could just barely create conditions which could sustain the masers (Larson 1973).

A 10 to $30 M_\odot$ star would be a better source of energy. Such a star evolves so rapidly that it reaches the main sequence while the outer envelope is still contracting. The environment pictured by Cochran and Ostriker (1977) would be favorable for the creation of masers. Radiation pressure halts the collapse of the dust at 100 to 1000 a.u. A dust bound HII region forms and expands. It is preceded by a shock traveling at 25 km s^{-1} . When the shock reaches 1000 a.u. , the temperature is 200°K . The density is $10^5 - 10^6 \text{ cm}^{-3}$ ahead of the

shock, and $2 \cdot 10^8 \text{ cm}^{-3}$ between the shock and ionization front. The star cannot have a mass greater than $30 M_{\odot}$ because such a star would produce more luminosity than the $10^5 L_{\odot}$ which is observed in the infrared.

An evolved star undergoing mass loss (such as a Mira variable), might account for the masers. Although it is unlikely that an evolved star is responsible for the H_2O masers seen in most sites of star formation, there are good reasons to believe that one exists in the Kleinmann-Low nebula. This possibility is discussed in Section 3.3. SiO is seen only near evolved stars. Other molecules in Orion show double peaked spectrum as expected from a shell about an evolved star. However, the Orion spectra are not exactly like those seen in other evolved stars. The 22 km s^{-1} separation of the SiO peaks is the widest known. The OH peaks are also widely ($>20 \text{ km s}^{-1}$) spaced. No long-term variability in the IR like that seen in Mira variables has been seen. The SiO , H_2O and OH double peak lines all have the same velocity. In a star with mass outflow, the molecular specie with the highest excitation temperature would have the lowest velocity. None of these objections are so strong that one can rule out a Mira variable.

The six known supergiants with $\text{OH}/\text{H}_2\text{O}$ masers differ markedly from the Kleinmann-Low source. The supergiants do not have the symmetrical SiO spectrum and they have strong unpolarized 1612 MHz emission with peaks separated by the 50 km s^{-1} . Furthermore, none of the supergiants have high velocity features.

All the other characteristics of H_2O masers associated with HII regions are compatible with conditions found near young stars. Therefore, the ultimate source of energy for most of the radiation is probably a premain sequence star of three to ten solar masses, or a zero age ten to thirty solar masses main sequence star.

A.2.2.3 A detailed model for Orion Source "A". Genzel and Downes (1977a) observed a $3' \times 3'$ region around the KL nebula over a velocity range of $\pm 120 \text{ km s}^{-1}$ for water vapor masers. They obtained absolute positions to $\pm 2''$, and relative positions to $\pm 1''$. The spectra is shown in Figure 20 and a map from the tabulated data in Figure 19.

To analyze the results, they identify two centers of activity of H_2O masers in the southwest complex, source "A" and source "B". Source "A" they associate with IRC4. An artificial spectra of just the emission from that region reveals two pairs of lines, each centered on 5.5 km s^{-1} . The pair with features at 3.4 and 7.6 km s^{-1} has corresponding lines in the 1665 MHz transition of OH. The second pair at -5.5 and $+16 \text{ km s}^{-1}$ have counterparts in the SiO spectra and in the excited OH spectrum (Snyder and Buhl 1974, Thaddeus et al. 1974, Snyder et al. 1975, Rickard et al. 1975, Knowles et al. 1976). Genzel and Downes (1977a) assume that the OH features, the SiO emission, and the water vapor emission all originate in the same source, i.e., source A. My VLBI observations of 1978 November 2 show that the widely spaced water vapor features, and hence the SiO emission, are not associated with source A.

Genzel and Downes (1977a) developed a model for source "A". Although my observations show that it cannot be completely correct for source "A", it is well thought out and illustrates phenomena which could account for many of the H_2O maser observations. Source "A" contains a 10 to 30 M_{\odot} star. The star is surrounded by a compact HII region so small that it has escaped detection. The HII region is expanding at 11 km s^{-1} and is preceded by a shock. The H_2O , OH and SiO emission at -5 and $+16 \text{ km s}^{-1}$ comes from the compressed, heated matter between the shock front and the ionization front. The lines at 3.4 and 7.6 km s^{-1} arise in either (a) matter outside the shock front which is still accreting at 2 km s^{-1} , or (b) matter in the projected edge of the dust shell which has a small velocity gradient, and hence large maser gain, along the line of sight. In case b, slight rotation could split the major H_2O and SiO peaks by the 2.5 km s^{-1} observed.

Source "B" is $4''$ southwest of source "A". Its artificial spectra also shows a central peak at 18.4 km s^{-1} and peaks at $\pm 9.5 \text{ km s}^{-1}$. No definite IR source has been seen at this position and there are no SiO lines at the same velocities.

A.2.3 The High Velocity Features. The high velocity H_2O masers are best explained as dense clumps of gas in a high velocity gas outflow from a newly formed star. These features probably appear late in the star formation process when the high velocity stellar wind breaks through the dust shell. This high velocity flow is also seen in other molecules. Assuming a density of 10^8 cm^{-3} (Strel'nitskii 1974,

Burdjuzha, Ruzmaikina, and Barshalovich 1975) and the diameter of a low velocity feature of a few astronomical units (Moran et al. 1973) gives a mass of 10^{27} g. A stellar wind of 2000 km s^{-1} with a flow of $10^{-5} M_{\odot} \text{ yr}^{-1}$ could accelerate such a clump to 100 km s^{-1} in a distance of only 1000 a.u. The lifetime of the fragments would be a few hundred years. The IR radiation from the KL nebula would be too dilute to pump its high velocity masers. However, the wind itself could easily pump the masers. Alternatively, the kinetic energy dissipated when the cloud is finally decelerated by the surrounding medium could provide more than enough energy to power the masers.

A plot of velocity of the high velocity features as a function of the distance from the center of the KL nebula shows a linear relation. This is what one expects in a stellar wind with the velocity proportional to the radius. However, the scatter expected is larger than that actually observed. The expected scatter could be reduced if the wind elongated the globs in the radial direction. The fragments would then radiate preferentially in the radial direction. An elongation factor of five to one would fit the data reasonably well.

Genzel et al. (1979a), in a discussion of W51 Main, refine this model of the high velocity sources. A 100 km s^{-1} stellar wind from a newly formed $30 M_{\odot}$ star on the edge of a cloud creates a blister in the cloud. The high velocity features are dense globs at the interface between the wind and the surrounding cloud. The stellar wind accelerates the globs, confines them, and provides the energy to pump the masers. A stellar wind with $\dot{M} = 10^{-5} M_{\odot} \text{ yr}^{-1}$ could create a bubble $1.5 \cdot 10^{16}$ cm in diameter in 200 years.

The high velocity masers cannot be individual protostars since that would require a central mass of $10\,000 M_{\odot}$ to gravitationally bind them. Zuckerman and Palmer (1974) estimated the mass of the entire KL to be only 200 to $1000 M_{\odot}$. Scattering phenomena is an unlikely cause of the high velocity features because the high velocity features are not coincident with the low velocity features. The high velocity features are probably not associated with an ionization front from the optical nebula. In Orion A, the high velocity masers are centered on the KL nebula rather than the HII region. Furthermore, Genzel and Downes (1977a) found no H_2O masers along the ionization ridge south of the Trapezium (Becklin *et al.* 1976). Supernovae are unlikely causes (contrary to Kwan and Scoville (1976) as discussed in Section 1.2.6.2) for the following reasons: (1) There is no non-thermal radio source in Orion. (2) A supernova would emit enough radiation to destroy any molecules within 100 000 a.u. (3) The blast would sweep up material into a thin shell. In such a shell, the material with the greatest velocity would lie close to the line of sight to the center of the activity. The opposite is actually observed. (4) The number of sources with high velocity H_2O features implies a lot of supernovae.

A.2.4 Other Phenomena. Genzel and Downes (1977a) decided that the two strong masers in the northeast section of the Orion maser region did not fall into either the high or low velocity category. The apparent line of H_2O masers running from the northeast to the southwest disappears with increasing sensitivity.

Genzel et al. (1978) determined the statistical lifetime of H₂O masers to be 20 000 years, while the time to form a massive star is 10⁵ to 10⁶ years. Therefore, only 10% of the forming stars will show maser emission at any one time. For regions such as Orion-KL, all the stars must have started to form at the same time. This supports a trigger theory as suggested by Elmegreen and Lada (1977). (My alternate suggestion: there are ten times as many stars forming as we see centers of activity.)

The strong IR radiation which should come from the dust shell containing the H₂O masers has not been observed. Such a shell is expected to have a temperature of 300°K, an H₂ density of 10⁶ to 10⁹ cm⁻³, a diameter of 1000 a.u. and a thickness of 10 a.u. A shell of cooler dust surrounding the maser region might have a large enough optical depth to block the IR emission.

A.2.5 An HII Region Powered Model. One other very different maser model has been proposed. The H₂O masers are dense fragments of gas (<1 M_⊙) more than 10 000 a.u. from a compact HII region. They do not possess an internal energy source. Shocks from the HII region would collisionally pump the masers. The masers would be associated with a much later stage of star formation and should be more irregular in appearance. This model does not have the problem of missing infrared emission, but it does have some of its own. Forster et al. (1978) find only one compact HII region in each site of H₂O masers. The masers are always off to one side of the HII region, whereas one would expect to see the masers distributed around the HII region. The shock

front preceding the ionization front cannot supply enough energy to the masers to keep them radiating for years. Furthermore, even an O5 star ($10^5 L_{\odot}$) 10 000 a.u. from the masers could not supply enough radiation to heat the dust to 100°K , or to pump the maser directly.

A more detailed scenario for the evolution of a cloud of dust and gas about a young OB star is given in Table 2 of Genzel and Downes (1977b).



